

Microwave Forward Model for Land Surface Remote Sensing

**Dissertation zur Erlangung des Doktorgrades
der Naturwissenschaften (Dr. rer. nat.)**

**Fakultät Naturwissenschaften
Universität Hohenheim**

Institut für Physik und Meteorologie (IPM)

vorgelegt von
Chang-Hwan Park

aus Seoul, Korea
2015



Microwave Forward Model for Land Surface Remote Sensing

**Dissertation for Obtaining the Doctoral Degree
of Natural Sciences (Dr. rer. nat.)**

**Faculty of Natural Sciences
University of Hohenheim**

University of Hohenheim
University of Waterloo

submitted by
Chang-Hwan Park

from *Place of birth Seoul, South Korea*
2015

Dean:	Prof. Dr. Heinz Breer
1st reviewer:	Prof. Dr. Volker Wulfmeyer
2nd reviewer:	Prof. Dr. Ellsworth LeDrew
Submitted on:	18.06 2015
Oral examination on:	10.12 2015

This work was accepted by the Faculty of Natural Sciences at the University of Hohenheim on 10.12 2015 as "Dissertation for Obtaining the Doctoral Degree of Natural Sciences". (only necessary in the required copies after the successful oral examination)

Abstract

In order to improve hydro-meteorological model prediction using remote-sensing measurements, the difference between the model world and the observed world should be identified. The forward model proposed in this study allows us to simulate the BT (brightness temperature) from the land surface model to compare with the observed microwave BT. The proposed dielectric mixing model is the key part of the forward model to properly link the model parameters and the BT observed by remote sensing. In this study, it was established that the physically valid computation of the effective dielectric constant should be based on the arithmetic average with consideration of the proposed universal damping factor. This physically based dielectric mixing model is superior to the refractive mixing model or semi-empirical/calibration model with RMSE values of 0.96 and 0.63 for the predicted real and imaginary parts, respectively, compared to the measured values. The RMSE obtained with the new model is smaller than those obtained by other researchers using refractive mixing models for operational microwave remote sensing.

Once we determine the model uncertainty using this forward model, we can update the model state using the values obtained from the remote-sensing measurement. The challenging task in this process is to resolve the ill-posed inversion problem (estimation of multiple model parameters from a single BT measurement). This study proposes a simple partitioning factor based on model physics. Again, the forward model is crucial because these factors are required to be computed in BT space.

In the case study involving the Schäfertal catchment area, the proposed forward model, including the new dielectric mixing model, and the proper partitioning factors computed from land surface model physics was able to successfully extract the refined soil texture information from the microwave BT measurements. The highly resolved soil moisture variability based on the refined soil texture will allow us to predict convective precipitation with higher spatial and temporal accuracy in the numerical weather forecasting model. Moreover, microwave remote sensing using the developed forward model, which provides the soil texture, soil moisture, and soil temperature with a fine scale resolution, is expected to open up new possibilities to examine the energy balance closure problem with unprecedented realism.

Zusammenfassung

Zur Verbesserung der Vorhersagen von hydrometeorologischen Modellen unter Verwendung von Fernerkundungsmessungen muss der Unterschied zwischen der Modellwelt und den Messdaten identifiziert werden. Das in dieser Studie vorgeschlagene Vorwärtsmodell erlaubt es uns, Strahlungstemperaturen (BT) mit einem Landoberflächenmodell zu simulieren und mit gemessenen Mikrowellen-BT-Werten zu vergleichen. Ein neues dielektrisches Mischungsmodell wird vorgeschlagen, das den entscheidenden Teil des Vorwärtsmodells ausmacht, der die Modellparameter und die durch Fernerkundung gemessene BT richtig verbindet. In dieser Studie wurde festgestellt, dass die physikalisch fundierte Berechnung der effektiven Dielektrizitätskonstante auf dem arithmetischen Mittelwert unter Berücksichtigung eines ebenfalls neu vorgeschlagenen universalen Dämpfungsfaktors basieren sollte. Dieses auf den Regeln der Physik basierende dielektrische Mischungsmodell ist dem Brechungsindexmischungsmodell oder dem semi-empirischen Kalibrierungsmodell überlegen wie RMSE-Werte von 0,96 und 0,63 für den Vergleich der vorhergesagten realen bzw. imaginären Teile mit den gemessenen Werten zeigen. Der mit dem neuen Modell erhaltene RMSE ist kleiner als derjenige, den man mit den in der operationalen Mikrowellenfernerkundung verwendeten Brechungsindexmischungsmodellen erhält.

Nach der Quantifizierung der Modellunsicherheit mithilfe des neuen Vorwärtsmodells kann der Modellzustand mithilfe der mittels Fernerkundung gemessenen Werte verbessert werden. Die Herausforderung in diesem Prozess ist es, das schlecht gestellte Inversionsproblem zu lösen (Ableitung mehrerer Modellparameter aus

einer BT-Messung). Diese Studie schlägt einen einfachen Partitionierungsfaktor auf Basis der Modellphysik vor. Auch hier ist das Vorwärtsmodell entscheidend, da diese Faktoren im BT-Raum berechnet werden müssen.

In einer Fallstudie im Schäfertal-Einzugsgebiet konnte das vorgeschlagene Vorwärtsmodell, einschließlich des neuen dielektrischen Mischungsmodells und der richtigen Partitionierungsfaktoren berechnet aus der Landoberflächenmodellphysik, erfolgreich verfeinerte Bodentexturinformationen aus den Mikrowellen-BT-Messungen extrahieren. Die hochaufgelöste Bodenfeuchtevariabilität basierend auf der verfeinerten Bodentextur wird es erlauben, konvektiven Niederschlag in numerischen Wettervorhersagemodellen mit höherer räumlicher und zeitlicher Genauigkeit zu prognostizieren. Darüberhinaus wird erwartet, dass die Mikrowellenfernerkundung mit dem entwickelten Vorwärtsmodell, das Bodentextur, Bodenfeuchte und Bodentemperatur in hoher Auflösung liefert, neue Möglichkeiten eröffnet, das Problem der Energiebilanzschließung mit bisher nicht erreichter Detailtreue zu untersuchen.

Acknowledgments

First of all, I have to express that the topic and main ideas for this exciting PhD project are provided by my PhD advisor Prof. Volker Wulfmeyer. He always waits with a great patience until when I fully understand the vision of this project and the related key questions. I could keep tackling challenging problems with a great passion and enjoying developing many creative solutions in the serious level. I really appreciate his help to find my lifetime research topic.

Without support and scientific direction from Prof. Ellsworth LeDrew I could not have finished my PhD research. Specially, helping me to have many great opportunities in JPL and the IGARRS conference has propelled my PhD work in this research field. Despite the geographical long distance from Canada to Germany, his support was significant during my PhD.

Sincerely I am thankful for the substantial help from Dr. Andreas Behrendt. Attending his class in University of Hohenheim, I had many opportunities to learn about the traditional spectroscopic techniques and discuss more about the new aspect of the dielectric constant which is the key solution in my thesis. His constructive comments and enormous efforts helped me to develop many ideas and ultimately shaped me to be a good scientist during my PhD.

For three months of my research stay in JPL, working with Dr. Tom Jackson inspired me as respectful great scientist. Also his every day lessons for me about past and future soil moisture microwave remote sensing will be a meaningful foundation for my remote sensing research.

I have had a great pleasure to learn R (a programming language for Statistical Computing) from Dr. Martin Ivanov in the professional level. His teaching and explanation for me to master R was critical to the experiment and to demonstrate my ideas for the data.

From the beginning of my PhD Dr. Matthias Grzeschik provided me with enormous help in learning about NOAH-MP land surface model and data assimilation system. Even though he

moved out from the junior supervisor position, his efforts in my PhD work are still definitely substantial.

Within IRTG (International Research Training Group in University of Tübingen), I have had the great pressure to work with my colleagues, Atefeh Hosseini, Alicia Sanz-Prat, Zhongwen Bao, Karim Norouzi-moghanjoghi, Bijendra Bajracharya, Diane Von-gunten and Jürnjakob Dugge. I also would like to thank Anneli Schöniger to help to prepare German abstract in this thesis and discussions and explanations associated with my general questions in hydrology during the PhD study. I am grateful to Ms. Monika Jekelius. Owing to her valuable advices and numerous assistances within IRTG program my studying and living in Tübingen definitely becomes much easier.

Finally, I would like to thank Prof. Olaf Cirpka. His truthful advice and mentoring are always firstly related with “students” in the IRTG program. I am very fortunate to do my PhD in the excellent research environment. Also his critical but ultimately very helpful scientific insights and suggestions in my PhD research were considerable even though his expertise is different from my PhD topic.

Overall, I was very lucky and happy PhD student in University of Tübingen and Hohenheim. Furthermore, I appreciate my parents support for my dream from Korea. I appreciate also my wife and son to awaken me to live real life.

This PhD work is financially supported by German Research Foundation (DFG) International Research Training Group (IRTG) “GRK 1829” is gratefully acknowledged.

CONTENTS

Abstract	3
Acknowledgments.....	5
1. Introduction.....	11
1.1 Soil temperature and soil moisture regulation	11
1.2 Soil texture as a key factor in land surface model and microwave observation operator.....	13
2. Dielectric mixing model	18
2.1 Measurements from microwave remote-sensing	18
2.2 Theoretical issue in interpretation of dielectric measurements.....	21
2.3 Investigation of dielectric and refractive mixing theories	25
2.4 Multi-phase mixing model for dielectric constant	29
2.5 Multiphase-phase mixing model for conductivity	35
2.5.1 Soil	35
2.5.2 Salinity	36
2.5.3 Water	37
2.6 Complex dielectric constant.....	39
2.7 Comparison with other approaches.....	40
2.8 Bulk dielectric mixing with damping	44
2.9 Results.....	48
2.10 Discussion	63
3. Radiative transfer model	65

3.1	Brightness Temperature Scaled on Spaceborne Measuring System.....	65
3.2	Colum-Integrated Brightness Temperature.....	65
3.3	Reflectivity of Soil, r_s , from Isotropic Dielectric Constant	68
3.4	Transmissivity of Canopy, t_c , from the Canopy Water Related Optical Thickness	69
3.5	Anisotropic Brightness Temperature Measured on Microwave Sensor	70
4.	Land surface model.....	71
4.1	Well-Posed Response Model	73
4.2	Physical Partitioning from Perturbation.....	74
4.2.1	Process 1: Model variation & Forward response model	75
4.2.2	Process 2: Partitioning factor	76
4.2.3	Process 3: Innovation	78
4.2.4	Process 4: Partitioned innovation, Inversed response & Model improvement	78
	These are the model improvements from the measured BT.	79
4.2.5	Process 5: Error consideration	80
4.2.6	Process 6: Improved model states	80
5.	Results.....	81
5.1	Limited knowledge about soil texture information.....	81
5.2	Homogeneous atmospheric weather forcing.....	82
5.3	High resolution innovation from observation	85
5.4	Computation of partitioning factor from model.....	87
5.5	Improvement for multiple model variables.....	87
5.6	Validation of BT simulation	94
5.7	Improvement in heat and water fluxes of NOAH-MP	97
6.	Summary and overview	100

1. Introduction

The simultaneous extraction of realistic soil temperature and soil moisture readings from remote-sensing measurements is challenging. The key factor in the variability of these soil properties is the soil texture. This study introduces a novel forward model for extracting the highly resolved soil texture information from microwave remote-sensing measurements.

1.1 Soil Temperature and Soil Moisture Regulation

Soil temperature and soil moisture are critical variables in numerical weather and climate prediction models. These model variables control the water and energy balance at the land surface [1]. An accurate knowledge of water and energy fluxes is closely related to the weather prediction of a precipitation event a week or a month later [2]. Furthermore, a highly resolved soil moisture input is critical for the proper initiation of convective precipitation as demonstrated in the COPS (Convective and Orographically induced Precipitation Study) campaign [3-7]. There is a complex relationship between the status of soil temperature and soil moisture, on the one hand, and soil texture and vegetation type, on the other, as shown in Fig. 1.

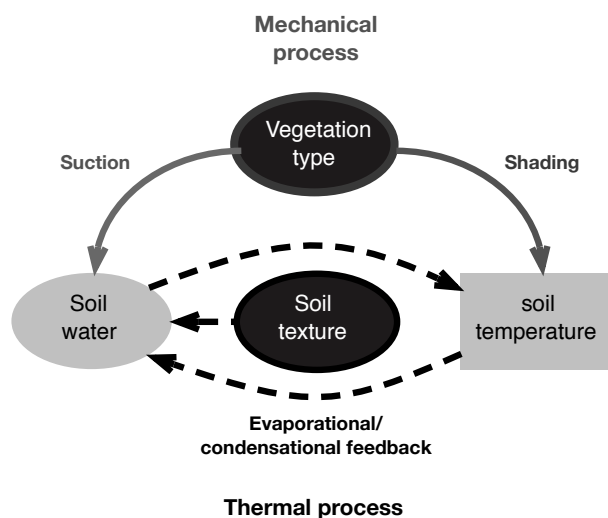


Fig. 1. Soil water and soil temperature regulation by soil texture and vegetation types; the arrow direction indicates the effect-results relation, and color codes are explained in the text.

Firstly, the soil texture helps to define the water availability on the land surface. The volume of water participates in evaporation and condensation processes according to the temperature variation of the surface layer, amongst other variables; for example, when the surface temperature increases, the soil water decreases by evaporation. A little later on, the surface temperature decreases as a result of negative feedback from the loss of latent heat due to the transition of the surface soil moisture (surface temperature increase–surface water decrease–surface temperature decrease). Fig. 1 shows that the soil texture (dotted curves) has a direct effect on the determination of water availability within the surface soil layer. On the other hand, the change in the soil temperature as a result of the soil texture is an indirect effect. The soil texture can also be related to the variation in soil temperature via the thermal conductivity specified for the soil texture. However, compared to the indirect effect of the evaporation/condensation by water on the temperature, the direct effect of the soil texture on the soil temperature in terms of soil thermal conductivity is negligible.

When vegetation is involved in this process (grey solid curves in Fig. 1), the type of vegetation also determines the rate of soil water loss. The change in the soil temperature because of shading by leaves modulates the evaporation and condensation processes towards less thermal activity. Because the plants lower the amount of water and the temperature, evaporation above the soil might be limited.

The successful estimation of the vegetation properties by eliminating both the contribution of the soil and soil water contributions or for the accurate soil moisture and soil temperature estimation from the vegetation disturbance firstly requires the identification of the soil texture effect on heat or water fluxes and quantification of the error in the model prediction. The contribution of soil texture in the regulation of the energy balance is still largely unknown. Therefore, bare soil remote sensing using microwave channel is necessary.

1.2 Soil Texture as a Key Factor in Land Surface Model and Microwave Observation Operator

The role of soil texture in the exchange of heat and water is largely unknown. Fig. 2 shows that the soil texture contains key information related with land surface model parameters and the surface energy balance. The highly resolved hydraulic and thermal conductivities in the land surface model (Fig. 2.(a)) can be obtained from the accurate matrix potential computed with refined soil texture information from remote-sensing measurements (Fig. 2(b)). It means that the model prediction for soil temperature and soil water can be improved by the temporal integration of the improved heat and water transport equations in which the thermal and hydraulic conductivities are key parameters, as shown in Fig. 2.

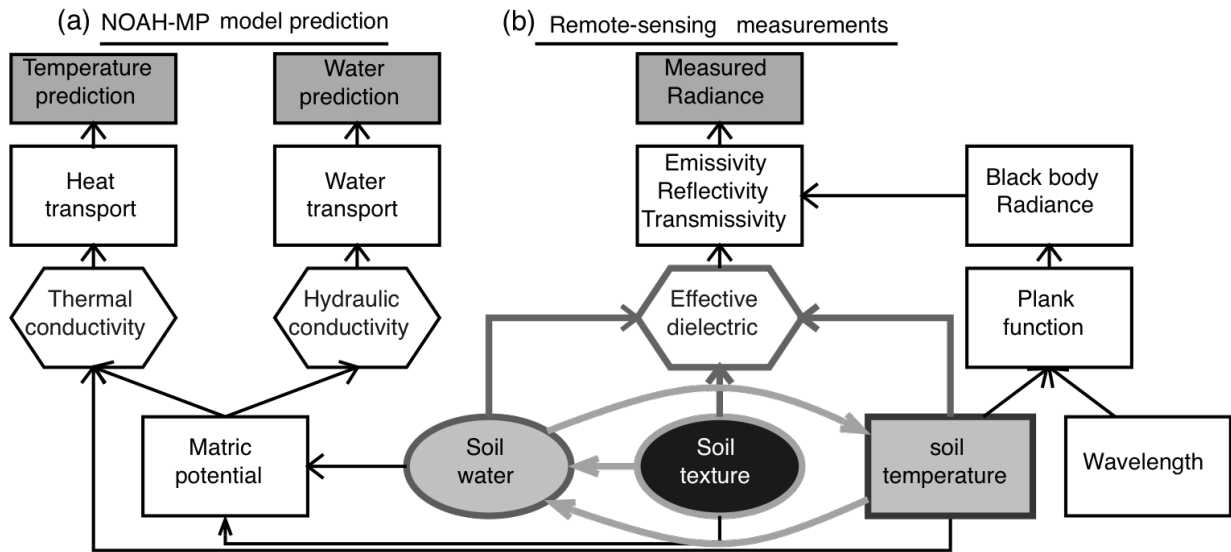


Fig. 2. Effect of soil texture on energy flux over bare soil simulated in the land surface model and its observing process by the advanced forward model for microwave remote sensing.

However, obtaining detailed global soil texture information, or even performing local scale soil texture mapping *in situ*, is a very challenging task. Thus, it was expected that the microwave remote-sensing measurement might be able to provide us not only with the soil

temperature and moisture, but also spatially highly resolved soil texture information. To link these properties with microwave radiance or BT measurements, I first studied the relationship between the effective dielectric constant and soil water, soil temperature, and soil texture (grey lines in Fig. 2), which is the main contribution of this thesis.

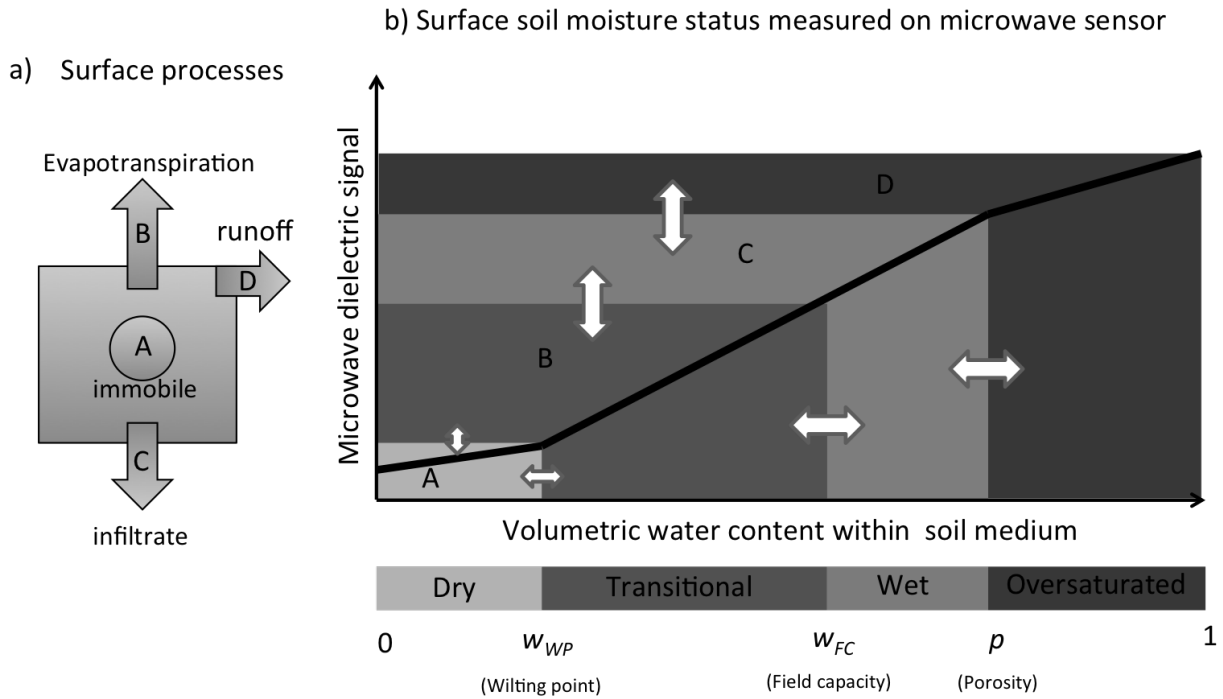


Fig. 3. Water content processes: (a) surface water fluxes and (b) their possible measuring regimes by microwave remote-sensing (the white arrows denote shifting regimes by soil texture)

As shown in Fig. 3(b), the soil moisture in each stage (i.e., dry, transitional, wet, and oversaturated), which is measurable by microwave remote-sensing techniques, tends to move in different directions in the surface soil layer (A: in the dry stage, the soil water is immobile, B: in the transitional stage, the soil water is removable from the soil medium by evapotranspiration, C: in the wet stage, gravity enables the water to infiltrate the soil, and D: in the oversaturated

stage, the soil water tends to flow over the surface. The effects of the soil moisture volume on climate and human-related events are presented in Table 1.

Table 1. Soil water status classified by soil texture information and its effect on energy balance and impact on life

	<i>Water status</i>	<i>Water flux</i>	<i>Socioeconomic effect</i>
A	Dry	Immobile within soil	Drought
B	Transitional	To atmosphere	Crop yield growth
C	Wet	To subsurface	Ground water recharge
D	Oversaturated	Over surface	Landslides/flood

Green box: positive effect and red box: negative effect on human life

As shown in Table 1, the different soil moisture stages lead to different kinds of interaction among the different earth surface layers to achieve a water and energy balance. Furthermore, knowledge of the soil water status from remote-sensing measurements is important for monitoring and managing water and food resources and the prediction of water-related natural hazards, such as landslides, caused by swelling clay.

In this research, I assess the capability of microwave remote sensing to measure soil texture accurately. In addition, I show that the use of improved soil texture information in land surface models enhances the accuracy of the results of the simulation of water and heat fluxes. The models that were developed in this study were demonstrated by assessing the soil texture of the Schäferfetal sub-catchment area in Germany, as shown in Fig. 4.

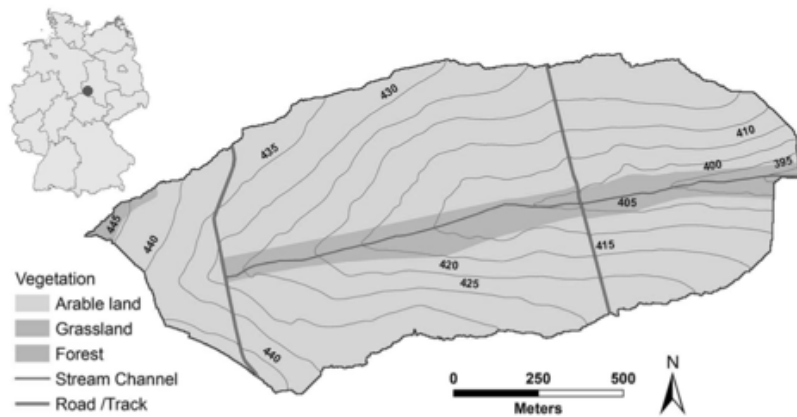


Fig. 4. The location and size of the Schäfertal catchment area with the initial land use data [8].

The size of this sub-catchment area is sufficiently small (1.4 km^2 [9]) to assume that an atmospheric forcing and precipitation event would be homogenous over the entire catchment area. This condition facilitates detection of the soil texture effect in remote-sensing measurements.

In this thesis, I introduce a novel forward model to quantify the effect of the soil texture and its error propagation on the heat and water fluxes on bare soil. The advanced forward model is composed of a reliable land surface model as well as a new model for dielectric mixing and a known radiative transfer model. The NOAH-MP (Noah Land Surface Model with Multi-Parametrization options) land surface model [10] is useful for resolving the inversion problem to estimate multiple soil properties such as soil water and temperature, because the model can provide a reliable physical relationship among these variables to express their unknown status in terms of the known sensitivity information. This is explained further in Section IV, Land Surface Model. The physically based dielectric mixing model accurately links the dielectric constant and soil properties. Finally, the radiative transfer model enables us to simulate the microwave brightness temperatures and assimilate them into the land surface model. The soil texture information in this framework is critically related to the thermal and hydraulic

conductivities in the NOAH-MP land surface model, the wilting point, and porosity in the novel dielectric-mixing model. The hypothesis in this new methodology is that accurate soil texture information from microwave measurements would be able to improve the realism of the water and heat fluxes in the land surface model and, therefore, also the soil temperature and water predictions.

To demonstrate the soil texture effect I performed a case study over the Schäfertal sub-catchment area, which is one of the TERENO (Terrestrial Environmental Observatories) [11] sites in Germany, by using a PLMR (Polarimetric L-band Multibeam Radiometer) developed by ProSensing (ProSensing Inc., USA). The viewing angle and the waveband of the PLMR used in this study was 38.5° among the six beams and 1.414 GHz respectively. Measurements were recorded by placing the PLMR aboard an aircraft, which measured the BT by flying low and slowly over the two distinct soil textures (clay loam and loam) in the relatively bare surface states of the Shäfertal region [12]. The small size of this catchment area allowed us to reasonably assume that atmospheric forcing, including precipitation events, are spatially homogenous. These controlled surface conditions allowed us to focus on the time invariant effect of the soil texture on the heat and water fluxes.

Finally, the advanced forward model with the proposed partitioning factor was used to assimilate the L-band microwave remote-sensing measurements into the NOAH-MP model by scaling the energy balance realistically. Furthermore, I validated the actual improvement by comparing the results with the microwave remote-sensing measurements.

2. Dielectric Mixing Model

2.1 Measurements from Microwave Remote Sensing

For remote-sensing signal processing purposes, the Earth can be divided into several separate layers between the sensor and the target, such as the atmosphere, canopy, and soil – each of these again with sub-layers. However, it can be very complicated and error-prone to distinguish the contribution of each layer-not even to mention a sub-layer-in an integrated-path measurement of, for example, the BT. In contrast to radiation in the visible and IR spectral region, microwaves penetrate non-precipitating clouds and the gaseous atmosphere without significant interaction. Therefore, microwaves can provide more reliable information than IR signals about the soil properties and temperatures of the terrestrial surface as well as of vegetation. At the same time, using microwave remote-sensing data enables us to reduce the uncertainties of remote-sensing observations made at other wavelengths regarding the land surface for improved estimations of atmospheric trace gases, aerosols, and clouds. Therefore, an understanding of the interaction of microwaves is critical, not only for land surface remote sensing, but also for observations of the Earth system as a whole.

In the current work, I focused on the emission of microwaves from bare soil, which was validated with TDR (Time-Domain Reflectometer) probe measurements. Future studies may extend the new dielectric-mixing model presented here for the first time to ground vegetation and canopy layers.

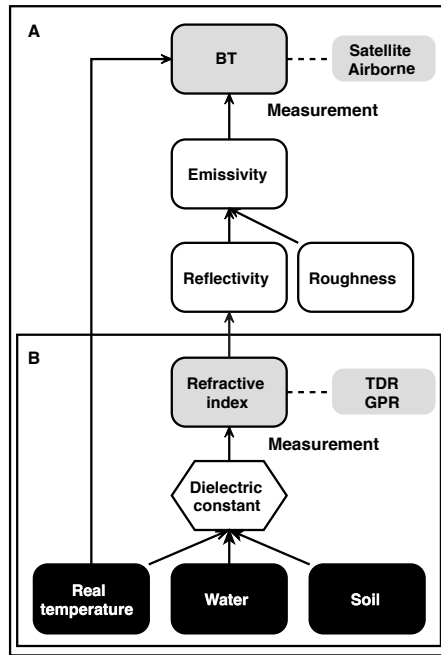


Fig. 5. Measuring principles of bare soil properties (black boxes) by satellite and airborne remote sensing in the microwave region (box A) and TDR and GPR (box B). The dielectric constant (hexagon) is the link between the measured parameters of the sensors (BT and refractive index, respectively) and the targeted soil properties.

When a material is exposed to an electric field, its dielectric constant describes the interaction. Thus, the remote sensing of land-surface properties, such as soil moisture, requires an effective operator for the computation of the effective dielectric constant (Fig. 4). TDR and GPR (Ground Penetrating Radar) measure the refractive index, compute the effective dielectric constant, and quantify soil water contents with separately obtained temperature and soil texture information. On the other hand, airborne and space-borne remote-sensing instruments measure the BT (box A in Fig. 5). To retrieve the soil moisture content from the measured BT, the traditional retrieval method requires ancillary information to account for soil temperature and soil texture as well as for the effects of vegetation. Studies have attempted to obtain this ancillary data for vegetation from the vegetation parameter b [13], multi-frequency microwave sensor

measurements [14-16], the NDVI (normalized differenced vegetation index) [17], or the MPDI (microwave polarization difference index) [18-20]. Although it is especially challenging for areas covered with vegetation, the measurement of land-surface properties is already very uncertain for bare soil; hence, for this simpler situation, the ancillary information about soil temperature and soil texture are quite critical for retrieving the soil moisture content. In a later step, I will integrate the dielectric mixing model into a land surface model. Our new integrated model provides the physical relationship for the calculation of the dielectric constant depending on soil temperature, soil texture, and soil moisture. All the information that is necessary to calculate the BT is available in the land surface model. Thus, the new mixing model can be used as a forward operator for determining BT. Finally, the BT obtained via microwave measurements may then be used in a data assimilation scheme.

In modern space-borne microwave remote sensing several bands are used: L-band (1 to 2 GHz), C-band (4 to 8 GHz), and K-band (12 to 40 GHz). Examples of remote-sensing instruments and satellites are listed in Table 2 [21].

Table 2. definitions of remote sensing system acronyms and applied wave bands [21].

Space borne microwave sensors		Wavebands		
Acronyms	Description	L	C	K
AMSRE-E	Advanced Microwave Scanning Radiometer onboard the Earth Observing System		*	*
ASCAT	MetOp's Advanced SCATterometer, the successor to the C-band scatterometers ESA's ERS-1 and ERS-2 satellites		*	
ALOS PALSAR	Advanced Land Observing Satellite	*		
AQUARIUS/SAC-D	NASA's sea surface salinity mission	*		
ASAR	Advanced Synthetic Aperture Radar onboard ENVISAT		*	
ERS-SAR	European Remote Sensing Satellite		*	
JERS-1 SAR	Japanese Earth Resources Satellite 1Landsat TM: Landsat Thematic Mapper	*		
RADARSAT 1&2	Canadian Space Agency's Radar Satellite		*	
SIR-A/C/X	Space borne Imaging Radar-L/C/X Band Synthetic:		*	
SMAP	NASA's Soil Moisture Active Passive Mission	*		
SMOS	ESA's Soil Moisture and Ocean Salinity Mission	*		
SSM/I	Special Sensor Microwave ImagerQuickscat: NASA's Quick Scatterometer			*
WindSAT	Multichannel multi-frequency microwave radiometer for Ocean Surface Wind detection		*	*
Tandem-L	Proposed L-band Radar Mission	*		

2.2 Theoretical Issue in Interpretation of Dielectric Measurements

The effective dielectric constant of the soil is a key variable to quantify the land surface properties. However, the models used to date to calculate the effective dielectric constant violate the first principle in physics; for example, when using mixing models for the refractive index and not—as should be the case—for the dielectric constant itself or when using semi-empirical power-law models or calibration models, which require various experimental fitting parameters. Nevertheless, these empirical and semi-empirical models are widely utilized in remote-sensing applications – including the interpretation of active remote-sensing measurements with TDR and GPR, as well as of passive microwave remote-sensing measurements, such as those recorded with the SMOS (Soil Moisture and Ocean Salinity) and SMAP (Soil Moisture Active Passive) satellites. In this thesis, I propose a new physical approach, based on an arithmetic average with damping, for obtaining the effective dielectric constant of multiphase soil. This approach enabled us to obtain results that show better agreement with experimental data than previous approaches. Therefore, using our model as a forward operator should produce improved results in a data assimilation system.

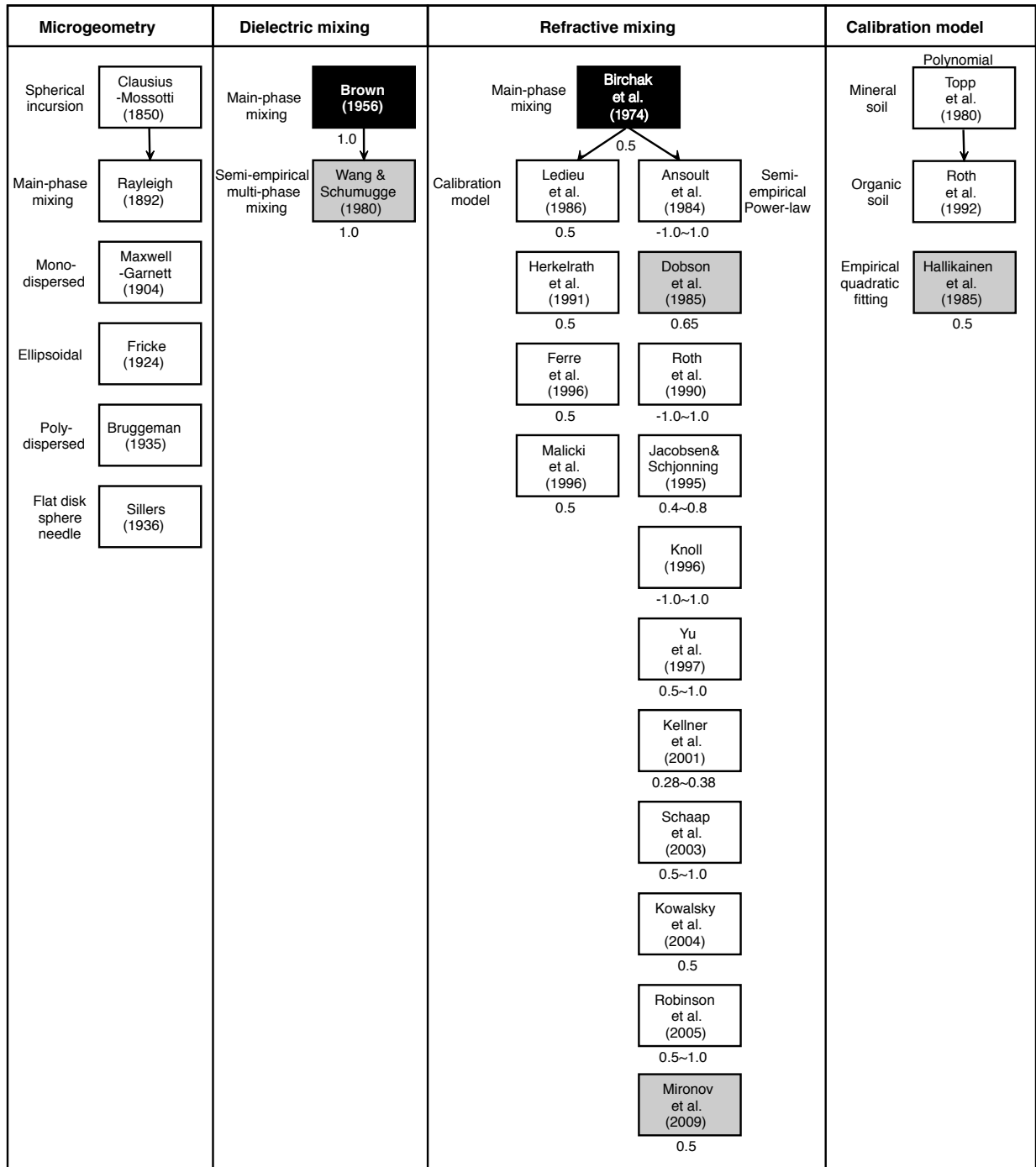


Fig. 6. Various methods for computing the effective dielectric constant; the numbers under each box indicate the value used for the exponent α in equation (4); micro geometry models [22-30], dielectric mixing models [31, 32], refractive mixing models [33-49], and calibration models [50-52]; black boxes are two main mixing theories for computation of effective dielectric constant; the gray boxes are the most popular but semi-empirical approaches and are

operationally used in airborne/space-borne microwave remote sensing, which I compare with our physically-based model in this publication.

The accurate computation of the effective dielectric constant is essential for all these passive and active microwave sensors. Furthermore, it is also critical for the analysis of materials in materials sciences [53]. The first dielectric mixing formulas were proposed for cavities, which are (hypothetical) spheres [22, 23], monodispersed spheres [24], polydispersed spheres [26], non-spherical [28], as well as for non-spherical nanoporous media and nanoparticles [25, 27]. However, these mixing models contain an innate limitation for complex multiphase materials such as moist soil: the practical design of the dielectric mixing model based on a microgeometry approach relies on empirical adjustments [53].

For land surface remote sensing, two mixing theories have been proposed, namely the ‘dielectric average’ originally proposed by Brown [31]

$$\varepsilon_{eff} = \sum_{j=1}^m v_j \varepsilon_j, \quad (1)$$

and the ‘refractive average’ originally proposed by Birchak [33]

$$n_{eff} = \sum_{j=1}^m v_j n_j = \sum_{j=1}^m v_j \sqrt{\varepsilon_j}. \quad (2)$$

Both approaches relate the effective dielectric constant ε_{eff} of a material to the dielectric constants ε_j of its m different components weighted according to their volumetric fractions v_j in the mixture. The refractive index n_{eff} measured by TDR and GPR is related to the time duration of electromagnetic wave propagation in a medium, in our case in the soil-water mixture [54], according to

$$n_{eff} = \frac{ct}{2L} \quad (3)$$

where c is the speed of light, t is the traveling time along the probe rod and L is the length of the probe rod.

A further refinement used by [35] and [36] is the empirical modification of (1) with an exponent α referred to as the ‘shape factor’ according to

$$\varepsilon_{eff}^{\alpha} = \sum_{j=1}^m V_j \varepsilon_j^{\alpha}. \quad (4)$$

The linear relationship of the soil moisture with the refractive index, similar to (2), has been widely used in calibration models [34, 37, 39, 41]. This approach has further evolved into various power-law based models: because the soil moisture estimation following (2) could not meet the required accuracy for different soil textures and frequencies of electromagnetic waves, various values have been proposed for α [35, 36, 38, 40, 42-47]. A description of the nonlinear relationship between water content and the dielectric constant with empirical calibration models has also been proposed [50-52]. An overview of these models together with the different values used for α is provided in Fig. 6. However, the theory of the refractive mixing is physically invalid and violates the superposition rule of polarizability, which is a smaller scale component of the dielectric constant. This section demonstrates that the volume of material is linearly proportional to its dielectric constant, and not to its refractive index. I demonstrate that the effective refractive index n_{eff} is supposed to be calculated from the effective dielectric constant ε_{eff} based on the arithmetic mean (parallel mixing) according to (1), and not (2) or (4).

2.3 Investigation of Dielectric and Refractive Mixing Theories

The dielectric constant and refractive index are macroscopic averages of polarizabilities within an atom. Firstly, I consider the smaller scale average, polarizability. The total polarizability for a single molecule $\alpha_{molecule}$ is composed of orientational polarizability α_{orient} , ionic polarizability α_{ionic} , and electronic polarizability α_{elect} [55] via

$$\alpha_{molecule} = \alpha_{orient} + \alpha_{ionic} + \alpha_{elect} . \quad (5)$$

I can extend the total polarizability of a single molecule to the total polarizability for multiple molecules by the equivalent principle of superposition according to

$$\sum_{i=1}^m \alpha_{orient,i} + \sum_{i=1}^m \alpha_{ionic,i} + \sum_{i=1}^m \alpha_{elect,i} = \sum_{i=1}^m \alpha_{molecule,i} \quad (6)$$

Subsequently, I can express the total amount of homogenous molecular polarizability for the specific species j (e.g., soil, air, or water) by

$$\sum_{i=1}^m \alpha_{i,j} = m \alpha_j \quad (7)$$

where m_j is the number of molecules of species j , i is the order of molecule, and j is the order of species.

Any 2D (two-dimensional) local electric field E can be expressed with a measurable mean, which is a macroscopic electric field \bar{E} , and its sub-grid scale perturbation, which is a microscopic electric field E' within a single molecular species j , by

$$E_{Local,j,j} = \bar{E}_j + E'_{i,j} \quad (8)$$

To consider the parallel mixture I define the total polarizability of molecules measured over the unit surface to be the surface polarization density P^{2D} , which is composed of the individual molecular polarizability $\alpha_{i,j}$ and its local electric field $E_{local,i,j}$ on the surface boundary

$$P_j^{2D} = \sum_{i=1}^m \frac{1}{A_j} \varepsilon_0 \alpha_{i,j} E_{Local,i,j} \quad (9)$$

where A_j is the area for species j .

Applying (7) and (8), using (9) enables us to express the homogenous molecular surface polarization density as

$$P_j^{2D} = \frac{m}{A_j} \varepsilon_0 \alpha_j \bar{E}_j^{2D} + \frac{1}{A_j} \varepsilon_0 \alpha_j \sum_{i=1}^m E'_{i,j} \quad (10)$$

I consider the sub-grid scale property as random noise. Then its total contribution can be assumed to be zero.

$$\sum_{i=1}^n E'_{i,j} \approx 0 \quad (11)$$

Then, we can simplify (10) with 2D number density M_j^{2D} for a certain species j ,

$$P_j^{2D} = M_j^{2D} \varepsilon_0 \alpha_j \bar{E}_j \quad (12)$$

$$\text{with } M_j^{2D} = \frac{m_j}{A_j} . \quad (13)$$

On the other hand, in the macroscopic electric field, which appears in the Maxwell equations, the polarization density can also be expressed in terms of the dielectric susceptibility χ_j^{2D} as follows.

$$P_j^{2D} = \varepsilon_0 \chi_j^{2D} \bar{E}_j \quad (14)$$

Thus, (12) and (14) can be used to relate the single molecular scale property α_j to the 2D macroscopic susceptibility χ_j^{2D} by

$$M_j^{2D} \alpha_j = \chi_j^{2D} \quad (15)$$

Then we can express the mean polarizability α_j for species j , with 2D macroscopic susceptibility χ_j^{2D} .

$$\alpha_j = \frac{1}{M_j^{2D}} \chi_j^{2D} \quad (16)$$

Now, we consider multiple species in the surface polarization density.

$$P_{eff}^{2D} = \sum_{j=1}^n P_j^{2D} = \frac{1}{A_{total}} \sum_{j=1}^n m_j \epsilon_0 \alpha_j \bar{E}_j \quad (17)$$

where n is the number of species

By introducing a partial volume A_j , the polarization density for the mixture of different species can be expressed as,

$$P_{eff}^{2D} = \sum_{j=1}^n \frac{A_j}{A_{total}} \frac{1}{A_j} m_j \epsilon_0 \alpha_j \bar{E}_j \quad (18)$$

where A_{total} is the total area from all species.

In (18) the 2D volumetric fraction is included in the polarization density. I define this volumetric fraction part with the mixing ratio, v .

$$P_{eff}^{2D} = \sum_{j=1}^n v_j^{2D} M_j^{2D} \epsilon_0 \alpha_j \bar{E}_j \quad (19)$$

$$\text{where } v_j^{2D} = \frac{A_j}{A_{total}} \quad (20)$$

Using (15), we can express the 2D polarization density of the heterogeneous mixtures with the dielectric susceptibility.

$$P_{\text{eff}}^{2D} = \varepsilon_0 \left(\sum_{j=1}^n v_j^{2D} \chi_j^{2D} \right) \bar{E} \quad (20)$$

If the effective property is defined with the 2D mixing fraction ratio v_j^{2D} , we can express the effective electric susceptibility in the polarization density for heterogeneous medium as,

$$P_{\text{eff}}^{2D} = \varepsilon_0 \chi_{\text{eff}}^{2D} \bar{E} \quad (21)$$

where

$$\chi_{\text{eff}}^{2D} = \sum_{j=1}^n v_j^{2D} \chi_j^{2D} . \quad (22)$$

The electric susceptibility is reflected to the dielectric constant

$$\chi_{\text{eff}}^{2D} = \varepsilon_{\text{eff}}^{2D} - 1 . \quad (23)$$

The derivation explained above allows us to determine which of the mixing theories presented in (1) and (2) are suitable for the calculation of the effective dielectric constant. In terms of the single molecular polarizability, the superposition principle is valid in (5). For a homogenous medium, α_j is proportional to χ_j (15). Then, we can superimpose χ_j with the mixing ratio v_j (22) to calculate χ_{eff} . The χ_{eff} is proportional to ε_{eff} (23). In this manner, it was determined that the dielectric mixing approach (1) is the physically valid average method. On the other hand, the refractive mixing approach represented by (2) or the power-law-based refractive mixing approach violate the superposition rule when the calculation has been examined down to the polarizability scale.

2.4 Multi-phase Mixing Model for Dielectric Constant

Because the dielectric constant follows the superposition rule of polarizability, this constant, and not the refractive index, is linearly proportional to the volume of the physical material. Therefore, the arithmetic average of the dielectric constant by volumes of soil water, of soil particles, and of air according to (1) is the physically valid approach.

For land surface properties, the main phases to be considered in the dielectric averaging approach [32] are soil, water, and air. Thus, m becomes 3 in (1). Furthermore, the volumetric fractions v_j are described by the soil porosity ρ resulting in

$$\epsilon_{eff} = (1-\rho)\epsilon_{soil} + w\epsilon_{water} + (\rho-w)\epsilon_{air} \quad (24)$$

with w for the volumetric fraction of water, $1-\rho$ for the volumetric fraction of soil, and $\rho-w$ for the volumetric fraction of air. The volumetric fractions of course add up to unity:

$$(1-\rho) + w + (\rho-w) = 1. \quad (25)$$

The soil volumetric ratios v_{silt} , v_{clay} , and v_{sand} enable us to derive a sub-phase model for the dry soil part namely

$$\epsilon_{soil} = v_{silt}\epsilon_{silt} + v_{clay}\epsilon_{clay} + v_{sand}\epsilon_{sand} \quad (26)$$

with

$$v_{silt} + v_{clay} + v_{sand} = 1. \quad (27)$$

The soil water can be subdivided into bound and free water, both of which show very different values for the dielectric constant [56-58]. Then, the effective soil water dielectric constant ϵ_{water} , can be expressed with the sub-phase volumetric mixing ratio, v_{bound} and v_{free} , with the

different dielectric properties of thin water layers around soil particles (so-called ‘bound water’) and larger water volumes (so-called ‘free water’) that are ϵ_{bound} and ϵ_{free} , respectively.

Table 3. Optical and volumetric properties of multi-phase model within the rescaling process

Effective medium	Main-phase	Sub-phase	
Optical property	ϵ_{water} (unknown)	ϵ_{bound} (modeled)	ϵ_{free} (known)
Volumetric property	W (measurable)	V_{bound} (not measurable)	V_{free} (not measurable)
$W < W_{wp}$	$0 \sim W_{wp}$	0~1	0
$W_{wp} < W < \rho$	$W_{wp} \sim \rho$	1~0	0~1

Ultimately, the model requires the unknown effective value ϵ_{water} . As shown in Table 3, we can obtain this parameter with the modeled value of ϵ_{bound} (see (88) and (89)) and the known value of ϵ_{free} via their fractional ratio V_{bound} and V_{free} . Because the values of V_{bound} and V_{free} are not measurable, I approximate them in terms of the soil water fraction W , which can be measured, via a rescaling process. The sub-phase fractional ratio V_{bound}/V_{free} is an expression depending on W as well as on the wilting point W_{wp} and porosity ρ .

Firstly, when the dry soil particles become moist and W remains below the wilting point, the volumetric soil water content consists only of bound water such that:

$$\epsilon_{water} = \epsilon_{bound} \quad (28)$$

Thus, I obtain the unknown value ϵ_{water} when W varies between 0 and W_{wp} . Then, (24)

becomes the single-phase (29), which only contains the dielectric constant of bound water:

$$\epsilon_{eff} = (1-\rho)\epsilon_{soil} + W\epsilon_{bound} + (\rho-W)\epsilon_{air} \quad \text{for } W < W_{wp} \quad (29)$$

Secondly, when W is larger than the wilting point but smaller than the porosity, the dielectric constant of water in the soil is a composite of the dielectric constants of bound water and free

water, respectively, according to

$$\varepsilon_{water} = V_{bound} \varepsilon_{bound} + V_{free} \varepsilon_{free} \quad (30)$$

$$\text{with } V_{bound} + V_{free} = 1 \quad (31)$$

The dominant force of bound water is the charge of soil particles, which attracts water molecules and causes them to adhere to the surface of soil particles forming thin layers around the mineral particles. The presence of increasing amounts of water in the soil serves to thicken the thin layer of water molecules, which causes the van der Waals force between these molecules [59] to dominate the force due to the surface charges of the soil particles; as a result the water is able to move freely. This transition point is termed the wilting point, which depends on the size and the characteristic electric charge of the soil particle. Based on this phase transition, we can derive v_{bd} and v_{free} according to

$$\underbrace{\frac{p - w_{WP}}{w - w_{WP}}}_{\substack{\text{Main phase domain} \\ \text{Fig. 3-a)}}} = \frac{1}{\underbrace{V_{free}}_{\substack{\text{Subphase domain} \\ \text{Fig. 3-b)}}}} \quad (32)$$

which is equivalent to

$$V_{free} = \frac{w - w_{WP}}{p - w_{WP}} \quad (33)$$

and then because of (31)

$$V_{bound} = \frac{p - w}{p - w_{WP}} \quad (34)$$

By substituting (33) and (34) into (30), we can translate the main-phase mixing model (24) into a multiphase mixing model :

$$\varepsilon_{eff} = (1 - p) \varepsilon_{soil} + w \left\{ \left(\frac{p - w}{p - w_{WP}} \right) \varepsilon_{bound} + \left(\frac{w - w_{WP}}{p - w_{WP}} \right) \varepsilon_{free} \right\} + (p - w) \varepsilon_{air}$$

for $w_{wp} < w < p$. (35)

Thus, we can calculate the effective dielectric constant by replacing the unknown ϵ_{water} and V_{bound} and V_{free} which are not measurable, with the known constants W_{wp} , ρ , ϵ_{bound} , ϵ_{free} , and the variable W . As a consequence, I obtain the desired relation between W and ϵ_{eff} .

In reality, heavily precipitated water cannot infiltrate the soil medium quickly. In this case, we must consider pure standing water within the observed volume. When W increases above the porosity point, the fraction of standing water over the soil layer increases and the fraction of saturated soil medium (free water with soil particles) decreases due to being out of the observed unit volume. Considering this condition, the standing water fraction can be computed by the relationship

$$\underbrace{\frac{1-\rho}{W-\rho}}_{\substack{\text{Mainphase domain} \\ \text{Fig.3-c)}}} = \underbrace{\frac{1}{V_{standing}}}_{\substack{\text{Subphase domain} \\ \text{Fig.3-c)}}} \quad (36)$$

which is equivalent to

$$V_{standing} = \frac{W-\rho}{1-\rho} \quad (37)$$

Using

$$V_{saturated} + V_{standing} = 1 \quad (38)$$

which, in combination with (18), results in

$$V_{saturated} = \frac{1-W}{1-\rho} \quad (39)$$

Using (37) and (39), we can express the measurable effective dielectric constant with

$$\epsilon_{eff} = \left(\frac{1-W}{1-\rho} \right) \left\{ (1-\rho)\epsilon_{soil} + \rho\epsilon_{free} \right\} + \left(\frac{W-\rho}{1-\rho} \right) \epsilon_{free} \quad \text{for } W > \rho. \quad (40)$$

This is simply equivalent to

$$\epsilon_{eff} = (1-w)\epsilon_{soil} + w\epsilon_{free} \quad \text{for } w > p. \quad (41)$$

In this case, the effective dielectric constant of wet soil can simply be calculated from ϵ_{soil} , ϵ_{free} , and the measured w regardless of the wilting point and porosity.

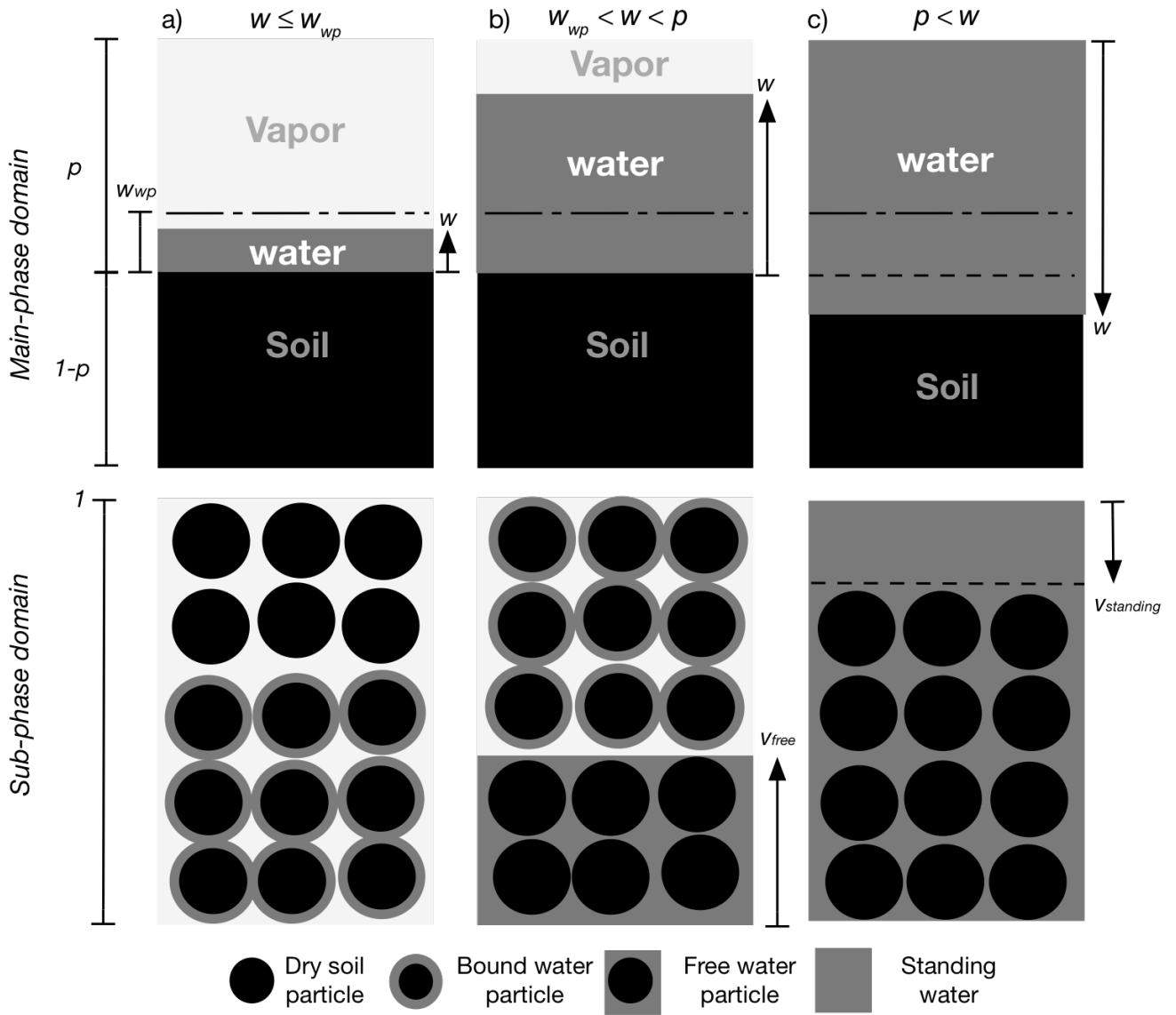


Fig. 7. Illustration of the relation between the variation of soil water content w and the variation of bound and free water fraction in a) dry b) transitional and c) oversaturated conditions

The distinct dielectric properties of bound water (characterized by a low dielectric constant such as that of ice) and free water (high dielectric constant) cause the effective dielectric constant of wet soil (Fig. 7(b)) to become a nonlinear function of w with three domains according to (29), (35), and (41), the boundaries of which are given by w_{wp} and p as shown in Fig. 8.

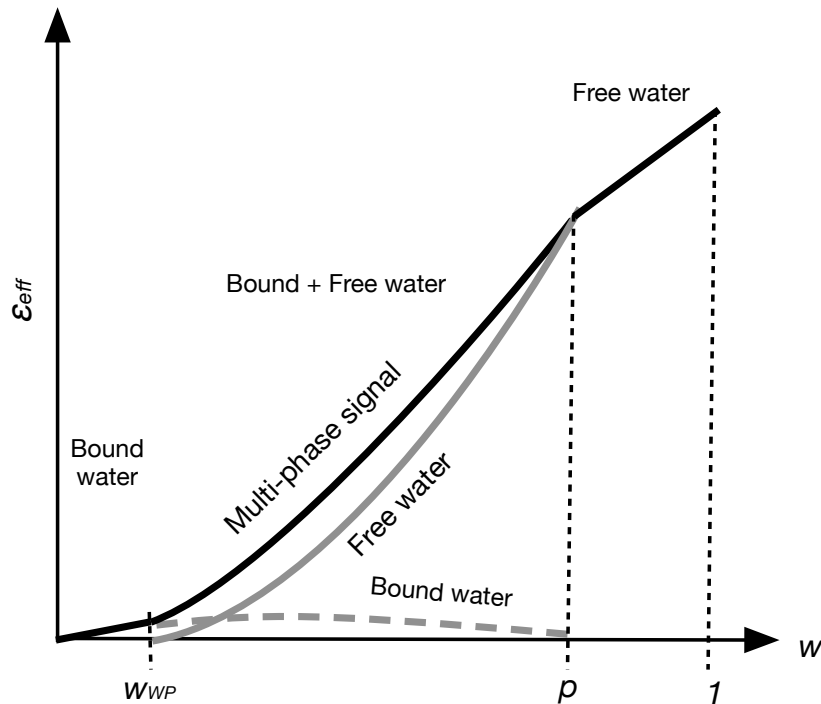


Fig. 8. Multiphase behavior of the effective dielectric constant ϵ_{eff} for different values of the soil water fraction w according to the new approach of (29), (35), and (41), where w_{WP} is the wilting point and p is the porosity, both of which are specific parameters for a given soil texture. The gray solid and dotted curves represent the free and bound water contributions, $w v_{free}\epsilon_{free}$ and $w v_{bound}\epsilon_{bound}$ to ϵ_{eff} , respectively.

2.5 Multiphase-Phase Mixing Model for Conductivity

2.5.1 Soil

The calculation of the effective conductivity was suggested empirically with volumetric mixing ratio of a sand and clay [36], and the bulk electric conductivity of complex materials such as soil and sediments were also proposed [60]. The effective conductivity modeled by these approaches, however, additionally requires various fitting parameters depending on the soil texture and sediment types. By extending the proposed mixing model, we can derive the EC (effective soil conductivity) σ_{eff} without additional empirical parameters. The conductivity σ_{eff} is divided into main phases (dry soil σ_{soil} , soil water with salinity σ_{eff} , and air σ_{air}),

$$\sigma_{eff} = (1-p)\sigma_{soil} + w\sigma_{water} + (p-w)\sigma_{air} \quad (42)$$

For the soil sub-phase, the parallel mixing for the finely layered sand–shale sequence is a composite of sand, which has a very low electric conductivity, and shale, which has a very high electric conductivity [61]. In this study, I subdivide soil into dry soil and wet soil composed of clay, silt, and sand. The dry soil effective conductivity σ_{soil} consists of the sub-phases: sand σ_{sand}^{min} , silt σ_{silt}^{min} , and clay σ_{clay}^{min} (see Table 4) with their volumetric ratio v , thus

$$\sigma_{soil} = v_{silt}\sigma_{silt}^{min} + v_{clay}\sigma_{clay}^{min} + v_{sand}\sigma_{sand}^{min} \quad (43)$$

Table 4 Electrical conductivity (EC) of land surface properties [S/m]

	σ^{\min}	σ^{\max}
Air[62]	3×10^{-15}	8×10^{-15}
Sand[63]	0.3×10^{-3}	30×10^{-3}
Silt[63]	4×10^{-3}	75×10^{-3}
Clay[63]	20×10^{-3}	600×10^{-3}
Salinity[63]	80×10^{-3}	800×10^{-3}
Pure water		10^{-4}
$\bar{\sigma}^*$		0.11

* The ionic conductivity is calculated at a soil temperature of 22 °C and soil salinity of 0.685 ‰

2.5.2 Salinity

The effective conductivity of saline water is simply obtained from the contribution of pure water and its salinity,

$$\sigma_{water} = V_{pure} \sigma_{pure} + V_{saline} \sigma_{saline} \quad (44)$$

$$V_{pure} + V_{saline} = 1 \quad (45)$$

Because the soil water includes almost no volumetric fraction for the solute, we can approximate the pure water sub-phase fraction V_{pure} as 1.

$$V_{pure} = 1 - s \frac{\rho_{solute}}{\rho_{solution}} \approx 1 \quad (46)$$

For the salinity part in (44), I assume that the volumetric partial EC contribution of the salinity

$V_{saline} \sigma_{saline}$ can approximate the ionic conductivity function of temperature T and salinity s [64].

$$V_{saline} \sigma_{saline} \approx \tilde{\sigma} = \sigma_{25^\circ\text{C}}(s) e^{-\varphi(s, 25-T)} \quad (47)$$

where the ionic conductivity for sea water at 25 °C is provided by [64] :

$$\sigma_{25^{\circ}\text{C}}(s) = 0.18252s - 1.4619 \cdot 10^{-3}s^2 + 2.093 \cdot 10^{-5}s^3 - 1.282 \cdot 10^{-7}s^4 \quad (48)$$

where, s is the salinity (‰) and

$$\varphi(s, 25-T) = (25-T) \left(\begin{array}{l} 2.033 \cdot 10^{-2} + 1.266 \cdot 10^{-4}(25-T) \\ + 2.464 \cdot 10^{-6}(25-T)^2 - 1.849 \cdot 10^{-5}s \\ + 2.551 \cdot 10^{-7}(25-T)s - 2.551 \cdot 10^{-8}(25-T)^2s \end{array} \right) \quad (49)$$

2.5.3 Water

The effective conductivity for the soil water part is expressed in terms of the bound water and free water on soil particles.

$$\sigma_{\text{pure}} = V_{\text{bound}}\sigma_{\text{bound}} + V_{\text{free}}\sigma_{\text{free}} \quad (50)$$

The value of EC differs considerably between bound water (counterions) and free water (electrolyte). Clavier *et al.* [65] suggested a value for the effective dielectric conductivity of soil including clay bound water and free water. I assume that the conductivity of bound water is equivalent to the conductivity of its bounded soil particles as shown in (51).

$$\sigma_{\text{bound}} \approx \sigma_{\text{soil}} = V_{\text{silt}}\sigma_{\text{silt}}^{\text{min}} + V_{\text{clay}}\sigma_{\text{clay}}^{\text{min}} + V_{\text{sand}}\sigma_{\text{sand}}^{\text{min}} \quad (51)$$

The conductivity of bound water σ_{bound} in (50) is equivalent to the conductivity of the dry soil σ_{soil} by the approximate relation (51). For the calculation of σ_{free} using (52) the maximum EC value σ^{max} in Table 4 was chosen.

$$\sigma_{\text{free}} = V_{\text{silt}}\sigma_{\text{silt}}^{\text{max}} + V_{\text{clay}}\sigma_{\text{clay}}^{\text{max}} + V_{\text{sand}}\sigma_{\text{sand}}^{\text{max}} \quad (52)$$

Then, we can rewrite the total soil water conductivity σ_{water} as the pure water contribution with ρ and w_{WP} and the salinity contribution, $\tilde{\sigma}$ from (47).

$$\sigma_{\text{water}} = \sigma_{\text{bound}} + (\sigma_{\text{free}} - \sigma_{\text{bound}}) \left(\frac{w - w_{wp}}{\rho - w_{wp}} \right) + \tilde{\sigma} \quad (53)$$

Several studies proved that the computation of the effective conductivity is based on the arithmetic average of the volumetric mixing ratio ([66], [67], and [53]). From this point onwards, the development of the new multiphase mixing model for effective conductivity is described. Similar to (29), (35), and (40), I obtain

$$\sigma_{eff} = (1-p)\sigma_{soil} + w\sigma_{bound} + (p-w)\sigma_{air} \text{ for } w \leq w_{wp} \quad (54)$$

$$\sigma_{eff} = (1-p)\sigma_{soil} + w \left\{ \left(\frac{p-w}{p-w_{wp}} \right) \sigma_{bound} + \left(\frac{w-w_{wp}}{p-w_{wp}} \right) \sigma_{free} \right\} + (p-w) \cdot \sigma_{air}$$

$$\text{for } w_{wp} < w < p \quad (55)$$

and

$$\sigma_{eff} = (1-w)\sigma_{soil} + w\sigma_{free} \text{ for } w > p. \quad (56)$$

The effective electrical conductivity σ_{eff} has a complex form [68]

$$\sigma_{eff} = \sigma'_{eff} + i\sigma''_{eff} \quad (57)$$

where σ'_{eff} represents ohmic conduction and σ''_{eff} refers to the faradaic diffusion loss.

2.6 Complex Dielectric Constant

The complex dielectric constant ε^* consists of the effective polarization term ε'_{eff} as the real part and the effective dielectric loss ε''_{eff} and effective DC (direct current) conductivity σ'_{eff} .

$$\varepsilon^* = \varepsilon'_{eff} + i \left(\varepsilon''_{eff} + \frac{\sigma_{eff}}{\omega \varepsilon_{W0}} \right) \quad (58)$$

The frequency-dependent ε'_{eff} and ε''_{eff} can be derived by, following Debye's relaxation formula [55] for free water, substituting (59) and (60) into (17), (18), and (20).

$$\varepsilon'_{free} = \varepsilon_{W0} + \frac{\varepsilon_{W0} - \varepsilon_{W\infty}}{1 + \omega^2 \tau^2} \quad (59)$$

$$\varepsilon''_{free} = \frac{\omega \tau (\varepsilon_{W0} - \varepsilon_{W\infty})}{1 + \omega^2 \tau^2} \quad (60)$$

where, ε_{W0} is the static dielectric constant of free water computed by Klein and Swift [69], τ is the relaxation time by Stogryn [70] and $\varepsilon_{W\infty}$ was obtained from Lane and Saxton [71]. Section 2.7 presents an investigation to determine whether the static dielectric constant ε_{W0} is physically applied and to determine the effect of the empirically chosen ε_{W0} in the most recent and prevalent refractive mixing approach, as shown in [49, 72].

The averaging approaches for both the effective value of conductivity σ_{eff} and the imaginary part of the dielectric constant ε''_{eff} should be identical in (58).

Then the total dielectric constant ε^* is

$$\varepsilon^* = \varepsilon'_{eff} + i \varepsilon''_{eff} + i \left(\frac{\sigma'_{eff}}{\omega \varepsilon_0} + j \frac{\sigma''_{eff}}{\omega \varepsilon_0} \right). \quad (61)$$

In general, σ''_{eff} is assumed to be 0 and σ'_{eff} is the DC conductivity of the medium [73]. Then, we can approximate the effective conductivity

$$\sigma'_{eff} \approx \sigma_{eff} \quad (62)$$

$$\varepsilon^* = \varepsilon'_{eff} + i \left(\varepsilon''_{eff} + \frac{\sigma_{eff}}{\omega \varepsilon_0} \right) \quad (63)$$

2.7 . Comparison with Other Approaches

Firstly, I compare the general expression of the dielectric mixing and refractive mixing model:

$$\varepsilon_{eff} = a \cdot \varepsilon_{soil} + b \cdot \varepsilon_{bound} + c \cdot \varepsilon_{free} + d \cdot \varepsilon_{air} \quad (64)$$

$$\varepsilon_{eff} = \left(a \cdot \varepsilon_{soil}^\alpha + b \cdot \varepsilon_{bound}^\alpha + c \cdot \varepsilon_{free}^\alpha + d \cdot \varepsilon_{air}^\alpha \right)^{1/\alpha} \quad (65)$$

$$n_{eff} = a \cdot n_{soil} + b \cdot n_{bound} + c \cdot n_{free} + d \cdot n_{air} \quad (66)$$

where, a , b , c , and d is the volumetric mixing ratio for each phase.

To ensure correspondence between the simulation of the effective dielectric constant and the actual measurements, Wang and Schmutge [32] introduced the transition moisture w_t , which is larger than the wilting point. If w_t is utilized to compute b and c in Table 5 according to (33) and (34), the bound water fraction b increases and free water fraction c decreases, thereby causing an underestimation of the effective dielectric constant. Therefore, the use of w_t required the empirical parameter Y to obtain a fit between the predicted and measured effective dielectric constants.

Table 5. list of volumetric mixing ratios in the general expression of the dielectric and refractive mixing formulas

		a	b	c	d	$a+b+c+d$
$w \leq w_{WP}$	Wang&Schmugge [32]	$1-p$	$\frac{w_t - w\gamma}{w_t}w$	$\frac{w\gamma}{w_t}w$	$p-w$	1
	Dobson et al. [36]	$1-p$	0	w^β	$p-w$	>1
	Mironov et al. [49, 72]	1	w	0	$-w$	1
	Park et al. [74]	$1-p$	w	0	$p-w$	1
$w_{wp} < w < p$	Wang&Schmugge [32]	$1-p$	$(1-\gamma)w$	γw	$p-w$	1
	Dobson et al. [36]	$1-p$	0	w^β	$p-w$	>1
	Mironov et al. [49, 72]	1	w_{WP}	$w - w_{wp}$	$-w$	1
	Park et al. [74]	$1-p$	$\frac{p-w}{p-w_{WP}}w$	$\frac{w-w_{wp}}{p-w_{WP}}w$	$p-w$	1
$p \leq w$	Wang&Schmugge [32]	-	-	-	-	-
	Dobson et al. [36]	-	-	-	-	-
	Mironov et al. [49, 72]	-	-	-	-	-
	Park et al. [74]	$1-w$	0	w	0	1

The following equations were used: (64) for Wang & Shmugge and Park *et al.* [74], (65) for Dobson *et al.* and (66) for Mironov *et al.*

Dobson *et al.* [36] adapted the empirical value of 0.65 for α in (65) and β for c that causes the total volumetric ratio to be larger than 1. In the approach of Mironov *et al.* [72] a negative volumetric ratio appears in d . Moreover, the free water dielectric constant reaches unrealistic values of up to 100, which is empirically formulated with the clay-mixing ratio. However, in reality, the dielectric constant of free water is not physically related to the clay-mixing ratio; it is simply the constant value for pure water. In addition, this approach ignores the porosity information in the refractive mixing model (see (66)) and thus fails to obtain an acceptable connection between the soil texture and the effective dielectric constant.

I also investigated a simple calibration model based on the linear relationship between the refractive index $\sqrt{\varepsilon_{eff}}$ and the soil water content w

$$w = a\sqrt{\varepsilon_{eff}} + b, \quad (67)$$

which is widely utilized for GPR applications, where $a = 0.1168$, $b = -0.19$ in [37] and for TDR applications, where $a = 0.1138$, $b = -0.1758$ in [34], $a = 0.1181$, $b = -0.1841$ in [39], and $a = 0.14$, $b = -0.2$ in [41]. This approach has been suggested as the refractive-index mixing approach, which only considers the soil water content. We can express the effective dielectric constant ε_{eff} as a polynomial function of the soil water content w according to

$$\varepsilon_{eff} = \frac{1}{a^2}w^2 - \frac{2b}{a^2}w + \frac{b^2}{a^2}. \quad (68)$$

Equation (68) needs various empirical fitting parameters for different soil textures. This quadratic polynomial calibration model was also proposed for microwave remote sensing by Hallikainen [52] with

$$\varepsilon_{eff} = (c_0 + c_1v_{sand} + c_2v_{clay})w^2 + (b_0 + b_1v_{sand} + b_2v_{clay})w + (a_0 + a_1v_{sand} + a_2v_{clay}). \quad (69)$$

Compared to (68), (69) is not only a function of the soil water content w , but also of the soil texture. Therefore, the model is able to simulate the effective dielectric constant in various soil textures with good agreement to the measurements; however, it also requires nine empirical fitting parameters $a_{0,1,2}$, $b_{0,1,2}$, and $c_{0,1,2}$.

We can rewrite our physically based new model for the mixed status of bound and free water (35) in terms of w in the following way

$$\varepsilon_{eff} = \frac{\varepsilon_{free} - \varepsilon_{bound}}{p - w_{wp}}w^2 + \frac{p\varepsilon_{bound} - w_{wp}\varepsilon_{free}}{p - w_{wp}}w + (p - w)\varepsilon_{air} + (1 - p)\varepsilon_{soil}. \quad (70)$$

The fitting parameters of the empirical polynomial models originate from the combination of the dielectric constants ε_{bound} and ε_{free} and the physical soil properties w_{wp} and p as shown in

(70). As a result, we can estimate the soil water content from the dielectric measurements without creating several empirical parameters or different calibrations for different soil conditions; the only unknown parameter, which cannot be resolved, is ϵ_{bound} . However, this single parameter can be determined by comparing the mixing model with observations.

2.8 Bulk Dielectric Mixing with Damping

When the medium is considered to be 3D (three-dimensional) and not flat, the geometrical structure and thickness become relevant. For example, the effective value of the polarization density P should be reduced by $1/3$, a number termed the depolarization factor for the spherical shape [22]. The non-spherical shape effect of soil particles in saturated and unsaturated porous media was reviewed by [75]. Recent studies showed that by increasing the thickness of a medium, the effective value of the dielectric constant decreases [45, 76-78]. In short, a reduction of the bulk dielectric constant compared to the flat 2D dielectric constant is attributable to both the 3D microgeometry and the thickness of the medium. In the following part of this section, I idealize the complex morphology of the land surface properties found in nature and consider the soil as isotropic. Thus, in order to consider dielectric constant in 3D aspect, I focus on the damping effect within the sampling depth of instrument, such as a penetration depth of TDR or GRP or an emission depth of SMOS or SMAP, which will be described further in the following section.

The sampling depth refers to the thickness at which the surface emission is determined by its dielectric constant [79]. Ultimately, the energy emitted from this layer is remotely sensed by instruments [80]. In other words, the signal detected over a surface is not only related to the arithmetic average of the dielectric constant of soil properties discussed in Section III, but also determined by the sampling depth, which is considered with the damping factor in this section. Knowing the depth from which the signal originates is important for the soil moisture estimation with remotely sensed measurements. With increasing sampling depth, the contribution of the signal from that depth to the average signal intensity becomes smaller and smaller. Without considering attenuation, the quantification of soil moisture content from surface emission is underestimated. The computation of the surface emission from the sampling

depth is related to a nonlinear weighting function, such as a decaying function with depth [81]. Wilheit [82] proposed a layered model for the electric field in the distinct interface between air (free space) and the soil surface. The medium under the surface layer is assumed as homogenous, which then can be described by Beer-Lambert's law. The interface provides one boundary condition for Maxwell's equations, namely

$$E_0 = \bar{E} + E_{dep} \quad . \quad (71)$$

The incident electric field E_0 is equivalent to the sum of the macroscopic electric field \bar{E} and the depolarization field E_{dep} . In the layer model, the attenuation of the electric field during the wave propagation from one layer to the next is derived with the propagation function that is governed by Beer-Lambert's law. The law describes the decrease of the intensity of radiation with depth z according to

$$\frac{I(z)}{I(0)} = \exp\left(-\frac{z}{\delta}\right) \quad (72)$$

where δ is the penetration depth [83]. The penetration depth for the vertically uniform soil profile can be simplified with the imaginary part of the refractive index n'' and the wavelength λ

$$\delta = \frac{\lambda}{4\pi n''} \quad (73)$$

The microwave penetration depth has been studied for various soil textures [84]. Depending on the type of material, $n_{eff}^{2D''}$ determines δ . On the other hand, the mixed medium has a penetration depth referred to as the effective penetration depth δ_{eff} , which is determined with the effective value of $n_{eff}^{2D''}$. If the distribution pattern of material is isotropic, the vertical distribution pattern (2D cross section) is identical to the horizontal 2D distribution pattern. As discussed in the

following, I believe that the effective penetration depth depends in an analogous way on the imaginary part of the effective refractive index, $n_{eff}^{2D''}$, namely the effective penetration depth is

$$\delta_{eff} = \frac{\lambda}{4\pi n_{eff}^{2D''}}. \quad (74)$$

where $n_{eff}^{2D''}$ can be derived from (29), (35), and (41), which was originally invented for parallel mixing, by

$$n_{eff}'' = \text{Im}\left(\sqrt{\epsilon_{eff}}\right). \quad (75)$$

Following (72), the electric field of the electromagnetic wave can be expressed as

$$\frac{\bar{E}(z)^2}{\bar{E}(0)^2} = \exp\left(-\frac{z}{\delta_{eff}}\right). \quad (76)$$

Then, we can describe the electric field at any depth by

$$\bar{E}(z) = \bar{E}(0) \exp\left(-\frac{z}{2\delta_{eff}}\right). \quad (77)$$

By integrating the 2D surface polarization density P_{eff}^{2D} (see equation (21)) with equation (77) up to the depth z , we get the following 3D averaging equation for the isotropic mixing medium

$$P_{eff}^{3D} = \frac{1}{z} \int_0^z P_{eff}^{2D}(z) dz = \epsilon_0 \chi_{eff}^{2D} \bar{E}(0) \frac{1}{z} \int_0^z \exp\left(-\frac{z}{2\delta_{eff}}\right) dz \quad (78)$$

and thus,

$$P_{eff}^{3D} = \epsilon_0 \chi_{eff}^{2D} \bar{E}(0) \frac{2\delta_{eff}}{z} \left(1 - \exp\left(-\frac{z}{2\delta_{eff}}\right)\right). \quad (79)$$

Equation (79) can be expressed with the initial electric field component $\bar{E}(0)$ and the effective electric susceptibility of a 3D substance χ_{eff}^{3D} as

$$P_{eff}^{3D} = \epsilon_0 \chi_{eff}^{3D} \bar{E}(0) \quad (80)$$

Then the new effective electric susceptibility is

$$\chi_{eff}^{3D} = \chi_{eff}^{2D} H_z \quad (81)$$

where

$$H_z = \frac{2\delta_{eff}}{z} \left(1 - \exp\left(-\frac{z}{2\delta_{eff}}\right) \right) \quad (82)$$

In other words, the final solution for an isotropic medium requires the effective susceptibility obtained simply by parallel mixing and an attenuation factor H_z .

The electric susceptibility is related to the dielectric constant according to

$$\chi_{eff}^{3D} = \epsilon_{eff}^{3D} - 1 \quad (83)$$

Thus, we obtain a 3D effective dielectric constant for a heterogeneous medium according to

$$\underbrace{\epsilon_{eff}^{3D}}_{\text{bulk}} = \left(\underbrace{\epsilon_{eff}^{2D}}_{\text{uppermost thin layer}} - 1 \right) \underbrace{H_z}_{\text{damping factor}} + 1 \quad (84)$$

Inserting the attenuation factor H_z into the multiphase model of equation (29), (35) and (41), we obtain the real part of the 3D effective dielectric constant

$$\epsilon_{eff}^{\prime 3D} = (\epsilon_{eff}' - 1) H_z + 1 \quad (85)$$

and for the imaginary part, we obtain

$$\epsilon_{eff}^{\prime\prime 3D} = \epsilon_{eff}^{\prime\prime} H_z.$$

If the sampling of the soil layer is obtained with penetration depth δ_{eff} , one needs to insert δ_{eff} for z in (82) and H_z becomes a constant H_δ , which is independent of the wavelength and extinction coefficient and has the value

$$H_\delta = 2 \left(1 - \exp(-0.5) \right) \approx 0.8 \quad (87)$$

Indeed, we found this simple selection of the integration limit δ_{eff} for z in (78) to provide the best results compared to the experimental values, as shown below.

In summary, the forward model operator, which is based on physical parameters, was obtained by combining the multiphase dielectric mixing model and the damping function.

2.9 Results

The proposed multiphase model translates links between the main-phase, which have to be estimated as model states, and the sub-phases, of which the optical characteristics can be captured by the sensor. I obtained w_{WP} and ρ from the STATSGO (State Soil Geographic) Data Base [85] (Table 6). These soil properties determine the nonlinear behavior in the calculation of the effective dielectric constant.

Table 6. Volumetric mixing ratio (%) of soil texture, wilting point, and porosity

	Sand	Sandy loam	Silt loam	Clay loam	Silt clay	Clay
Sand (%)	100.0	51.5	17.2	35	5.0	15
Silt (%)	0.0	35.0	63.8	30	47.6	20
Clay (%)	0.0	13.5	19.0	35	47.4	65
Wilting point (cm^3/cm^3)	0.010	0.047	0.084	0.103	0.126	0.138
Porosity (cm^3/cm^3)	0.339	0.434	0.476	0.465	0.550*	0.550*

Soil texture data were obtained from [51] and porosity from STATSGO Data [cm^3/cm^3] [82]; * increased porosity to match the maximum measurement point.

The consistent performance of the new approach in predicting the effective dielectric constant was compared by utilizing the four most prevalent dielectric mixing models.

The published values of the dielectric constants for the bound water and the dry soil are listed in Table 7. The Wang-and-Schmugge model has a smaller dielectric constant for bound water compared to other approaches. The model of Dobson *et al.* does not deal separately with bound and free water but integrates them into a dielectric constant of water. For the comparison

with Mironov *et al.* [72], I simulated the effective dielectric constant with two conditions (referred to as Mironov *et al.*-1 and Mironov *et al.*-2). Mironov *et al.*-1 is the originally proposed refractive mixing model ([49, 72]) which uses a static dielectric constant of free water ϵ_{w0} of 100 in (59) and (60). Such a value does not realistically represent the pressure at the land surface. This empirical choice in Debye's relaxation formulas (59) and (60) yields greater values for the dielectric constants for both the real and imaginary parts in Mironov *et al.*-1 compared to other approaches. Mironov *et al.*-2 is our modification with the physically known ϵ_{w0} for pure water of 80, which is the same value that is used in the remainder of the approaches, including our approach. This value can either be measured [86] or modeled [69] at 20 °C with the surface pressure level 0.1 MPa. In our approach, the free water dielectric constant is computed from Debye's equations, (59) and (60).

Table 7. Complex dielectric constant for land surface properties

Microwave	Free water			Bound water			Soil	Air [87, 88]	
	L	C	K	L	C	K			
Mironov et al.-1	ϵ'	99.5	93.7	43.9	79.1(1)	62.0(2)	29.8(2)	2.67-1.88 [72]	1.0
					68.3(2)				
					64.2(3)				
	ϵ''	7.1	23.7	47.5	53.4(4)	19.4(3)	29.9(3)	0.13-0.002 [72]	0.0
					46.2(5)				
					37.7(6)				
Mironov et al.-2	ϵ'	79.6	75.0	43.9	*	*	*	*	1.0
	ϵ''	5.6	18.7	37.5	*	*	*	*	0.0
Wang& Schmugge	ϵ'	79.6	73.1	41.3		3.15[32]		5 [87, 88]	1.0
	ϵ''	6.1	23.8	38.2		0.0 [32]		0.078 [87, 88]	0.0
Dobson et al.	ϵ'	79.6	73.1	41.3		35 [36]		4.67 [36]	1.0
	ϵ''	6.1	23.8	38.2		5 [36]		0 [36]	0.0
Park et al.	ϵ'	79.6	73.1	41.3	48.0(1), 38.2(2), 32.4(3), 29.7(4), 22.4(5), 18.3(6)			5.0 for clay & loam 3.0 for sand [87, 88]	1.0
	ϵ''	6.1	23.8	38.2	1.0(1), 3.6(2), 5.3(3), 5.4(4), 7.2(5), 7.7(6)			0.078 for clay, loam, and sand [87, 88]	0.0

Bound water: (1) sand, (2) sandy loam, (3) silt loam, (4) clay loam, (5) silt clay, (6) clay * same value as Mironov *et al.*-1

The optimal bound water dielectric constant for the imaginary part and the real part has been determined as the following formulations,

$$\epsilon'_{bound} = 48 v_{sand} + 36 v_{silt} + 6 v_{clay} \quad (88)$$

and

$$\epsilon''_{bound} = v_{sand} + 5 v_{silt} + 10 v_{clay}$$

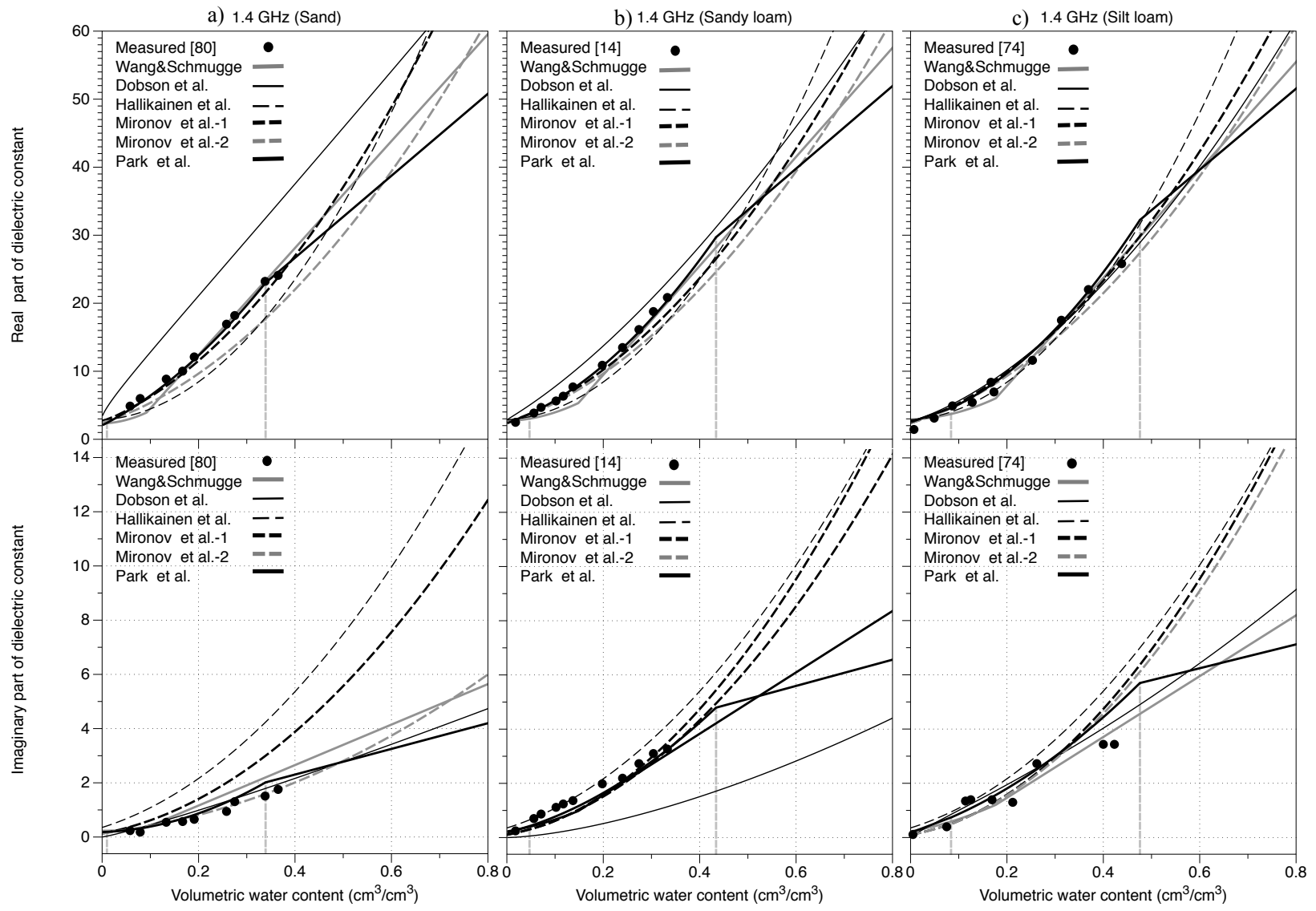
to complete the mixing formulas (29), (35), and (40).

In Table 8 the RMSE between the simulation results obtained with our novel model and the measured data, was calculated with

$$RMSE = \sqrt{\frac{1}{n} \sum_{t=1}^n (\varepsilon_{t,eff}^{3D} - \varepsilon_{t,measured})^2} \quad (89)$$

Each approach was calibrated or empirically designed based on the limited availability of their dielectric measurements.

However, considering that the purpose of this modeling is the operational usage of microwave remote sensing for soil moisture estimation on a global scale, the consistent performance of the dielectric prediction with reasonable accuracy, in general, is more important than obtaining high accuracy only in specific cases. Therefore, I next examined the approach involving the most reliable dielectric mixing model for microwave remote sensing in the L-band (Fig. 9), C-band (Fig. 10), and K-band (Fig. 11) over various soil textures through assessment of the RMSE value. In this analysis, I examined whether the wilting point and porosity are really the critical factors required to predict the effective dielectric constant and whether the physically based approach consistently performs well in predictions compared to other semi-empirical and calibration approaches.



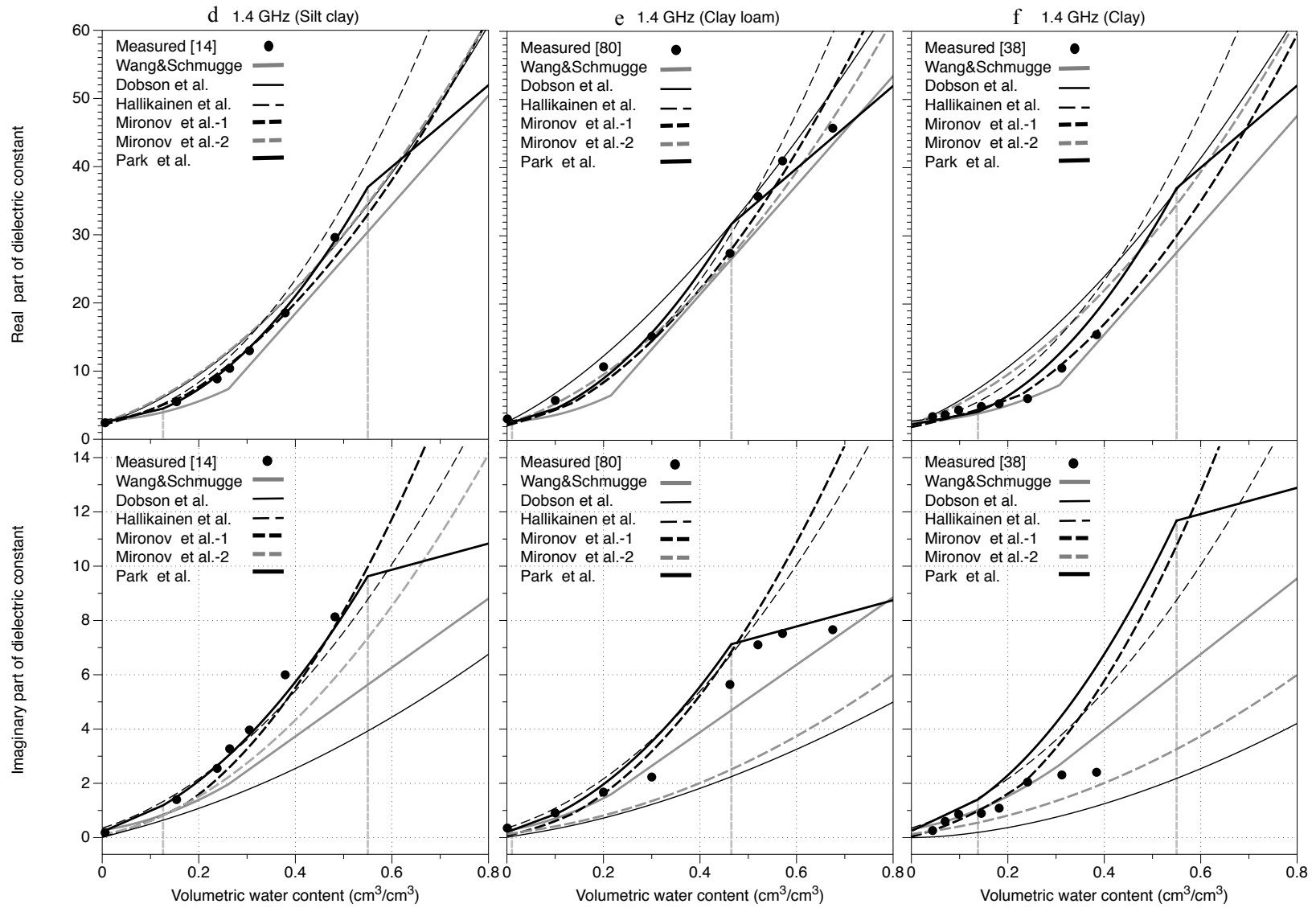


Fig. 9. Comparison of the effective dielectric constant in the L-band region for five soil textures from sand to clay predicted by our approach, Wang & Schmugge [32], Dobson et al. [36], Hallikainen et al. [52], Mironov et al. [89], and Park et al. [74] with the measured points obtained from [36], [32], [74, 88, 90](vertical lines indicates wwp and p).

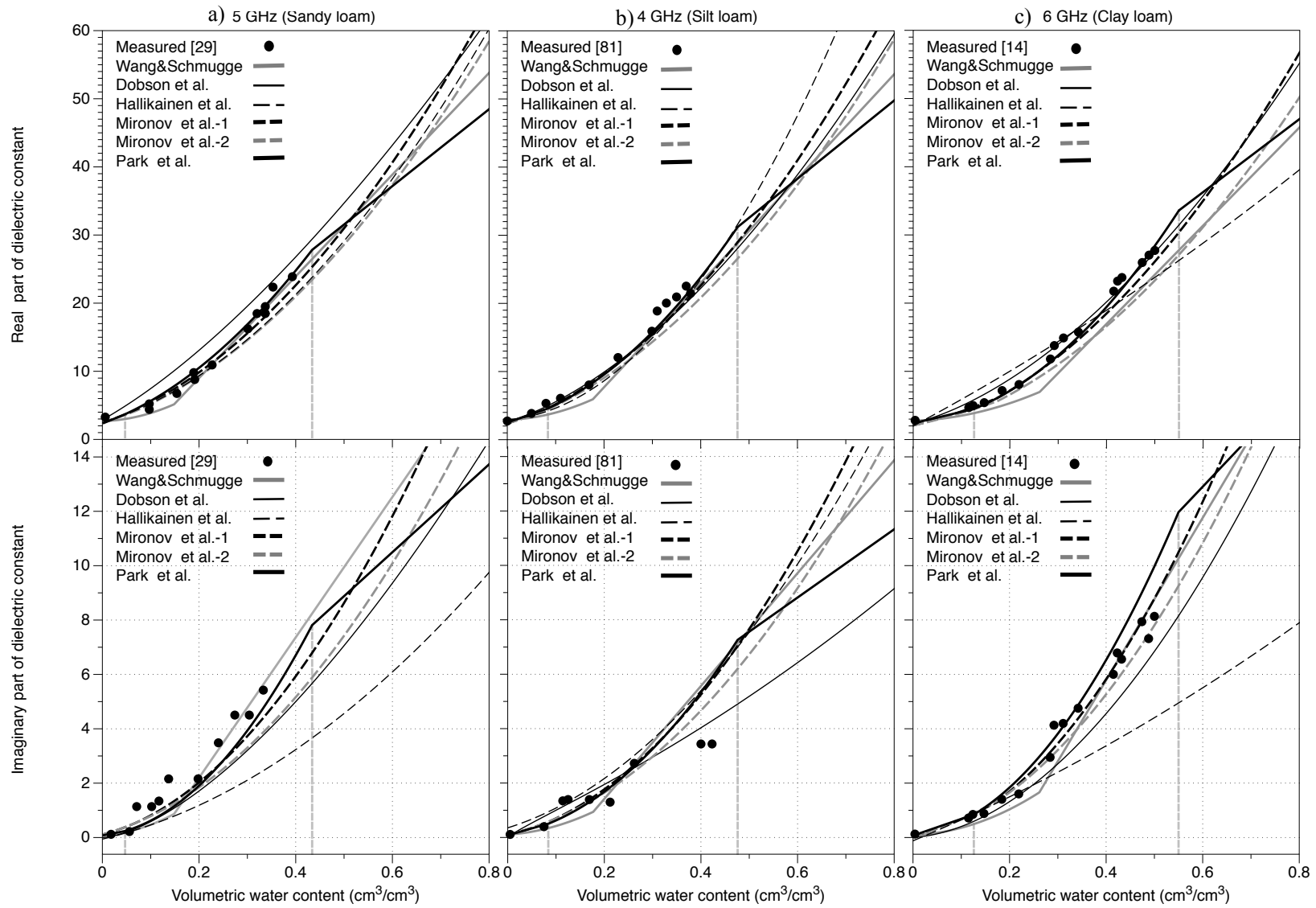


Fig. 10. Comparison of the C-band effective dielectric constant predicted by our approach, Wang & Schmugge, Dobson et al., Hallikainen et al., and Mironov et al. with measured points obtained from [36], [52], and [91] (vertical lines indicates w_{wp} and p).

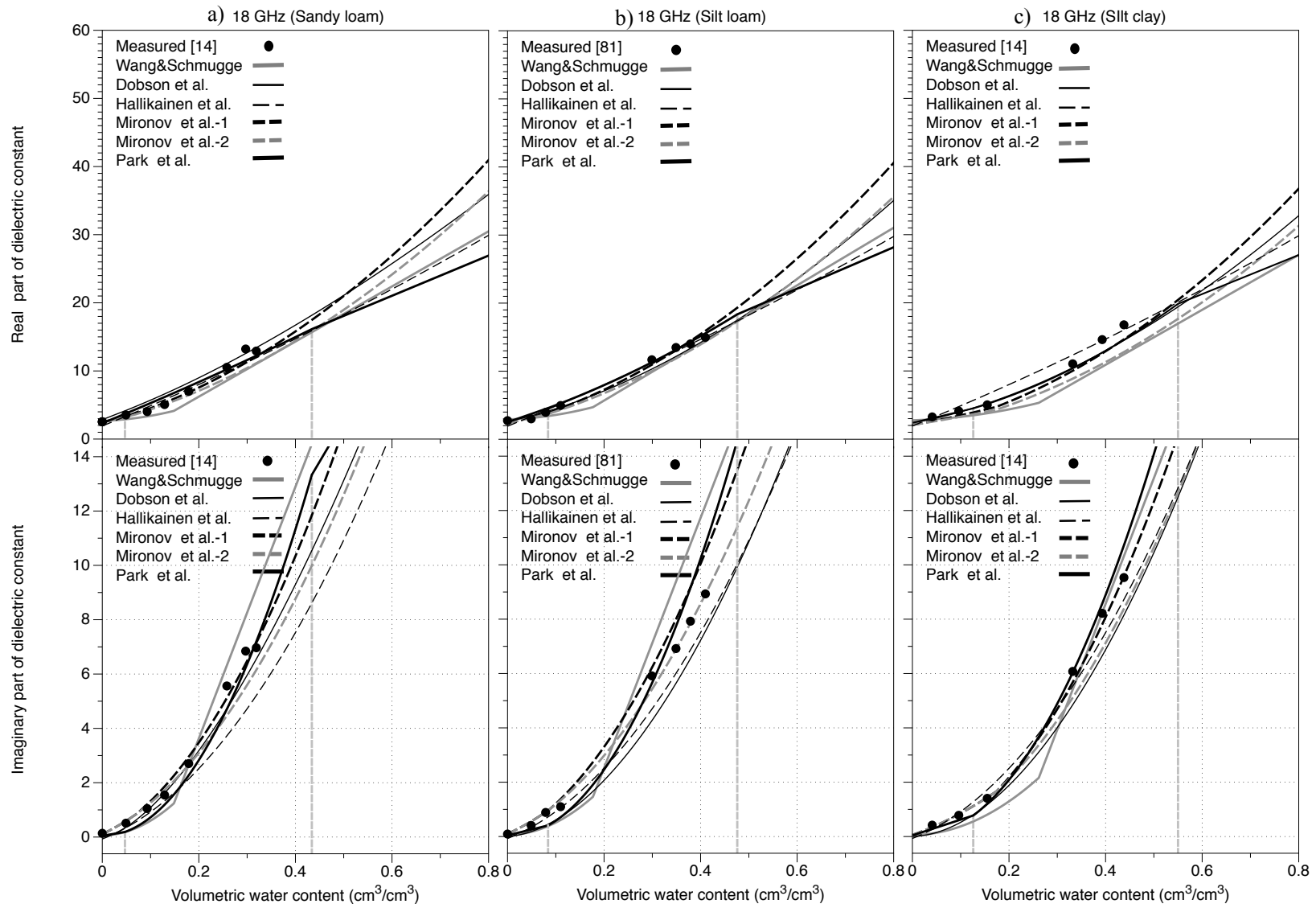


Fig. 11. Comparison of the K-band effective dielectric constant predicted by our approach, Wang & Schmugge , Dobson et al., Hallikainen et al., and Mironov et al. with measured points obtained from [36] and [91] (vertical lines indicates wwp and p).

Dobson's model [36] was proposed based on the evaluation and calibration of five soil texture values from sandy loam to silt clay for which the sand mixing ratio ranged from 5 to 51%. The simulation for pure sand by this model revealed a highly overestimated dielectric constant in the real part as shown in Fig. 9(a) (e.g., 27 instead of 18 for $w = 0.275$, i.e., a 50% overestimation). Other approaches, such as that of Wang & Schmugge [32] and that of Hallikainen *et al.* [52], generally underestimate the dielectric constant in such a situation and, therefore, result in excessively large values of soil moisture resulting from the dielectric measurements. On the other hand, the values obtained with our model were in good agreement (e.g., only a 3% underestimation for $w = 0.275$) with the dielectric constant measurements of wet sand, also capturing the oversaturated condition above the porosity point. The models of Mironov *et al.* [89] and Hallikainen *et al.* [52] largely overestimate the imaginary part of the dielectric constant (e.g., 67% and 144% overestimated in $w = 0.275$, respectively (see Fig. 9(a)), whereas other models including ours more closely correspond with the measurements (e.g., an 18% overestimation for $w = 0.275$). When we compare the predictions of various models along the gradient of increasing clay content (see Fig. 9(a) to (f)), the dielectric predictions for the real part are similar amongst the models; in general, all the predictions are in good agreement with the measured values of the dielectric constants. However, the models show significantly different performances in the prediction of the imaginary part. Considering the modeled curve for the imaginary part shown in Fig. 9(a), (d), and (e), by increasing clay contents, our model is in good agreement for both sand and clay loam with values of 0.25 and 0.72, respectively, regarding the RMSE score in Table 8, both of which are approximately four times less than the RMSE score of Mironov *et al.* [89]. On the other hand, other approaches show a slight shift according to the variation in clay content, thereby causing overestimation and underestimation problems for the sand and the clay loam in the prediction of the imaginary part. The improved

performance of our model is attributed to the physically based mixing approach for the computation of effective conductivity similar to the mixing model for the real part of effective dielectric constant. For the clay case (Fig. 9(f)), our model shows an overestimation problem. One of the possible reasons might be a swelling process of heavy clay in the oversaturated soil condition. A significantly larger porosity of the sampled clay soil than the value that I applied in our model (0.550 in Table 6) might cause this disagreement.

For higher frequencies, such as the C- (Fig. 10) and K- bands (Fig. 11), the dielectric difference of the bound water and free water decreases, as shown in Table 7, and the wilting point and porosity of the soil texture are less significant in the prediction of the effective dielectric constant. Therefore, as shown in Fig. 10 and Fig. 11, the C- and K- band predictions of all the models from the soil water to the dielectric constant or vice versa are less diverse than the L-band prediction.

Overall, the physical adaption of the static dielectric constant of free water in Mironov *et al.*-2 resulted in a larger RMSE than Mironov *et al.*-1 which introduced the empirical value for the static dielectric constant of pure water as 100. However, our physical-based approach proved to be 15% more accurate than Mironov *et al.*-1 and 50% more accurate than other approaches for the real part. For the imaginary part, it shows the same performance as Mironov *et al.*-1 and is 40% more accurate than the other approaches. For the L-band, our model is 13% more accurate than Mironov *et al.*-1 and 66% more accurate than other approaches regarding the real part and 28% more accurate than Mironov *et al.*-1 and 48% more accurate than other approaches regarding the imaginary part.

Table 8. RMSE scores of the effective dielectric constant predicted by the approaches shown in

Figs. 8 - 10

Soil texture	Sand	Sandy loam	Silt loam	Silt clay	Clay loam	Clay	Sandy loam	Silt loam	Silt clay	Sandy loam	Silt loam	Silt clay
Real part			L-band				C-band			K-band		
Wang&Schmugge	1.34	1.40	1.21	0.96	3.44	1.08	0.96	1.77	2.75	1.66	1.01	2.75
Dobson et al.	8.06	2.21	1.12	2.86	2.87	4.77	2.86	1.52	0.93	0.98	0.74	1.25
Hallikainen et al.	3.96	2.33	1.15	1.93	5.22	3.38	1.93	1.69	2.46	0.94	0.43	1.25
Mironov et al.-1	2.78	1.79	1.09	2.04	4.03	0.68	2.04	2.40	3.20	1.34	0.96	2.44
Mironov et al.-2	1.15	0.43	1.15	0.82	2.51	0.69	0.82	1.04	1.65	0.71	0.63	1.67
Park et al.	0.47	0.33	1.11	0.91	1.98	1.77	0.91	0.97	1.03	0.89	0.45	1.23
Imaginary part			L-band				C-band			K-band		
Wang&Schmugge	0.45	0.35	0.74	1.78	0.91	0.52	0.50	0.61	0.66	0.98	1.83	0.53
Dobson et al.	0.22	1.38	0.28	0.60	2.92	1.01	0.66	0.27	1.05	0.52	1.11	1.01
Hallikainen et al.	1.78	0.39	1.12	0.56	1.85	1.19	1.47	0.69	2.13	1.21	0.77	1.01
Mironov et al.-1	1.15	0.35	0.63	0.56	2.51	1.14	0.71	0.71	0.44	0.28	0.81	0.24
Mironov et al.-2	0.82	0.38	0.73	0.61	2.12	1.12	0.44	0.44	0.54	0.68	0.20	0.82
Park et al.	0.25	0.26	0.64	0.33	0.72	1.68	0.70	0.87	0.88	0.47	0.87	0.52

Gray boxes indicate the best performance

Table 9. RMSE score averaged over soil textures for L, C, and K band wavelengths

		Wang & Schmugge	Dobson et al.	Hallikainen et al.	Mironov et al.-1	Mironov et al.-2	Park et al.
Real part	L	1.78	3.78	3.13	1.12	2.27	0.98
	C	1.99	1.77	2.03	1.17	2.55	0.97
	K	1.81	0.99	0.87	1.00	1.58	0.86
Average		1.86	2.44	2.22	1.13	2.10	0.96
Imaginary part	L	0.75	1.46	1.20	0.82	0.94	0.59
	C	0.68	0.66	1.43	0.50	0.54	0.63
	K	1.11	0.88	1.00	0.24	0.57	0.61
Average		0.82	1.08	1.18	0.64	0.76	0.63

Gray boxes indicate the best performance

Table 10. Number of black boxes in Table 8 showing the number of times a model provided the most accurate performance of all the models that were used

		Wang & Schmugge	Dobson et al.	Hallikainen et al.	Mironov et al.-1	Mironov et al.-2	Park et al.
Real part	L	0	0	0	2 (1)	0	4 (2)
	C	0	1	0	0	1	1
	K	0	0	1	0	1	1
Imaginary part	L	1 (0.5)	2 (1)	0	0	0	3 (1.5)
	C	0	1	0	1	1	0
	K	0	0	0	2	1	0
Total		0.5	3	1	4	4	5.5
Normalized score		0.03	0.17	0.05	0.22	0.22	0.31

Numbers in brackets are the numbers for the L-band divided by 2 because collected cases for L band were double those of the C and K bands; these bracketed numbers are the weighted scores comparable to those of the C and K bands. They are used for the overall total score. Gray boxes mark the model which performs best.

2.10 Discussion

Previous models focused on the prediction of the dielectric constant of wet soil below the porosity point. The simulation of the dielectric constant for $w > \rho$ has not been studied using the previous dielectric or refractive mixing models although the prediction of the effective dielectric constant in this range could potentially facilitate the tracking of rain events, in estimating the infiltration capacity of the surface, and in mapping flooded areas via surface microwave remote sensing. The contribution of our novel physical-based approach is that it includes the less frequent but important case of oversaturation. Because of the lack of measurement data for this case in the literature, I could only validate the prediction in this range with data for clay loam at 1.4 GHz [32], as shown in Fig. 5(e). These measured dielectric constant data show a change in gradient when w becomes larger than ρ . Our new approach reflects this behavior and indeed simulates dielectric constant data which are linearly proportional to w for $w > \rho$ (see (22)), whereas none of the previous models displayed this capability; for example, the approach of Mironov *et al.* which is the current baseline dielectric mixing model both for SMOS [92] and SMAP satellites ([93, 94]) shows that both the real and imaginary parts of the dielectric constant increase exponentially for $w > \rho$, which leads to unrealistically low BTs. In this regard the different frequency regions behave differently; particularly in the L-band, significant differences are found between our new model and previous models. It should be noted, however, that this concept requires more extensive validation with measurements.

The best approach among the various soil types and wide range of microwave frequencies (L-, C-, and K-bands) was identified by counting the cases in which a model provided the best

RMSE score. To account for the higher number of comparisons for the L-band (six) instead of three for each of the other bands, I finally divided the score for the L-band by 2 to arrive at the overall performance scores in Table 10. An analysis of the results in Table 10 indicates that our new approach performs best with a normalized total score of 0.315 compared to the models of Wang & Schmugge [32], Dobson *et al.* [36], and Hallikainen *et al.* [52], which produced scores of 0.035, 0.172, and 0.05, respectively. The model of Mironov *et al.* [49, 72] also produced a comparatively high score of 0.22, but this is 10% less than the result obtained with our new model. Furthermore, as discussed above, this model is not physically based and requires several fitting parameters.

3. Radiative Transfer Model

3.1 Brightness Temperature Scaled on Spaceborne Measuring System

In this section, I combine the effective dielectric constant computed by using the physical-based novel dielectric constant derived in Section II with the existing radiative transfer model to simulate the BT. In respect of the spatial resolution of space borne remote-sensing measurements, such as SMAP and SMOS, we need to define the measurable scale BT as an anisotropic BT measurement with isotropic effective dielectric constants as shown in Fig. 12.

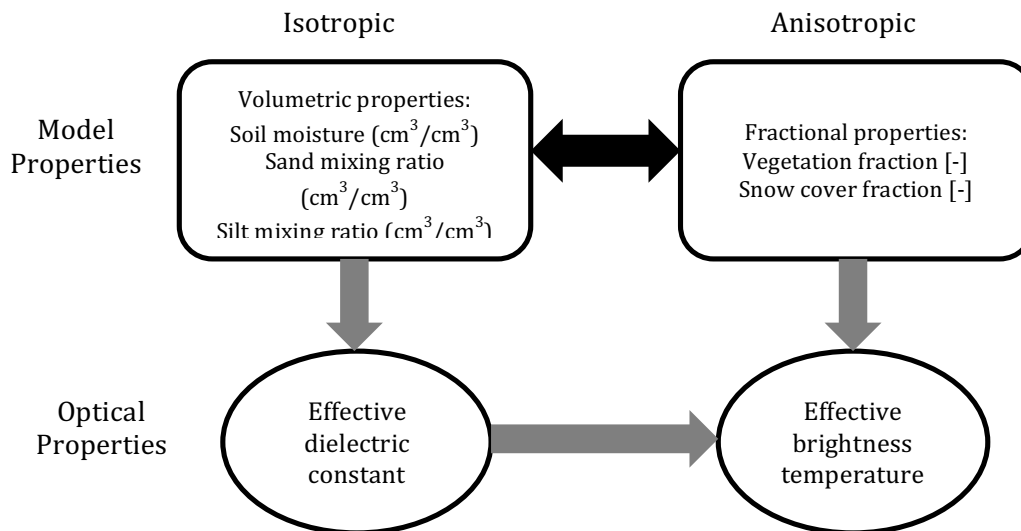


Fig. 12. Computation of the effective BT using the land surface model properties at the scale of the space-borne remote-sensing sensor.

Understanding the difference between isotropic and anisotropic computation is important for the accurate quantification of land surface properties derived from large-scale remote sensing of the land surface. Fig. 12 indicates which components in the forward model should be considered for isotropic and anisotropic approaches. Generally, the effective dielectric constant and volumetric parameter of the land surface model are isotropic properties. The microwave penetration depth

for the particular soil medium is approximately 2 cm [95], for which soil moisture retrieval against emissivity ([96, 97]) was performed at a depth of 0 – 2 cm assuming the soil water is homogeneously distributed. Therefore, the effective dielectric constant can also be assumed to be constant. The soil moisture captured in the scale of the field of view (FOV) of SMOS and SMAP was estimated by considering the volumetric (isotropic) and fractional (anisotropic) properties in the forward simulation. If we could succeed in describing the relationship between the volumetric and fractional properties indicated by the black arrow in Fig. 12 via physical or statistical modeling, we could avoid the ill-posed problem by reducing two unknowns into one, that is, either a volumetric or a fractional parameter. An example of this kind of solution would be the statistical model between the maximum value and the spread of the property in the sub-grid. This approach would allow us to realistically estimate the soil moisture from the BT measurement of space-borne remote sensing.

3.2 Column-Integrated Brightness Temperature

The blackbody radiance is calculated using the absolute temperature T of the medium and the wavelength of the observed electromagnetic wave λ with additional constants (where h is Planck's constant, k_b is the Boltzmann constant, and c is the speed of light) according to Planck's function.

$$B(T, \lambda) = \frac{2hc^2}{\lambda^5} \left(\exp\left(\frac{hc}{\lambda kT}\right) - 1 \right)^{-1} \quad (90)$$

The radiance measured on the remote-sensing sensor is composed of the atmospheric contribution and the emission of the top of the vegetation attenuated by atmospheric transmissivity.

$$B(T_{TOA}, \lambda) = B(T_{ATM}, \lambda) + t_{ATM} B(T_{TOV}, \lambda) \quad (91)$$

The emitted BT across the top of the vegetation is composed of the canopy contribution and soil contribution as follows.

$$B(T_{TOV}, \lambda) = (1 - t_c)(1 + t_c r_s) B(T_c, \lambda) + t_c (1 - r_s) B(T_s, \lambda) \quad (92)$$

For microwave remote sensing, we can simply substitute (91) and (92) into

$$B(T_{TOA}, \lambda) = (1 - t_c)(1 + t_c r_s) B(T_c, \lambda) + t_c (1 - r_s) B(T_s, \lambda) \quad (93)$$

with the approximations,

$$B(T_{ATM}, \lambda) \approx 0 \quad (94)$$

$$\text{and } t_{ATM} \approx 1. \quad (95)$$

In the long wavelength range, such as for microwave radiation, we can also approximate (90) with the Rayleigh-Jeans law.

$$B(T, \lambda) \approx \frac{2kT}{\lambda^2} \quad (96)$$

Then, we can rewrite (93) as follows:

$$T_{TOA} = (1 - t_c)(1 + t_c r_s) T_c + t_c (1 - r_s) T_s \quad (97)$$

The top of the atmosphere is the surface layer of the Earth from which the microwaves are ultimately emitted and registered on the sensor, and this emission is referred to as *BT* in this study.

$$BT = (1 - t_c)(1 + t_c r_s) T_c + t_c (1 - r_s) T_s \quad (98)$$

This equation tells us that the determination of the measured temperature on the microwave sensor, referred to as the BT, across the top of the vegetation or the top of the atmosphere not

only depends on the absolute temperature of the canopy and soil, but also on their respective optical properties t_c and r_s . Ultimately, the BT measured by the microwave sensor contains the temperature information and optical properties of the soil and canopy. In Section III-C, we show how the optical properties t_c and r_s are determined by obtaining the volumetric information of the soil and canopy water, the soil texture, and the type and height of the canopy. The isotropic effective dielectric constant is utilized to compute the effective reflectivity of the soil layer and the effective transmissivity of the canopy layer.

3.3 Reflectivity of Soil, r_s , from Isotropic Dielectric Constant

The computed effective dielectric constant is a key parameter to simulate the BT of the soil observable on remote-sensing sensors. The reflectivity of two polarization directions is related with the effective dielectric constants of soil, ϵ'_{eff} , ϵ''_{eff} , and the incident angle of light θ_i according to the Fresnel equation.

$$r_h = \frac{\left| \cos \theta_i - \sqrt{\frac{\sqrt{\epsilon'_{eff}{}^2 + \epsilon''_{eff}{}^2} + \epsilon'_{eff}}{2} - \sin^2 \theta_i} \right|^2}{\left| \cos \theta_i + \sqrt{\frac{\sqrt{\epsilon'_{eff}{}^2 + \epsilon''_{eff}{}^2} + \epsilon'_{eff}}{2} - \sin^2 \theta_i} \right|^2}, \quad (99)$$

$$r_v = \frac{\left| \epsilon'_{eff} \cos \theta_i - \sqrt{\frac{\sqrt{\epsilon'_{eff}{}^2 + \epsilon''_{eff}{}^2} + \epsilon'_{eff}}{2} - \sin^2 \theta_i} \right|^2}{\left| \epsilon'_{eff} \cos \theta_i + \sqrt{\frac{\sqrt{\epsilon'_{eff}{}^2 + \epsilon''_{eff}{}^2} + \epsilon'_{eff}}{2} - \sin^2 \theta_i} \right|^2}. \quad (100)$$

The total reflectivity from the homogenous media becomes

$$r = \frac{r_v + r_h}{2}, \quad (101)$$

$$k_s = \exp(-h \cos^2 u) \quad (102)$$

The roughness parameter h is calculated with the standard deviation of the roughness height and wavelength,

$$h = 4\sigma^2 \left(\frac{2\pi}{\lambda} \right)^2 \quad (103)$$

Finally, the reflectivity, including the roughness effect is,

$$r_s = r k_s \quad (104)$$

The radiative transfer model connects the BT measured on the microwave sensor with the actual temperature and optical properties of the land surface. The dielectric mixing model links the optical properties (reflectivity of soil) and soil water w via (99) to (104).

3.4 Transmissivity of Canopy, t_c , from the Canopy Water Related Optical Thickness

The soil emission underneath the canopy layer is attenuated by the transmissivity of the canopy, t_c , which is determined by the optical thickness τ and the incident angle θ_i .

$$t_c = \exp(-\tau \cos \theta_i) \quad (105)$$

Theoretically, the physically valid computation of t_c or τ of the canopy might be based on the isotropic effective dielectric constant of vegetation, which is composed of main-phases biomass, vegetation water, and pores in the membranes, similar to the dielectric mixing for the soil medium. In this study, we apply the existing simple linear approximation with parameter b according to Jackson [13].

$$\tau = bw \quad (106)$$

3.5 Anisotropic Brightness Temperature Measured on Microwave Sensor

The effective BT and fractional parameter of the land surface model are anisotropic as shown in Fig. 12. The anisotropic medium is defined in terms of different properties in different directions. In remote-sensing applications, the measured unit pixel originates from a FOV covering a large horizontal area with very shallow measured depth. Upon normalization of this medium, the measurable medium becomes anisotropic. The effective value of the BT, which is the final product from the forward model, is anisotropic. The measurement scale in microwave remote sensing has a shallow penetration depth, i.e., 2 cm, and a wide FOV of 39 km · 47 km for SMAP and 35 km at the center of the FOV for SMOS. Therefore, the normalized vertical and horizontal directions of the observed mixture are anisotropic.

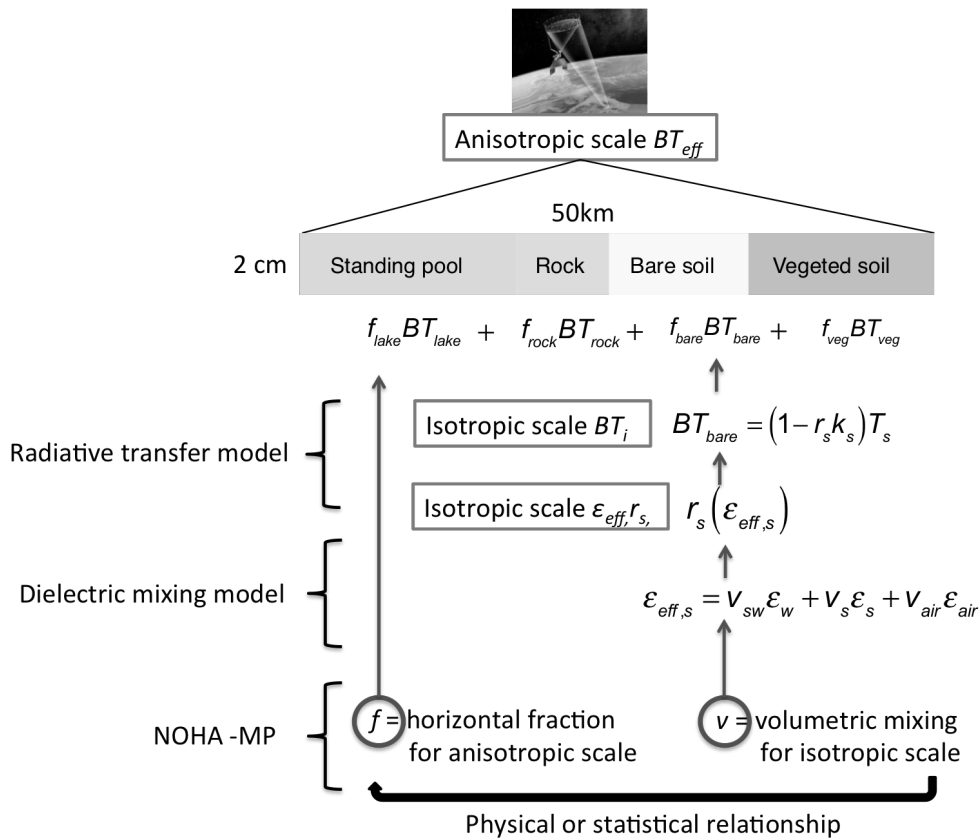


Fig. 13. Anisotropic BT simulation using the advance forward operator in the space-born remote-sensing scale.

Overall, the link between the effective values of electromagnetic properties is related differently to the model properties. The volumetric mixing information of sand, silt, and clay particles and the volume of water molecules are linked to the effective dielectric constant. The fractional information of the soil texture class, vegetation, and precipitated area are linked to the effective BT. As shown in Fig. 12, the fractional water or vegetation are linearly proportional to BT. The volumetric water contents, vegetation density, or the volumetric mixing ratio of clay are linearly proportional to the effective dielectric constant (which is nonlinear for water because of its multiple phases) and nonlinear in relation to the effective BT. In the case study scale I focus on a real-world isotropic case, namely a bare soil surface in Schäfertal.

4. Land Surface Model

4.1 Theoretical Framework

Finally, the addition of physical properties through a land surface model completes our novel forward model. The land surface model facilitates resolution of the ill-posed inverse problem in bare soil remote sensing. In this section, the proposed forward model is utilized for soil texture inversion obtained from remotely sensed BT.

Table 11. Concept of the inversion process using new approaches

Term	Mathematical expression	Description
True state	X_{true}	Real temperature, water, and soil texture on the surface
Observable true state	Y_{true}	Observed BT from the passive microwave remote sensing
Model state	X	Temperature, water, and soil texture in land surface model
Forward model*	f	Radiative model / Dielectric mixing model*
Response model	r	Partial derivative of f
Partitioning factor*	Φ	Model sensitivity in BT scale normalized via r
Partitioned simulation error	$\Phi(Y_{true}-f(X))$	Model error in BT scale
Partitioned model error	$r^{-1}\Phi(Y_{true}-f(X))$	Model error in own physical scale
True state	$X+r^{-1}\Phi(Y_{true}-f(X))$	Model states improved from observed BT which is ideally equivalent to X_{true}

*New approaches

As shown in Table 11, the forward model f and partitioning factor Φ are essential components of the inversion process. These two models developed in this study form a new contribution to the research field of land surface remote sensing. The following parts of this section contain a detailed explanation of the mathematical derivation of the proposed response model.

4.2 Well-Posed Response Model

This section introduces the response model, which integrates the physical parameters from the bare soil model. This approach allows us to estimate multiple soil properties from the single BT value measured remotely over bare soil. The measured radiance is a signal resulting from the effect of multiple model variables: the soil water content W , soil temperature T , and soil texture S ; the canopy water W_c , canopy temperature T_c , and canopy type C and its status (e.g., its leaf area index (LAI) and height). The determination of the soil water and soil temperature not only depends on the soil texture, but also on the status and type of canopy. Therefore, the BT registered on the microwave sensor is the result of the regulation of both soil texture and vegetation. Should we already have accurate soil texture information from underneath the canopy layer, this could be reflected as input in the land surface model to identify the error source in the canopy information of the model. Thus, in this study I focus on developing the bare soil forward model to simulate accurate BT readings before the vegetation appears. Even though the relationship between the model properties and remote-sensing measurement in the case of bare soil is less complicated compared to those with vegetation, bare soil remote sensing is still challenging with one measured variable, BT, and three unknown variables: soil temperature, soil water, and soil texture. Furthermore, I also investigate the response model derived from the forward model in this section.

The general mathematical expression of the forward model for bare soil is (A) in Fig. 14, which is an ill-posed problem involving the estimation of three model variables, T , W , and S , from a single measurement, namely the BT.

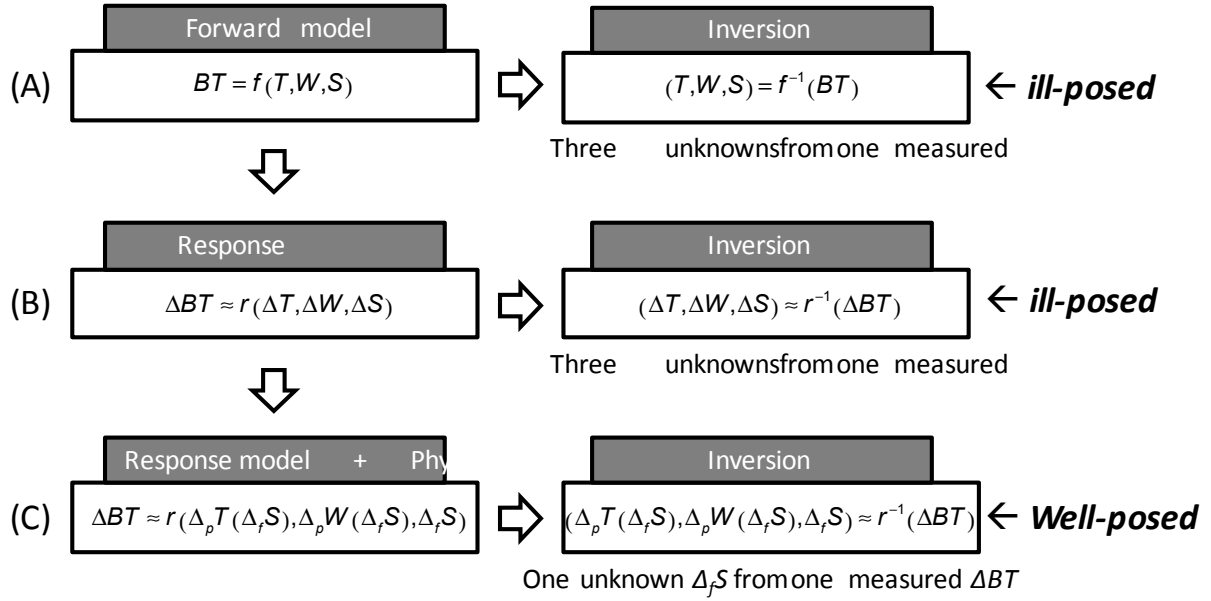


Fig. 14. Derivation of the well-posed solution for bare soil remote sensing (f: forward model, r: response model equivalent to Jacobian operator).

The response model presented in (B) is equivalent to the partial derivative of the forward model, the inversion of which suffers from an ill-posed problem. However, by virtue of the physical relationship among the variations of the model parameters, the inversion process of the response model can be well posed if we apply the model physics. For example, in bare soil remote sensing the difference in the soil temperature ΔT and soil moisture ΔW in the pixels are determined only by the difference in the soil texture ΔS under identical atmospheric forcing and initial conditions. Therefore, the unknowns ΔT and ΔW can be expressed in terms of ΔS as shown in (C) in Fig. 14, concluding that the inverse response function is well posed for estimating one of the unknowns ΔS from the one known variable ΔBT . In other words, the physical relationship of the soil texture ΔS with ΔT and ΔW is the key clue to resolve the ill-posed problem in the estimation of these variables from the remote-sensing measurement.

4.3 Physical Partitioning from Perturbation

Therefore, we need to determine how to apply the model physics to the inversion process (C), i.e., the physical relationship of ΔS to ΔT and ΔW . I address this problem by introducing the concept of the physically based partitioning factor. The partitioning factors for each model parameter are computed based on their physical variations in the normalized space. The sum of these factors always becomes a unit maintaining physical balance among them. Therefore, for the soil texture remote-sensing application, these factors play a role in accurately distributing the observed ΔBT into the estimations of ΔT , ΔW , and ΔS . The physically based partitioning factors are computed by introducing the perturbation strategy using the land surface model, NOAH-MP. In addition, I demonstrate the ability of the physically based partitioning factor to improve soil texture information and accordingly the soil temperature and soil moisture information.

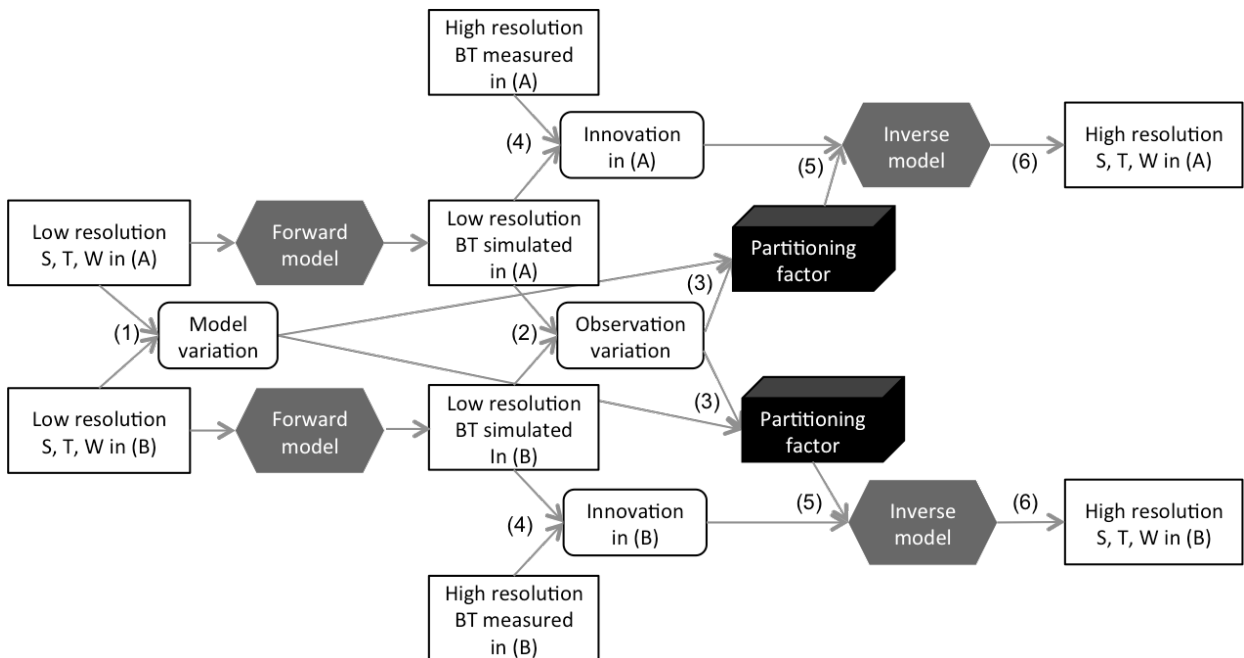


Fig. 15. Inversion strategy using partitioning factors by NOAH-MP perturbation and forward and inverse response model from dielectric mixing and radiative transfer model; S: soil texture, T: soil temperature and W: soil moisture.

4.3.1 Process 1: Model variation & Forward response model

I derive the forward response ((2) in Fig.15) from our forward model. The expression containing the partial derivatives provides an intuitive prospect about how the net variation of BT on the measurements sensor is composed of the variation of the individual model parameters T , W , and S , which is (1) in Fig.15.

$$\underbrace{dBT}_{\text{observable net variation}} = \underbrace{\frac{\partial BT}{\partial T}}_{\text{response model}} \underbrace{dT}_{\text{model variation}} + \underbrace{\frac{\partial BT}{\partial W}}_{\text{response model}} \underbrace{dW}_{\text{model variation}} + \underbrace{\frac{\partial BT}{\partial S}}_{\text{response model}} \underbrace{dS}_{\text{model variation}} \quad (107)$$

$$\begin{aligned} \text{Response model} & \left\{ \begin{array}{l} \text{Dielectric mixing model} \\ \text{Radiative model} \end{array} \right. \\ \text{Model variation} & \left\{ \text{NOAH – MP model} \right. \end{aligned}$$

Scaling of the model variation (right side of (107)) is determined by the equivalence of their total contributions to the observed correction (left side of (107)). If one of the contributing components is missing from (107) and it was a significant source among the contributions on the right side of (107), the inversion process (computation from left to right in the equation) will cause a bias error in the estimation of the model parameters.

4.3.2 Process 2: Partitioning factor

The partitioning factor ((3) in Fig.15) calculated by the forward response model, plays a critical role to divide the net measured BT into multiple model parameters. The model variations or the model sensitivity information can be translated into their variation in the observation space via the forward response model of the conjugation with the partial derivative of radiative transfer (98) and the dielectric-mixing model (84) for bare soil. The response model

derived from the forward response model enables us to compute the partial contribution of the land surface variables in NOAH-MP and measurable as the BT on the microwave sensor. The partial contribution of the variables of the i -th model in BT space can be expressed as

$$dBT_i = \frac{\partial BT}{\partial x_i} dx_i . \quad (108)$$

Then, the partitioning factor normalized by the total contribution of the variables of the entire model becomes

$$\phi_i = \frac{dBT_i}{\sum_{i=1}^n dBT_i} , \quad (109)$$

where n is the number of variables in the model.

For example, by model perturbation, each grid cell contains the perturbations of the soil temperature

$$dBT_T = \frac{\partial BT}{\partial T} dT \quad (110)$$

soil water

$$dBT_W = \frac{\partial BT}{\partial W} dW \quad (111)$$

and soil texture,

$$dBT_S = \frac{\partial BT}{\partial S} dS . \quad (112)$$

Based on the model information, which is translated into the BT space via the response model, I compute the physical-based partitioning factors for the remotely measured BT related to the contribution of the soil temperature

$$\phi_T = \frac{dBT_T}{dBT_T + dBT_W + dBT_S} , \quad (113)$$

soil water

$$\phi_w = \frac{dBT_w}{dBT_T + dBT_w + dBT_s} \quad (114)$$

and soil texture

$$\phi_s = \frac{dBT_s}{dBT_T + dBT_w + dBT_s} \quad (115)$$

The physically based partitioning factors allow us to perform realistic model improvement over multiple variables and parameters by maintaining the physical balance among them based on the remote-sensing measurements.

If the contribution factors are not computed based on the model physics or are ignored for any contribution of model variables, the model update from remote-sensing measurements will be problematic, thereby causing unrealistic values in model updates or improvements.

4.3.3 Process 3: Innovation

Innovation ((4) in Fig.15) is the difference between the model world with limited knowledge of the true states and the real world measured by remote sensing. In this study, innovation is defined as the difference between observation from remote sensing and simulation from NOAH-MP via the forward model.

$$\Delta BT = BT_{obs} - f(T, W, S) \quad (116)$$

Innovation can be obtained from our limited knowledge of the soil texture map as low-resolution soil texture input in NOAH-MP.

4.3.4 Process 4: Partitioned innovation, Inversed response & Model improvement

The computed innovation between the measured signal and the simulated signal can be subdivided into dBT_T , dBT_W , and dBT_S by the partitioning factors. If the values are simply retrieved without using the model physics to interpret them, the signal variation only originates from the single model properties such as in the microwave soil moisture retrieval algorithm. However, by knowing the physical relationship among the parameters, we can interpret all model contributions in the BT space simultaneously by substituting the partitioning factors calculated from (113), (114), and (115) which are referred to as partitioned innovation ((5) in Fig. 15) as follows.

$$\Delta BT_T = \phi_T \Delta BT \quad (117)$$

$$\Delta BT_W = \phi_W \Delta BT \quad (118)$$

$$\Delta BT_S = \phi_S \Delta BT \quad (119)$$

Then we can translate the partial contribution of remotely sensed BT into its own physical units using the inversed response function.

$$\Delta T = \left(\frac{\partial BT}{\partial T} \right)^{-1} \Delta BT_T \quad (120)$$

$$\Delta W = \left(\frac{\partial BT}{\partial W} \right)^{-1} \Delta BT_W \quad (121)$$

$$\Delta S = \left(\frac{\partial BT}{\partial S} \right)^{-1} \Delta BT_S \quad (122)$$

These are the model improvements from the measured BT.

4.3.5 Process 5: Error consideration

The remote-sensing measurement can be more realistically interpreted by identifying the error ((8) in Fig.15). If the observation error is relatively high compared to the background knowledge or the model simulation, we have to avoid updating the model from the observation. In this case, the weighting factor of the difference from the observation simply becomes 0. However, if the remote-sensing observation is very reliable, this factor approaches 1. For example, this weighting factor for the observation error is mathematically derived in the Ensemble Kalman filter [6].

$$\Delta T = \left(\frac{\partial BT}{\partial T} \right)^{-1} \Delta BT_T \eta_{BT} \quad (123)$$

$$\Delta W = \left(\frac{\partial BT}{\partial W} \right)^{-1} \Delta BT_W \eta_{BT} \quad (124)$$

$$\Delta S = \left(\frac{\partial BT}{\partial S} \right)^{-1} \Delta BT_S \eta_{BT} \quad (125)$$

Note that, unlike the various partitioning factors of BT for each of the model variables, the error-weighting factor η_{BT} is identical for all the variables as the measured BT is the single source of errors.

4.3.6 Process 6: Improved model states

By adding model improvements to the original control model states, we can compute the new temperature, T_{new} , water, W_{new} , and volumetric soil mixing ratio S_{new} as shown in

$$T_{new} = T + \Delta T, \quad (126)$$

$$W_{new} = W + \Delta W, \quad (127)$$

and

$$S_{new} = S + \Delta S. \quad (128)$$

5. Results

5.1 Limited Knowledge about Soil Texture Information

BT simulations were performed by using the bare soil properties of the Schäfertal sub-catchment area. The general soil texture in this region is characterized as Luvisols (upper part) and Cambisols (lower part) as shown in Fig.10(a) [98]. According to the USDA (U.S. Department of Agricultural) soil texture classification, the soil texture of the upper part is loam, whereas the lower part consists of clay loam (see Fig. 10(b)). The dominant soil mineral in the Schäfertal sub-catchment area is silt, which forms approximately 60 % of the volumetric mixing ratio [99]. On the other hand, the volume matrix ratio for silt measured in a small hill slope area of the Schäfertal gauging station, as found in [100], was 69.48 % for silt and the sand and clay mixing ratio was 13.78 % and 17.22 %, respectively. This small-scale study area corresponds to the upper part of the Schäfertal catchment area. Regardless of the large-scale soil texture map of the Schäfertal catchment area or the more detailed soil texture measurements in parts of the Schäfertal catchment area, the high-resolution soil texture information is required to understand the hydrological cycle and energy balance over this region. In this study, I improved our limited knowledge of the soil texture information over the Schäfertal catchment area by extracting information from the PLMR measurements

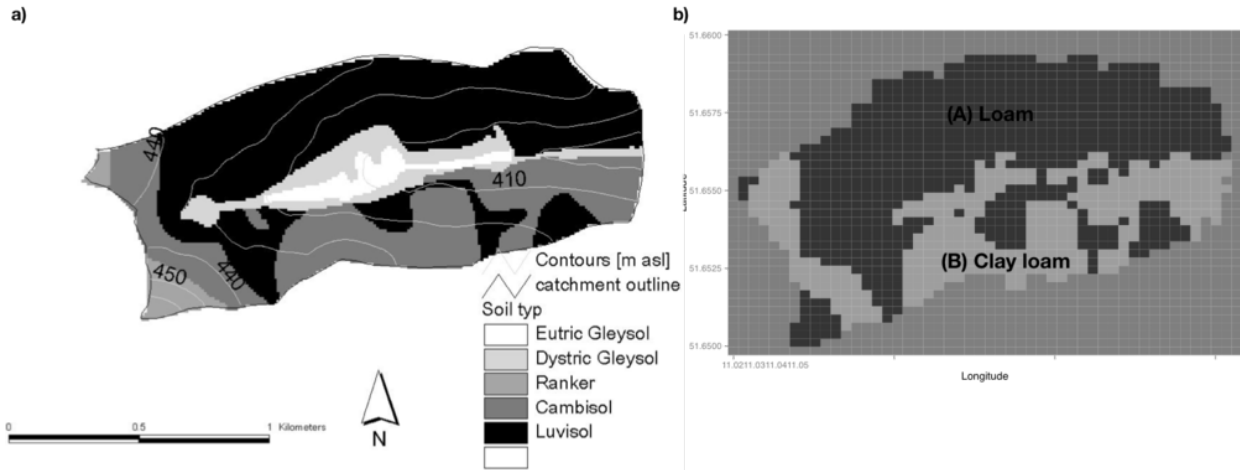


Fig. 16. Soil texture map for (a) Schäfertal sub-catchment area [98] and (b) digitized into two soil textures: (A) loam for Luvisol and (B) clay loam for Cambisol. The regional map for this catchment area is provided in Fig.4.

5.2 Homogeneous atmospheric weather forcing

As shown in Fig. 18, the microwave BT measurements from PLMR were obtained at 10:30 am on May 27, 2008 for which the DOY (days of year) is 148. The atmospheric weather forcing related to this remote-sensing moment was obtained from the re-analysis of the GLDAS (Global Land Data Assimilation System) weather data [101]. The size of the Schäfertal sub-catchment area is so small (1.44 km^2 [9]) that the weather conditions could reasonably be assumed as homogeneous. The main difference in an area of this size is, therefore, only the soil texture distribution as shown in Fig. 16.

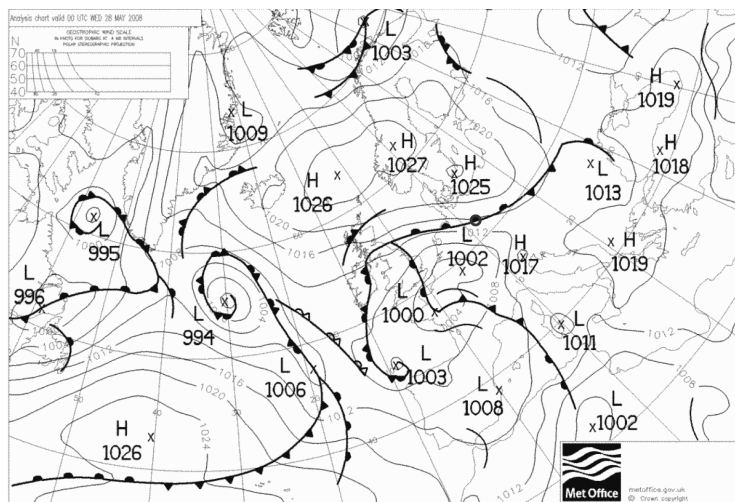
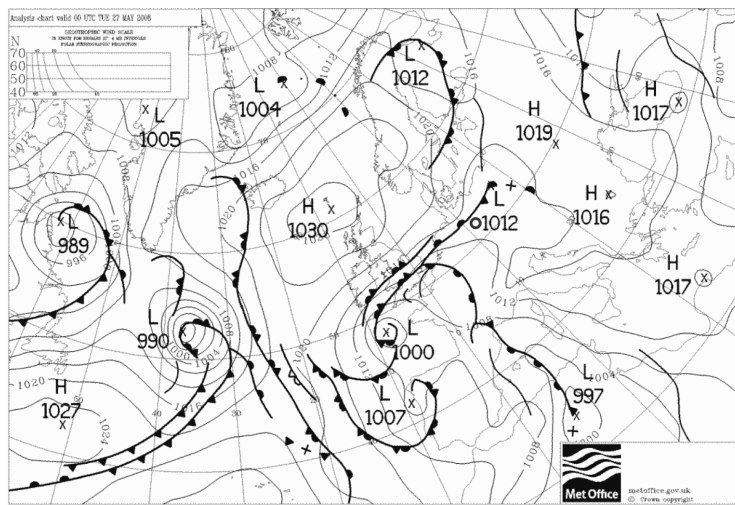
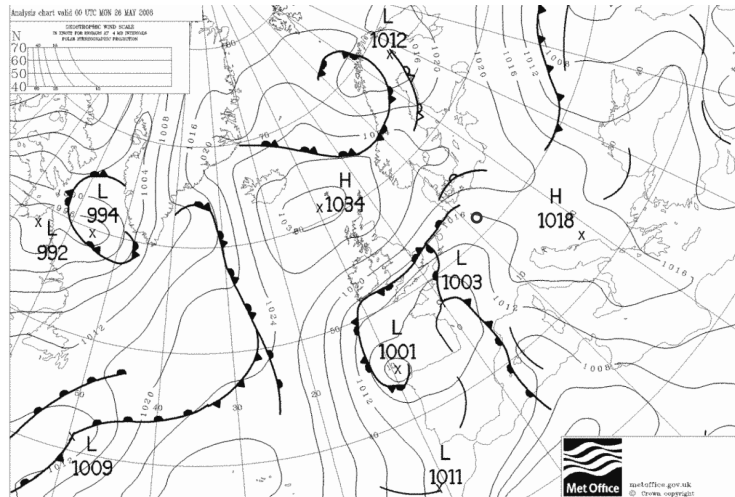


Fig. 17. Synoptic weather map from Met Office: top (May 26, 2008), middle (May 27, 2008), which is the date of PLMR measurement, and bottom (May 28, 2008). The black dot indicates the location of the Schäfertal catchment area (51°39'19.61" N, 11°02'24.78"E).

On May 26, 2008 (147 DOY), the warm front is far away from the Schäfertal catchment area as shown in Fig. 17. On May 27, 2008 (148 DOY) the warm front is approaching the red dot indicating the Schäfertal catchment area. On the next day, (May 28, 2008; 149 DOY), the warm front caused the precipitation of rain over the catchment area. Fig. 18 shows the same weather pattern in the NOAH-MP simulation with GLDAS weather forcing. The prediction of soil moisture based on the different soil textures (A) and (B) shows a distinct temporal pattern in soil moisture prediction (Fig. 18(b)) as opposed to the soil temperature (Fig. 18(c)). For instance, the soil water content of the surface layer of the clay loam (B) was systematically higher than that of the loam (A). On the other hand, the soil temperature differed between the loam (A) and clay loam (B), although this difference was smaller than the difference in the soil water. This experiment demonstrates that the effect of soil texture on the soil water content is significant.

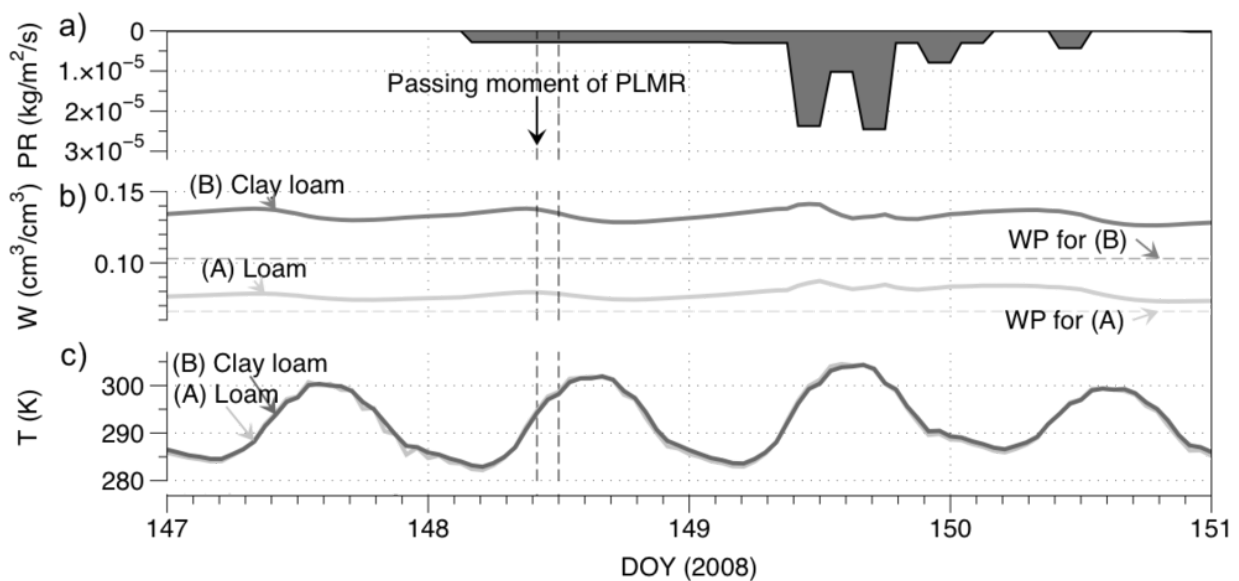


Fig. 18. Temporal simulation of soil moisture (b) and soil temperature (c) with the identical forcing of precipitation event (a) with different soil texture. (A) and (B) are loam and clay loam, respectively, as indicated in Fig. 16.

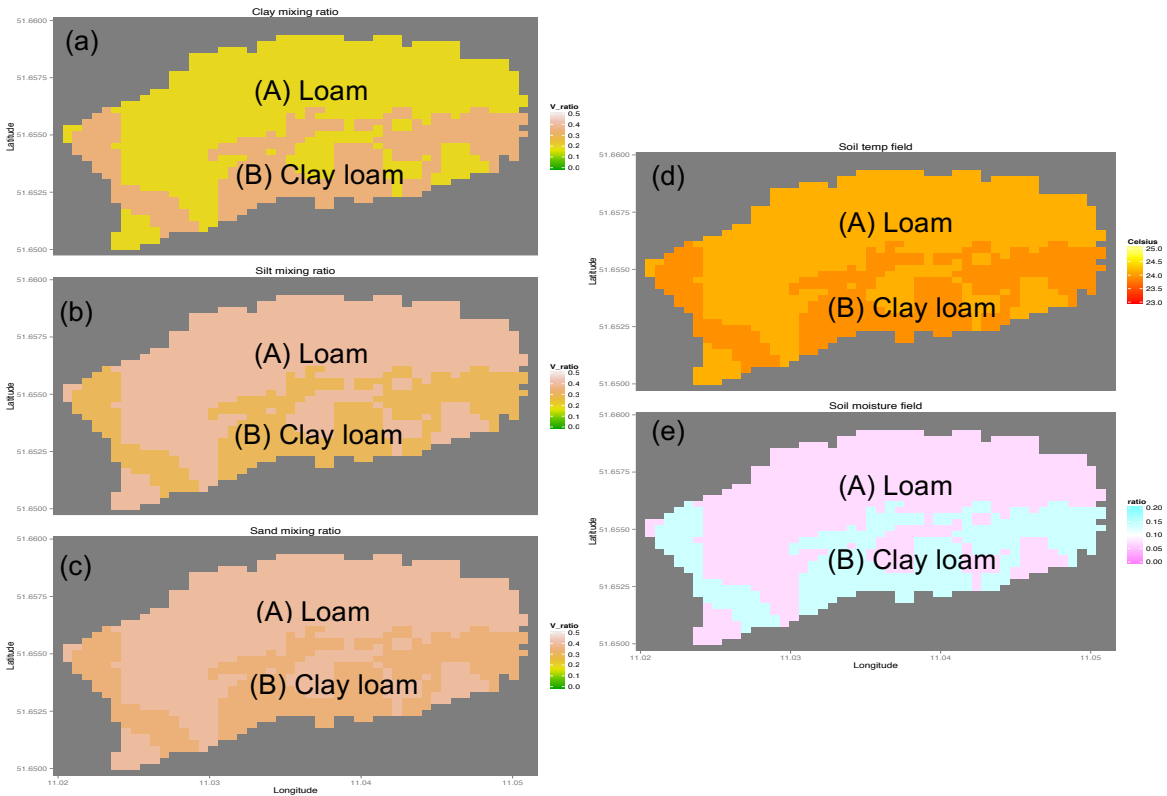


Fig. 19. NOAH-MP 2D simulation at the passing moment of PLMR with the atmospheric forcing form GLADS re-analysis from January to December, 2008: (a) clay, (b) silt, c) sand mixing ratios, (d) soil temperature, and (e) soil moisture for (A) loam and (B) clay loam.

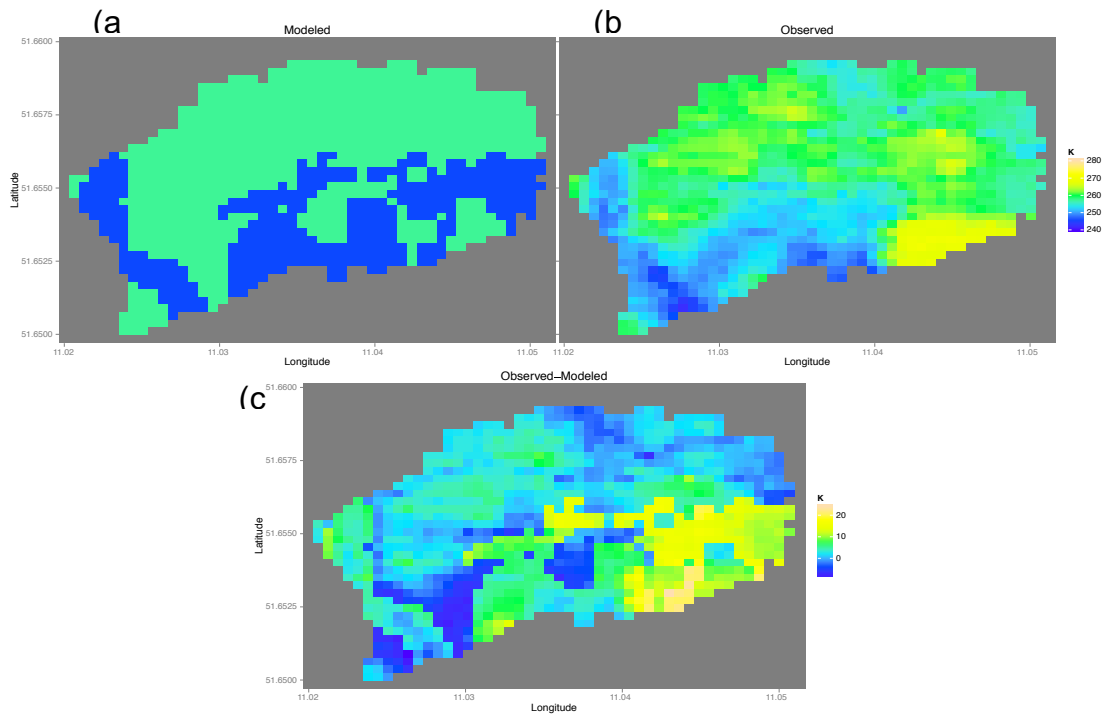


Fig. 20. Computation of model error using microwave measurements: (a) forward model simulation (NOAH-MP), (b) L-band microwave radiometry measurement (PLMF), and (c) innovation from the difference between observation and model simulation.

Fig. 19 presents the 2D simulations of the land surface model properties from NOAH-MP according to the soil texture, loam (A), and clay loam (B). In reality, the soil texture, i.e., the mixing ratio of clay, silt, and sand, is spatially continuous. Therefore, the tabulated soil input parameters, such as the wilting point and porosity of the soil medium, saturation soil potential, soil diffusivity, and soil thermal conductivity/diffusivity coefficient, parameterized according to 12 soil texture classes are inherently the huge error sources in the prediction of the land surface model, including the NOAH-MP model. Therefore, a highly resolved soil texture from microwave BT measurements, rather than a coarse classification, would result in a more realistic spatial distribution pattern of the soil temperature and soil moisture.

5.3 High Resolution Innovation from Observation

Firstly, based on the simplified soil texture map reflecting our limited knowledge about the Schäfertal catchment area, the low-resolution BT is simulated as shown in Fig. 20(a). Using the L-band microwave remote-sensing measurements (Fig. 20(b)) we can calculate the model error as the BT (Fig. 20(c)). The inversion process presented in this study was expected to lead to a reduction of the model error. Therefore, the innovation is a potential model improvement appearing in the observation space, such as the remote-sensing BT measurements.

5.4 Computation of Partitioning Factor from Model

Based on the soil texture simplified as the two types shown in Fig. 20, the soil temperature and the soil moisture were simulated for the moment when the PLMR measurements were obtained (dotted lines in Fig. 18). The result showed that the different soil textures are associated with different soil temperature and soil moisture regimes. This sensitivity study enabled us to derive the forward response model from the forward model. Using the forward response model, I was able to compute the partitioning factor using (113), (114), and (115), which served a critical role in the solution of the ill-posed inverse problem.

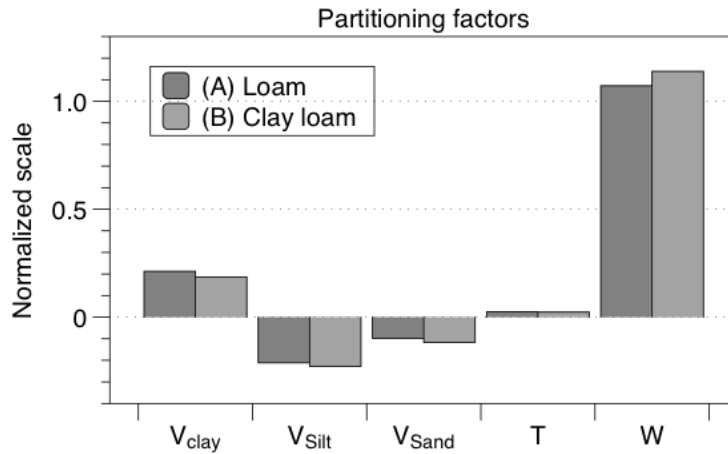


Fig. 21. Computed partitioning factors for soil mixing ratios and model variables T (soil temperature) and W (soil water) for (A) loam and (B) clay loam.

The set of partitioning factors presented in Fig. 21 are computed from: (1) perturbation of the temperature and soil moisture by the soil texture difference between (A) and (B), (2) translating the difference between (A) and (B) of model properties into BT space by multiplying the forward response model (differentiate forward model) as shown in (110) – (112) and, finally, (3) normalization of each component based on their total. The partitioning factor contains the information about how to subdivide the remotely sensed measurement into the

multiple land surface model variables in the same BT scale. The novel forward model composed of the NOAH-MP, dielectric mixing, and radiative transfer models translates the degree of soil temperature, soil water, and soil mixing ratios into the measurable BT and its response model allows us to compute their partitioning factors in the BT space. For instance, Fig. 21 shows that the BT measured by the PLMR over the loam area (A) on May 28, 2008 is almost partitioned into 110 % for the soil water, and 21 %, -21 %, and -10 % for the volumetric mixing ratio of clay, silt, and loam, respectively.

5.5 Improvement for Multiple Model Variables

The spatial variation of the model error computed by obtaining the difference between the model and the remotely sensed measurement in Fig. 20(c) provides us with the unique magnitude of the total BT contribution from the remote-sensing measurement for each individual pixel. Owing to the partitioning factors computed for loam and clay loam as in Fig. 21, the improvements for the multiple model parameters on the BT scale (Fig. 22(a).1 to (e).1)) can be translated into their own physical unit (Fig. 22(a).2 to (e).2)) via the inverse response model. A comparison of the model simulations based on the two types of soil texture information (Fig. 23(a).1 – (e).1), indicated that the resolution of the new model predictions for the multiple model states was improved (Fig. 23(a).2 – (e).2).

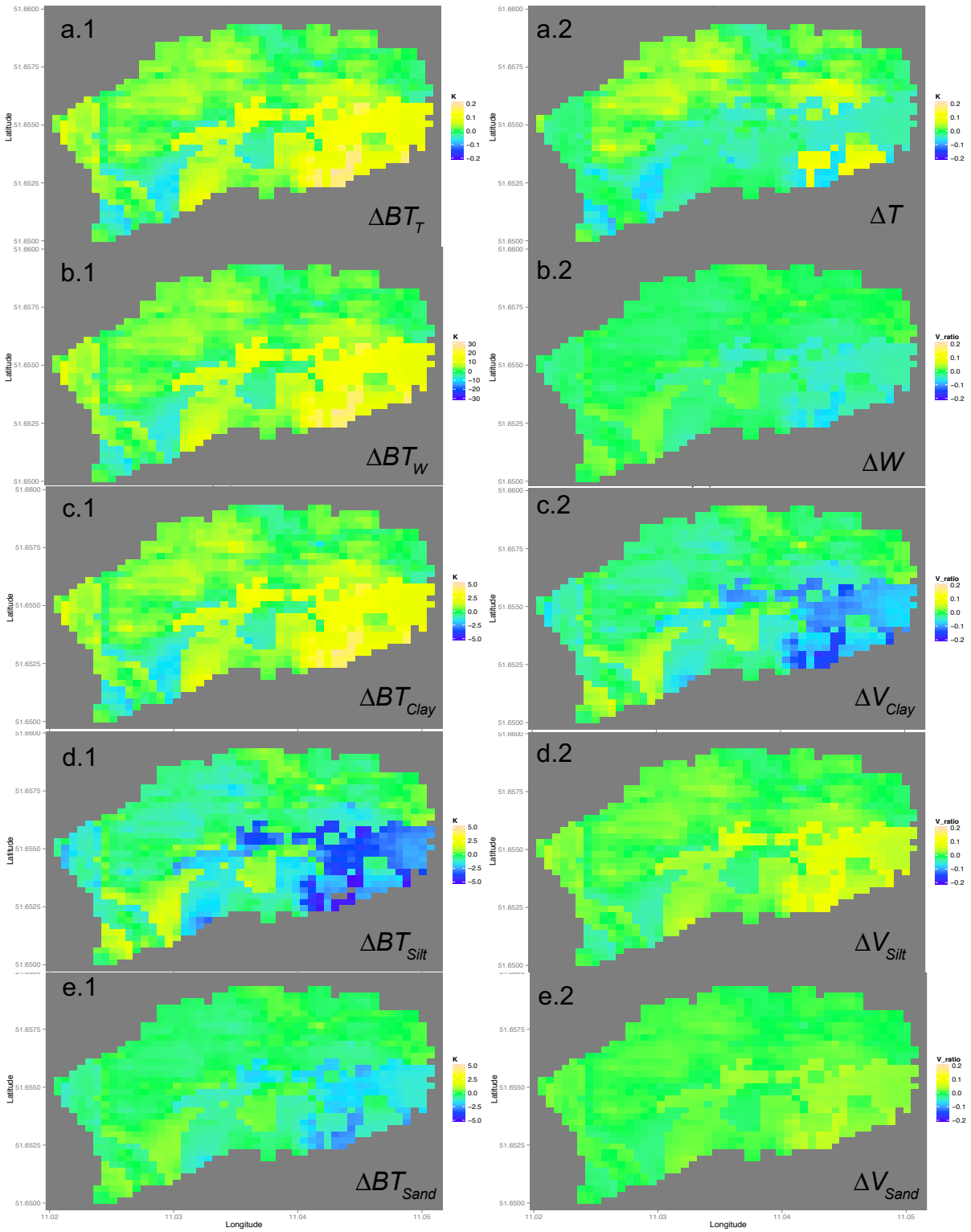


Fig. 22. BT contribution plot of the measurement difference separated into multiple model parameters (soil temperature, surface temperature, soil water (first row), and soil texture, clay, silt, and sand (second row)) computed by (117) – (122).

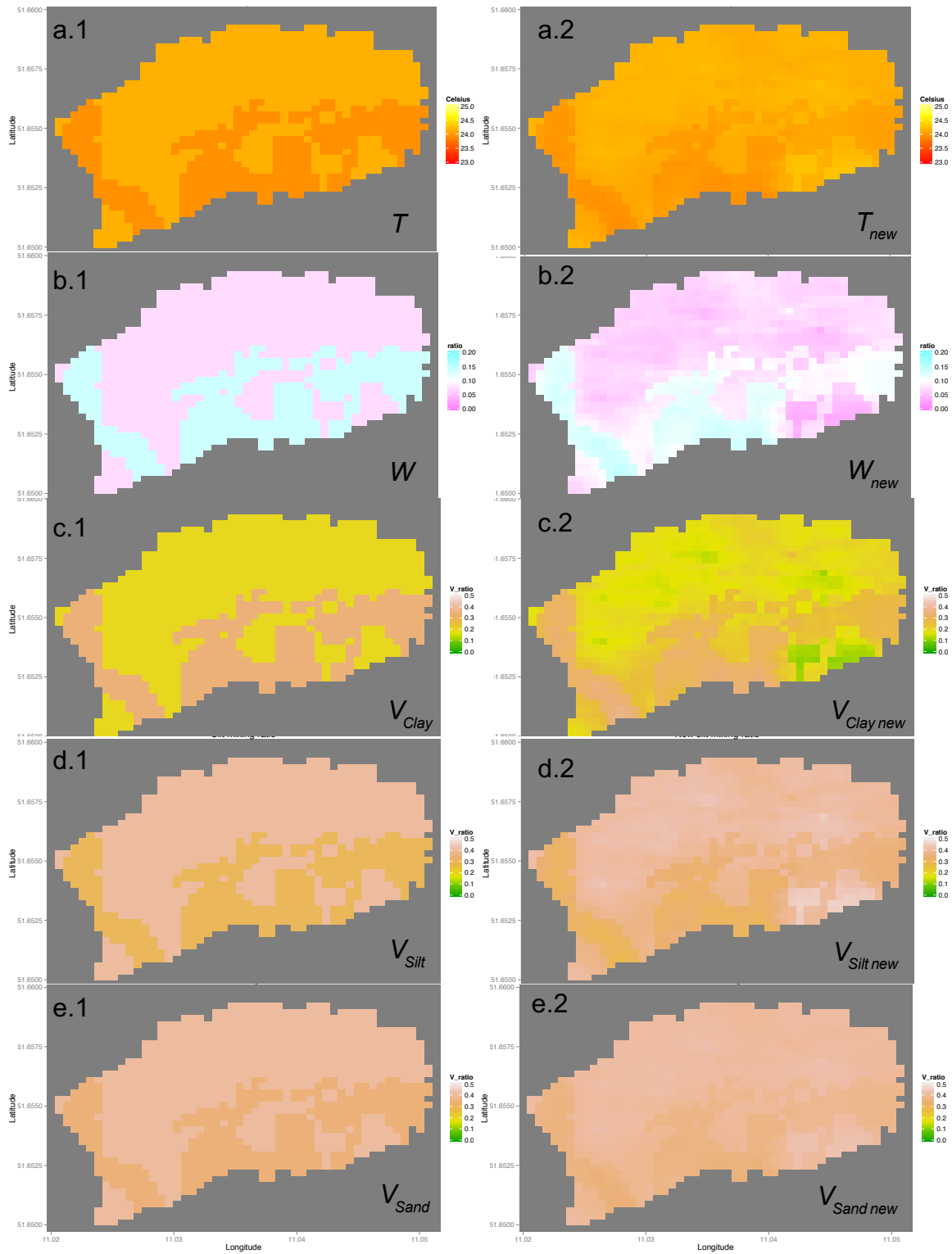


Fig. 23. Improved model states after reflecting remote-sensing measurements in the soil temperature, the surface temperature, the soil water (first row), and the soil texture, clay, silt, and sand (second row) computed by (126) – (128).

In the new model prediction with the improved soil texture input, two distinct bar-distribution patterns of the model states in the control run were changed into continuous Gaussian-like curves with a greater standard deviation than the control run; i.e., ‘before update’ for which the standard deviation is 0 due to the bar-type distribution for each soil texture (A) and (B). The change in the distribution pattern from a single value for all pixels to a unique magnitude for each pixel implies that the resolution of the model prediction has been refined by the remote-sensing measurements. Now the peaks of the distribution patterns can be compared to the bar distributions of the control run in Fig. 24. If the model predictions for the soil temperature, soil water, and volumetric soil-mixing ratio from the control run are systematically overestimated or underestimated compared to the average of their new estimation (translated from the remote-sensing measurements), the remote-sensing observation can also be utilized to reduce these model bias errors.

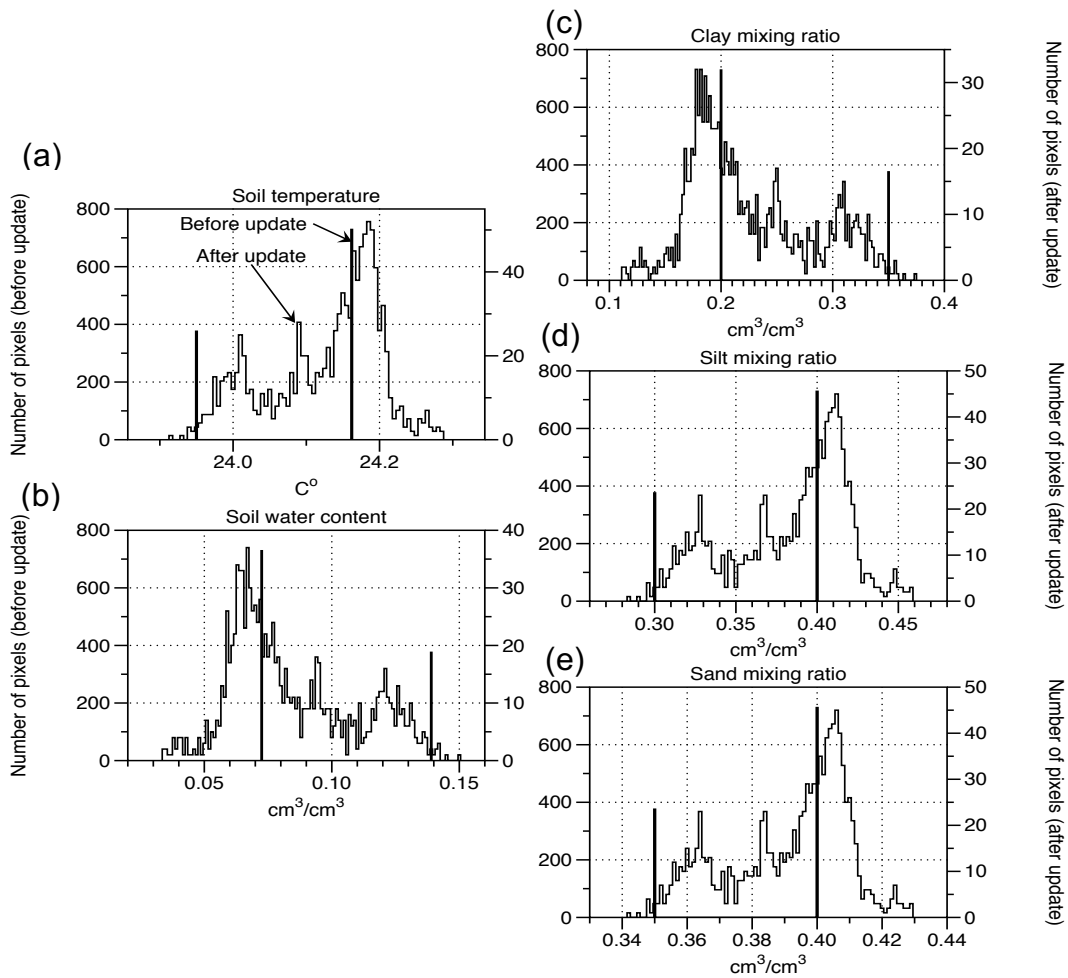


Fig. 24. Comparison between the average and standard deviation of the simulation before update (two types of soil texture input) and the simulation after update (spatially refined input of soil texture and other relevant soil parameters).

The NOAH-MP land surface model is capable of simulating the soil temperature and soil moisture based on only 12 types of soil textures by USDA soil classification (Fig. 25(a)). Using the proposed forward model, the microwave remote-sensing measurements would not only lead to improved soil texture information, (Fig. 25(a)) but would also improve the resolution of other model parameters in the NOAH-MP simulation (Fig. 25(b) and (c)).

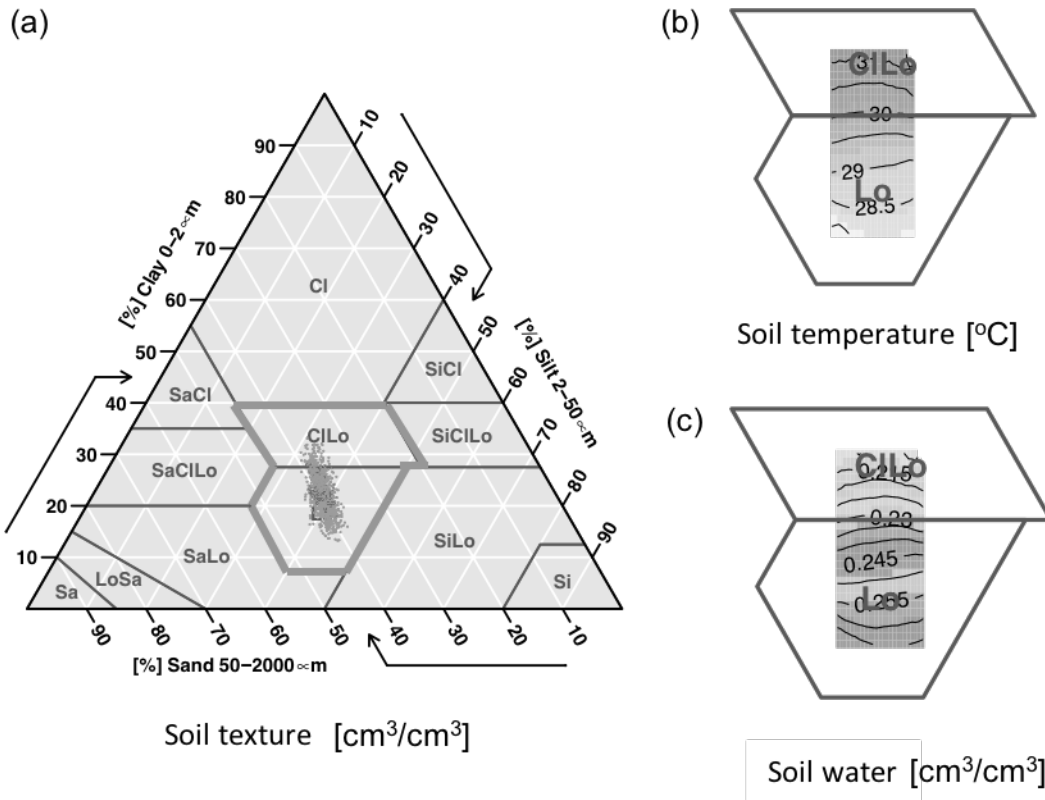


Fig. 25. Refined sand, silt, and clay mixing ratio information over the typical USDA soil texture classification and (a) their impacts on the soil temperature, (b) soil moisture, and (c) regimes in the simulation of NOAH-MP.

5.6 Validation of BT Simulation

The *in situ* soil moisture and soil temperature measurements for the Schäfertal catchment area are unfortunately not available for the targeted forecasting time step, which was on May 28, 2008, i.e., on day 148 of the year (DOY). This date falls in a drying period when the surface temperature and soil moisture content largely depend on the type of the soil texture. These *in situ* measurements are critical for retrieval of the soil texture. However, in this work, instead of the *in situ* measurements, the remote-sensing BT measurements were implemented with the forward and NOAH-MP models to derive the soil texture. In addition, rather than using the *in situ* measurements, which were unavailable, I used the microwave BT measurements to validate the improvement in the NOAH-MP prediction by the soil texture correction.

The microwave BT is the impact of the measured phenomenon of the soil texture on the land surface model properties. Using this inversion approach we are able to retrieve this cause as the refined soil texture input. Only by modifying the soil texture input based on realistic conditions, can we truly predict the soil temperature and soil moisture in the NOAH-MP land surface model. This prediction originates from the NOAH-MP simulation, and not from the inversion of the measured BT. Simulation of the BT from the new prediction of the surface temperature and soil moisture with NOAH-MP enables us to compare these predicted values with the measured BT values to determine whether the new prediction effectively changes toward the control model run or the remotely sensed measurements. For instance, in our Schäfertal catchment case study, the use of the novel forward model and NOAH-MP land surface model allowed us to obtain high-resolution soil texture information from the microwave remote-sensing measurements recorded on May 28, 2008, which were then used to correct the soil texture and hydrological parameters accordingly for Jan. 1, 2008. Based on the same weather forcing technique and the same initial values of the soil temperature and moisture for Jan. 1, 2008, I ran

more than 1000 cases for each pixel with unique soil texture information extracted from the microwave BT obtained on May 28, 2008.

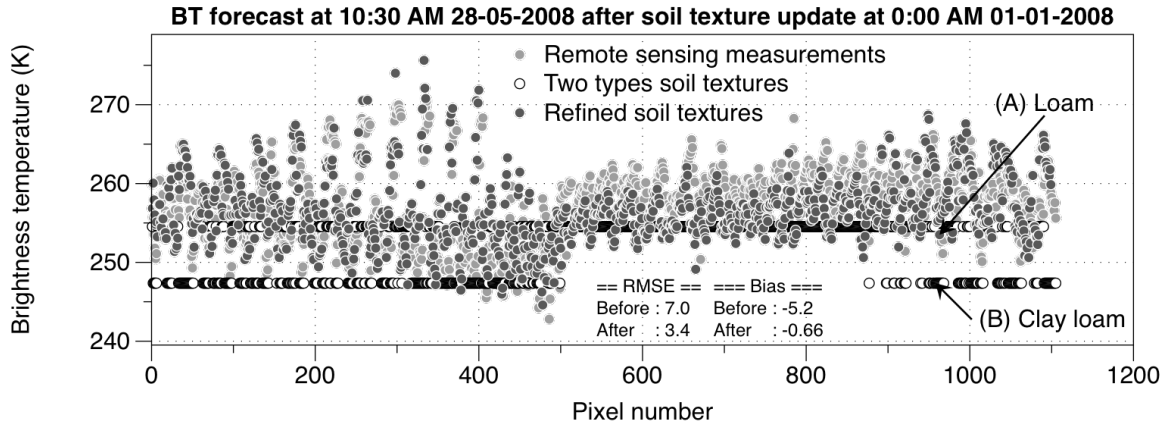


Fig. 26. Predicted BT (red) based on the refined soil texture ranging between the simulated BT from the control run and the BT measured by the PLMR.

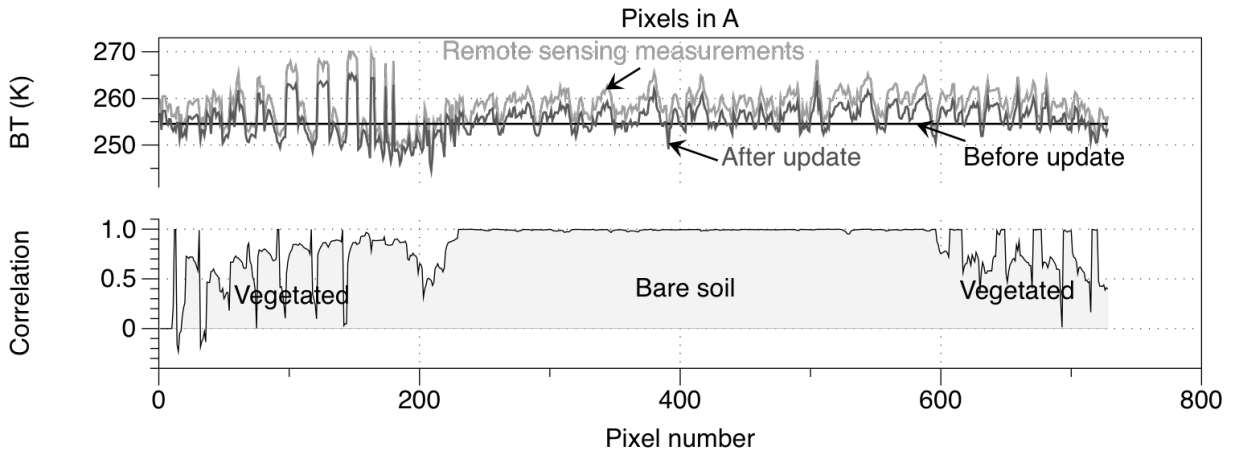


Fig. 27. Correlation analysis resulting from comparison of the bare soil forward model and observed data for surface classification types.

Considering only the pixels classified as (A) loam, I compared the BT simulation from the model run without the soil texture refinement (white dots) and after the soil texture refinement (dark grey dots) against the remotely sensed BT (light grey dots) as shown in Fig. 26. The

abovementioned period of five months was modeled by using the soil texture refinement and this led to an improved prediction of the BT measurements compared to the prediction obtained by running the model based on the two types of soil texture (A) and (B). The improved prediction showed a 50 % reduction in the RMSE score and a significant improvement in the BIAS correction from -5.2 to -0.66.

Furthermore, when I performed a correlation analysis spatially sampled with a limited number of pixels (in this study 10 pixels) (Fig. 27(a)), there is a clear distinction between regions with a very high correlation and those with a low and fluctuating correlation in terms of BT measurements as shown in Fig. 27(b). Because the forward model developed in this study only considers the error effects of the bare soil surface type on the sensor, the BT measurements recorded over the vegetation and BT simulation using the bare soil forward model produced a low and unstable correlation score. This pattern provided by the BT simulation via the forward model for bare soil can be utilized to identify whether a pixel resulting from BT measurements represents vegetation or bare soil. This explanation is also supported by the fact that regions covered in vegetation typically result in brighter BT measurements than bare soil due to the emissivity of the vegetation. Additionally, these brighter BT pixels, which are assumed to be from a vegetated region, also display uncorrelated patterns against BT measurements. This indicates that an approach such as this to perform surface type classification would require a primary forward model designed for one specific type of surface to allow the targeted type to be distinguished in the remote-sensing measurements over regions with mixed surface types.

5.7 Improvement in Heat and Water Fluxes of NOAH-MP

Because the dielectric constant of water in the microwave band is significantly higher than for land surface covers, microwave is the most effective channel for tracking water movement on the land surface. For example, the water flux from the surface to the subsurface (wetting period) and from the surface to the atmosphere (drying period) has different patterns in BT variation that are similar to the different contribution curves in the evapotranspiration and infiltration in Fig. 14(f). Furthermore, the microwave BT measurements as a proxy of water and heat fluxes allow us to realistically calibrate the flux of both the sensible heat and latent heat. In addition, the forward model, composed of the novel dielectric-mixing and radiative transfer models, represents the response between the model properties and the L-band brightness. In Section F, it was demonstrated that the difference between the predicted BT based on the refined soil texture and the measured BT becomes significantly smaller than the BT simulation of the control run when comparing the RMSE and BIAS shown in Fig. 26. The refined soil moisture content of the predicted BT may also facilitate the computation of the turbulence fluxes of the latent heat and sensible heat. However, the refinement in these fluxes would need to be validated by *in situ* measurements, such as eddy covariance flux measurements, in future studies. The focus of this study was on the analysis of the difference between the fluxes that were originally simulated and the predicted fluxes based on new soil texture input to improve our understanding of the role of soil texture in the surface energy balance.

To determine whether the flux simulation is supposed to become increasingly or decreasingly realistic as a result of soil texture improvement, the model variables in Fig. 28(b) and (c) and their temporal variation per hour (d) and (e) in a time series were simulated as a control run (NOAH-MP run based on two types of soil texture). The proposed forward model enables us to simulate the temporal variability of different land surface properties in the BT domain.

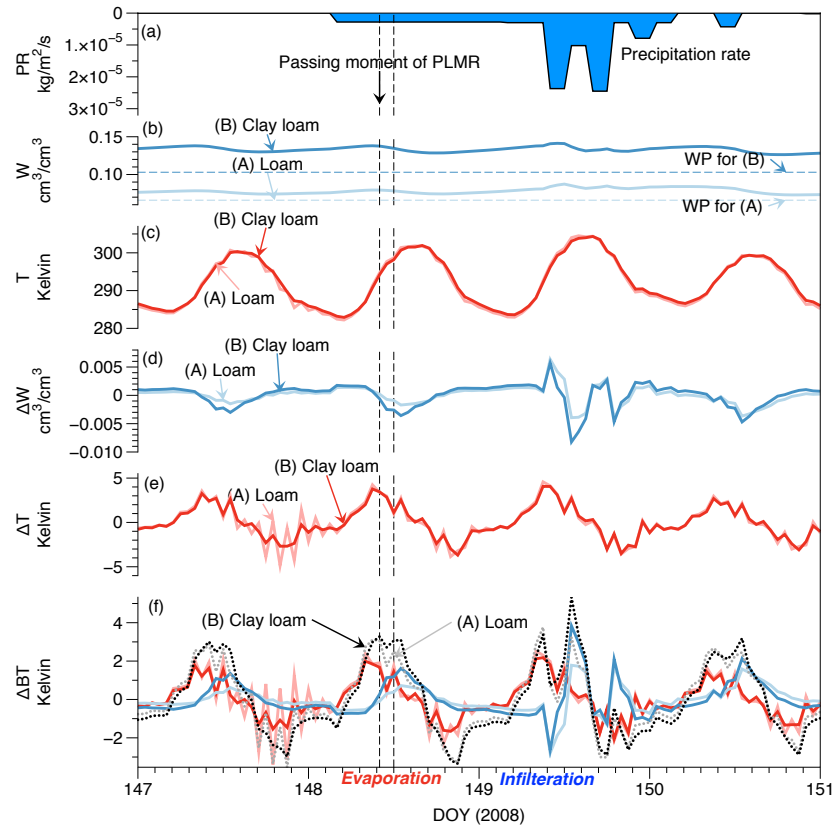


Fig. 28. Temporal response analysis of microwave BT as a proxy of water and heat fluxes in NOAH-MP.

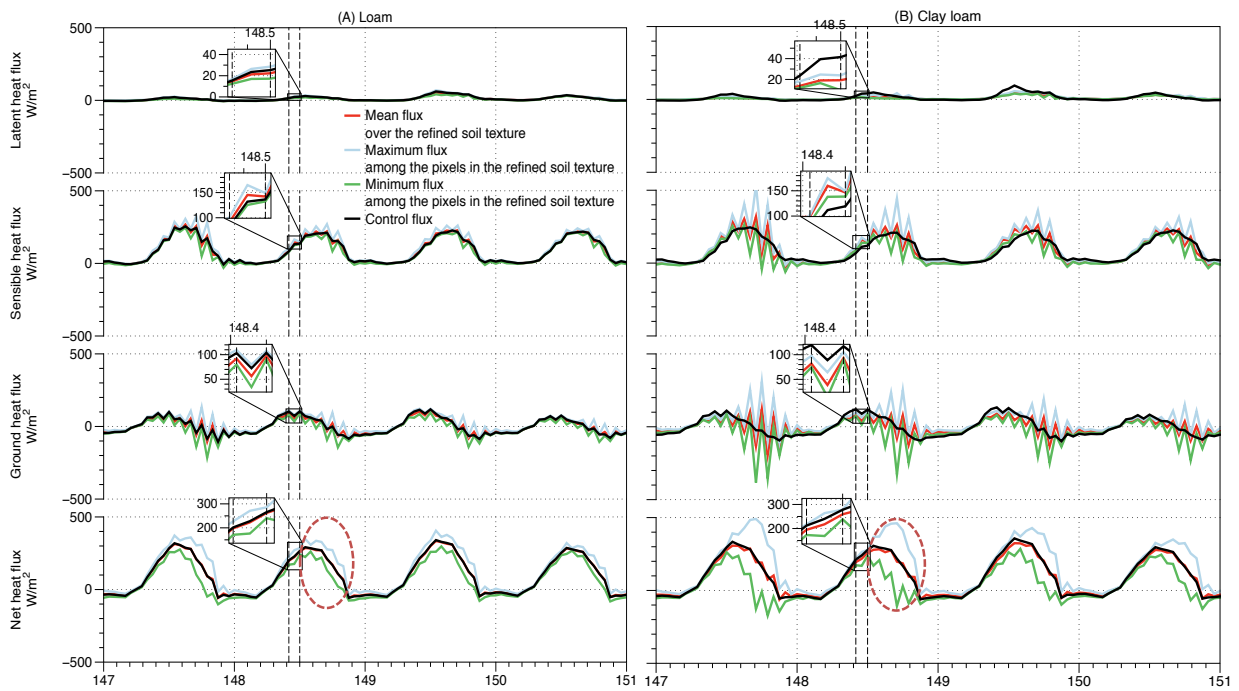


Fig. 29. Flux change in NOAH-MP by the refined soil texture input.

The soil texture refinement based on microwave remote sensing also affects the flux variables in NOAH-MP. The new model run based on the improved soil texture with more than 400 sets of clay, silt, and sand-mixing ratios over the pixels originally classified as representing (A) loam and (B) clay loam, shows a slightly lower net heat flux rate than the control run. On the other hand, owing to the highly resolved soil texture input, the NOAH-MP flux simulation for individual pixels varied in the range with maximum (light blue) and minimum values (light green) as shown in Fig. 29. The significant difference between the minima and maxima of the net heat fluxes was found to occur during the cooling process indicated with red dotted circles (decreasing net radiation in afternoon), especially for the (B) clay loam.

6. Summary and overview

Lately, the “physically based model” ([17, 19, 102]) as radiative transfer model in the study of soil moisture retrieval from passive microwave measurements has been actively studied, a direction that fits into the data assimilation scheme [103]. Rather than focusing on the physical principles of the radiative transfer model, this study focuses on the physical principles of the dielectric mixing model and the physics of the NOAH-MP land surface model introduced in the partitioning factor.

The effective dielectric constant in the forward model is the fundamental parameter required in the accurate quantification of land-surface properties such as water and mineral soil particles. The physically correct averaging method for the effective dielectric constant is the arithmetic mean because it does not violate the superposition rule of polarizability. Considering the soil water phase as consisting of free and bound water and the bulk behavior to include a damping factor, the effective dielectric constant of bare soil properties predicts a complex nonlinear behavior over various soil textures with the lowest RMSE score compared to other semi-empirical models such as those of Wang & Shmugge [10], Dobson *et al.* [6] and the most recent and most prevalent model, that of Mironov *et al.* [7], and calibration approach, e.g., that of Hallikainen *et al.* [52]. An improvement by the new microwave dielectric mixing model would be anticipated in monitoring the surface runoff to minimize damage caused by flooding and flood-related landslides. Moreover, it would be possible to apply the proposed algorithm directly to existing soil moisture estimation algorithms of TDR/GPR devices or to the baseline dielectric mixing model for SMOS and SMAP.

The combination of the physically based dielectric mixing model with the radiative transfer model, and the proposed partitioning factor computed from NOAH-MP model perturbation enables us to evaluate and minimize the model error compared to the remote-sensing

measurements. For example, in the case study of the Schäfertal catchment area, it is discovered that the use of a refined soil texture not only affected the soil moisture and soil temperature, but also other prediction variables, such as the latent heat, sensible heat, and ground heat fluxes in the NOAH-MP output. The new soil texture input consistently improved the temporal simulation of these critical model variables in the NOAH-MP simulation.

In a future validation, this study would aim to use *in situ* measurements in the proposed approach to improve the soil temperature and soil moisture simulation of the NOHA-MP. Ultimately, the highly resolved soil texture information from microwave remote sensing is expected to resolve NOAH-MP land surface parameters, including soil moisture prediction, for which spatial resolution plays a crucial role in the initiation process of convective precipitation coupled with an atmospheric model system such as WRF (Weather Research and Forecasting Model)[12]–[16]. Furthermore, the proposed forward model may prove to be a useful tool in flux partitioning by means of microwave remote sensing and land surface models. Ultimately, this study will allow us to investigate the energy balance closure problem with unprecedented resolution and scale, which is one of the critical issues in micrometeorology and climate study.

References

- [1] H. Vereecken, J. Huisman, H. Bogaen, J. Vanderborcht, J. Vrugt, and J. Hopmans, "On the value of soil moisture measurements in vadose zone hydrology: A review," *Water resources research*, vol. 44, 2008.
- [2] R. D. Koster, P. A. Dirmeyer, Z. Guo, G. Bonan, E. Chan, P. Cox, *et al.*, "Regions of strong coupling between soil moisture and precipitation," *Science*, vol. 305, pp. 1138-1140, 2004.
- [3] V. Wulfmeyer, C. Flamant, A. Behrendt, A. Blyth, A. Brown, M. Dorninger, *et al.*, "Advances in the understanding of convective processes and precipitation over low-mountain regions through the Convective and Orographically-induced Precipitation Study (COPS)," *Quarterly Journal of the Royal Meteorological Society*, vol. 137, pp. 1-2, 2011.
- [4] V. Wulfmeyer, A. Behrendt, C. Kottmeier, U. Corsmeier, C. Barthlott, G. C. Craig, *et al.*, "The Convective and Orographically-induced Precipitation Study (COPS): the scientific strategy, the field phase, and research highlights," *Quarterly Journal of the Royal Meteorological Society*, vol. 137, pp. 3-30, 2011.
- [5] A. Behrendt, A. Blyth, M. Dorninger, N. Kalthoff, C. Flamant, P. Di Girolamo, *et al.*, "Convective Precipitation in complex terrain: Results of the COPS campaign," *Meteorologische Zeitschrift*, vol. 22, pp. 367-372, 2013.
- [6] S. Khodayar, N. Kalthoff, and G. Schädler, "The impact of soil moisture variability on seasonal convective precipitation simulations. Part I: validation, feedbacks, and realistic initialisation," *Meteorologische Zeitschrift*, vol. 22, pp. 489-505, 2013.
- [7] S. Khodayar and G. Schädler, "The impact of soil moisture variability on seasonal convective precipitation simulations. Part II: sensitivity to land-surface models and prescribed soil type distributions," *Meteorologische Zeitschrift*, vol. 22, pp. 507-526, 2013.
- [8] I. Schröter, H. Paasche, P. Dietrich, and U. Wollschläger, "Estimation of catchment-scale soil moisture patterns based on terrain data and sparse TDR measurements," *Vadose Zone Journal*, 2015.
- [9] P. Grathwohl, H. Rügner, T. Wöhling, K. Osenbrück, M. Schwientek, S. Gayler, *et al.*, "Catchments as reactors: a comprehensive approach for water fluxes and solute turnover," *Environmental earth sciences*, vol. 69, pp. 317-333, 2013.
- [10] G. Y. Niu, Z. L. Yang, K. E. Mitchell, F. Chen, M. B. Ek, M. Barlage, *et al.*, "The community Noah land surface model with multiparameterization options (Noah-MP): 1. Model description and evaluation with local-scale measurements," *Journal of Geophysical Research: Atmospheres (1984–2012)*, vol. 116, 2011.
- [11] H. Bogaen, K. Schulz, and H. Vereecken, "Towards a network of observatories in terrestrial environmental research," *Advances in Geosciences*, vol. 9, pp. 109-114, 2006.
- [12] M. Pause, "Soil moisture retrieval using high spatial resolution Polarimetric L-Band Multi-beam Radiometer (PLMR) data at the field scale," *Imu*, 2011.
- [13] T. Jackson and T. Schmugge, "Vegetation effects on the microwave emission of soils," *Remote Sensing of Environment*, vol. 36, pp. 203-212, 1991.
- [14] T. Schmugge, P. Gloersen, T. Wilheit, and F. Geiger, "Remote sensing of soil moisture with microwave radiometers," *Journal of Geophysical Research*, vol. 79, pp. 317-323, 1974.
- [15] E. G. Njoku and L. Li, "Retrieval of land surface parameters using passive microwave measurements at 6-18 GHz," *Geoscience and Remote Sensing, IEEE Transactions on*, vol. 37, pp. 79-93, 1999.
- [16] M. Owe, R. de Jeu, and T. Holmes, "Multisensor historical climatology of satellite-derived global land surface moisture," *Journal of Geophysical Research: Earth Surface (2003–2012)*, vol. 113, 2008.
- [17] M. Pause, A. Lausch, M. Bernhardt, J. Hacker, and K. Schulz, "Improving Soil Moisture Retrieval from Airborne L-band Radiometer Data by Considering Spatially Varying Roughness," *Canadian Journal of Remote Sensing*, pp. 00-00, 2014.
- [18] R. A. de Jeu, T. R. Holmes, R. Panciera, and J. P. Walker, "Parameterization of the Land Parameter Retrieval Model for L-Band Observations Using the NAFE'05 Data Set," *Geoscience and Remote Sensing Letters, IEEE*, vol. 6, pp. 630-634, 2009.
- [19] M. Owe, R. de Jeu, and J. Walker, "A methodology for surface soil moisture and vegetation optical depth retrieval using the microwave polarization difference index," *Geoscience and Remote Sensing, IEEE Transactions on*, vol. 39, pp. 1643-1654, 2001.

- [20] A. G. Meesters, R. A. De Jeu, and M. Owe, "Analytical derivation of the vegetation optical depth from the microwave polarization difference index," *Geoscience and Remote Sensing Letters, IEEE*, vol. 2, pp. 121-123, 2005.
- [21] H. Vereecken, L. Weihermüller, F. Jonard, and C. Montzka, "Characterization of crop canopies and water stress related phenomena using microwave remote sensing methods: A review," *Vadose Zone Journal*, vol. 11, 2012.
- [22] O. F. Mossotti, "Mem. di mathem. e fisica," in *Modena*, vol. 24, p. 49, 1850.
- [23] L. Rayleigh, "LVI. On the influence of obstacles arranged in rectangular order upon the properties of a medium," *The London, Edinburgh, and Dublin Philosophical Magazine and Journal of Science*, vol. 34, pp. 481-502, 1892.
- [24] J. C. M. Garnett, *Philos. Trans. R. Soc. London*, vol. Ser. A 203, 1904.
- [25] H. Fricke, "Mathematical treatment of the electrical conductivity and capacity of diverse system," *Phys.Rev.*, vol. 24, pp. 575-587, 1924.
- [26] D. A. G. Bruggeman, *Ann. Phys. (Leipz.)*, vol. 24, 1935.
- [27] R. Sillars, "The properties of a dielectric containing semiconducting particles of various shapes," *Institution of Electrical Engineers-Proceedings of the Wireless Section of the Institution*, vol. 12, pp. 139-155, 1937.
- [28] R. Hamilton and O. Crosser, "Thermal conductivity of heterogeneous two-component systems," *Industrial & Engineering chemistry fundamentals*, vol. 1, pp. 187-191, 1962.
- [29] L. Tsang, J. A. Kong, and R. T. Shin, "Theory of microwave remote sensing," 1985.
- [30] D.-H. Yoon, J. Zhang, and B. I. Lee, "Dielectric constant and mixing model of BaTiO₃ composite thick films," *Materials Research Bulletin*, vol. 38, pp. 765-772, 2003.
- [31] M. F. Brown, "Dielectrics," in *Encyclopedia of Physics*, vol. 17, 1956.
- [32] J. R. Wang and T. J. Schumge, "An empirical model for the complex dielectric permittivity of soils as a function of water content," *IEEE Transactions on Geoscience and Remote Sensing*, pp. 288-295, 1980.
- [33] J. R. Birchak, C. Gardner, J. Hipp, and J. Victor, "High dielectric constant microwave probes for sensing soil moisture," *Proceedings of the IEEE*, vol. 62, pp. 93-98, 1974.
- [34] J. Ledieu, P. De Ridder, P. De Clerck, and S. Dautrebande, "A method of measuring soil moisture by time-domain reflectometry," *Journal of Hydrology*, vol. 88, pp. 319-328, 1986.
- [35] M. Ansoult, L. De Backer, and M. Declercq, "Statistical relationship between apparent dielectric constant and water content in porous media," *Soil Science Society of America Journal*, vol. 49, pp. 47-50, 1984.
- [36] M. C. Dobson, F. T. Ulaby, M. T. Hallikainen, and M. A. Elrayes, "Microwave Dielectric Behavior of Wet Soil .2. Dielectric Mixing Models," *Ieee Transactions on Geoscience and Remote Sensing*, vol. 23, pp. 35-46, 1985.
- [37] W. Herkelrath, S. Hamburg, and F. Murphy, "Automatic, real-time monitoring of soil moisture in a remote field area with time domain reflectometry," *Water Resources Research*, vol. 27, pp. 857-864, 1991.
- [38] K. Roth, R. Schulin, H. Flühler, and W. Attinger, "Calibration of time domain reflectometry for water content measurement using a composite dielectric approach," *Water Resources Research*, vol. 26, pp. 2267-2273, 1990.
- [39] P. Ferré, D. Rudolph, and R. Kachanoski, "Spatial averaging of water content by time domain reflectometry: Implications for twin rod probes with and without dielectric coatings," *Water Resources Research*, vol. 32, pp. 271-279, 1996.
- [40] O. H. Jacobsen and P. Schjonning, "Comparison of TDR calibration functions for soil water determination. TDR, Applications in soil science," *Proc. TDR Symp. Rep.*, vol. 11, 1995.
- [41] M. Malicki, R. Plagge, and C. Roth, "Improving the calibration of dielectric TDR soil moisture determination taking into account the solid soil," *European Journal of Soil Science*, vol. 47, pp. 357-366, 1996.
- [42] M. D. Knoll, "A petrophysical basis for ground penetrating radar and very early time electromagnetics: Electrical properties of sand-clay mixtures," University of British Columbia, 1996.
- [43] C. Yu, A. Warrick, M. Conklin, M. Young, and M. Zreda, "Two-and three-parameter calibrations of time domain reflectometry for soil moisture measurement," *Water Resources Research*, vol. 33, pp. 2417-2421, 1997.
- [44] E. Kellner and L.-C. Lundin, "Calibration of time domain reflectometry for water content in peat soil," *Nordic Hydrology*, vol. 32, pp. 315-332, 2001.
- [45] M. Schaap, D. Robinson, S. P. Friedman, and L. A., "Measurement and modeling of the dielectric permittivity of layered granular media using time domain reflectometry," *Soil Sci. Soc. Am. J.*, vol. 67, pp. 1113-1121, 2003.

- [46] M. B. Kowalsky, S. Finsterle, and Y. Rubin, "Estimating flow parameter distributions using ground-penetrating radar and hydrological measurements during transient flow in the vadose zone," *Advances in Water Resources*, vol. 27, pp. 583-599, 2004.
- [47] D. Robinson, S. B. Jones, J. Blonquist, and S. Friedman, "A physically derived water content/permittivity calibration model for coarse-textured, layered soils," *Soil Science Society of America Journal*, vol. 69, pp. 1372-1378, 2005.
- [48] M. G. Todd and F. G. Shi, "Complex permittivity of composite systems: A comprehensive interphase approach," *Dielectrics and Electrical Insulation, IEEE Transactions on*, vol. 12, pp. 601-611, 2005.
- [49] V. L. Mironov, L. G. Kosolapova, and S. V. Fomin, "Physically and mineralogically based spectroscopic dielectric model for moist soils," *IEEE Transactions on Geoscience and Remote Sensing*, vol. 47, pp. 2059-2070, 2009.
- [50] G. Topp, J. Davis, and A. P. Annan, "Electromagnetic determination of soil water content: Measurements in coaxial transmission lines," *Water resources research*, vol. 16, pp. 574-582, 1980.
- [51] C. Roth, M. Malicki, and R. Plagge, "Empirical evaluation of the relationship between soil dielectric constant and volumetric water content as the basis for calibrating soil moisture measurements by TDR," *Journal of Soil Science*, vol. 43, pp. 1-13, 1992.
- [52] M. T. Hallikainen, F. T. Ulaby, M. C. Dobson, M. A. Elrayes, and L. K. Wu, "Microwave Dielectric Behavior of Wet Soil .1. Empirical-Models and Experimental-Observations," *Ieee Transactions on Geoscience and Remote Sensing*, vol. 23, pp. 25-34, 1985.
- [53] M. Wang and N. Pan, "Predictions of effective physical properties of complex multiphase materials," *Materials Science and Engineering: R: Reports*, vol. 63, pp. 1-30, 2008.
- [54] H. Fellner-Feldegg, "Measurement of dielectrics in the time domain," *The Journal of Physical Chemistry*, vol. 73, pp. 616-623, 1969.
- [55] D. B. Sirdeshmukh, L. Sirdeshmukh, and K. Subhadra, *Atomistic Properties of Solids* vol. 147: Springer, 2011.
- [56] L. Palmer, A. Cunliffe, and J. Hough, "Dielectric constant of water films," 1952.
- [57] D. J. Mulla, J. H. Cushman, and P. F. Low, "Molecular dynamics and statistical mechanics of water near an uncharged silicate surface," *Water Resources Research*, vol. 20, pp. 619-628, 1984.
- [58] J. M. Wraith and D. Or, "Temperature effects on soil bulk dielectric permittivity measured by time domain reflectometry: Experimental evidence and hypothesis development," *Water Resources Research*, vol. 35, pp. 361-369, 1999.
- [59] Y. Maréchal, *The hydrogen bond and the water molecule: The physics and chemistry of water, aqueous and bio-media*: Elsevier, 2006.
- [60] K. Knödel, G. Lange, and H.-J. Voigt, "Environmental geology: Handbook of field methods and case studies," *Environmental Geology: Handbook of Field Methods and Case Studies*, by K. Knödel, G. Lange, and H.-J. Gerhard. Editor/s: Bundesanstalt für Geowissenschaften und, Berlin: Springer, 2008. ISBN 978-3-540-74669-0, vol. 1, 2008.
- [61] D. V. Ellis and J. M. Singer, *Well logging for earth scientists* vol. 692: Springer, 2007.
- [62] S. Pawar, P. Murugavel, and D. Lal, "Effect of relative humidity and sea level pressure on electrical conductivity of air over Indian Ocean," *Journal of Geophysical Research: Atmospheres (1984–2012)*, vol. 114, 2009.
- [63] R. N. Barbosa and C. Overstreet, "What Is Soil Electrical Conductivity," *LSU AgCenter* vol. Pub. 3185 2011.
- [64] Y. Kerr, P. Waldteufel, P. Richaume, I. Davenport, P. Ferrazzoli, and J. Wigneron, "SMOS level 2 processor soil moisture algorithm theoretical basis document (ATBD)," *SM-ESL (CBSA), CESBIO, Toulouse, SO-TN-ESL-SM-GS-0001, V5. a, 15/03, 2012.*
- [65] C. Clavier and G. Coates, "Theoretical and experimental basis for the dual-water model for the interpretation of shaly sands," *Dumanoir, Soc. Pet. Eng. J.*, vol. 9, pp. 341-351, 1984.
- [66] C. Böttcher, "Theory of Electric Polarisation," ed: Elsevier, Amsterdam, 1952.
- [67] R. W. Zimmerman, "Thermal conductivity of fluid-saturated rocks," *Journal of Petroleum Science and Engineering*, vol. 3, pp. 219-227, 1989.
- [68] S. H. Ward and G. W. Hohmann, "Electromagnetic theory for geophysical applications," *Electromagnetic methods in applied geophysics*, vol. 1, pp. 131-311, 1988.
- [69] L. Klein and C. T. Swift, "An improved model for the dielectric constant of sea water at microwave frequencies," *IEEE Transactions on Antennas and Propagation*, vol. 25, pp. 104-111, 1977.
- [70] A. Stogryn, "Equations for calculating the dielectric constant of saline water (Correspondence)," *IEEE Transactions on Microwave Theory and Techniques*, vol. 19, pp. 733-736, 1971.

- [71] J. Lane and J. Saxton, "Dielectric dispersion in pure polar liquids at very high radio-frequencies. I. Measurements on water, methyl and ethyl alcohols," *Proceedings of the Royal Society of London. Series A. Mathematical and Physical Sciences*, vol. 213, pp. 400-408, 1952.
- [72] V. Mironov, Y. Kerr, J.-P. Wigneron, L. Kosolapova, and F. Demontoux, "Temperature-and texture-dependent dielectric model for moist soils at 1.4 GHz," *Geoscience and Remote Sensing Letters, IEEE*, vol. 10, pp. 419-423, 2013.
- [73] M. M. Braun and L. Pilon, "Effective optical properties of non-absorbing nanoporous thin films," *Thin Solid Films*, vol. 496, pp. 505-514, 2006.
- [74] C.-H. Park, A. Behrendt, E. LeDrew, and V. Wulfmeyer, "Effective Dielectric Constant for Microwave Land-Surface Remote-Sensing," *IEEE Transactions on Geoscience and Remote Sensing*, 2015.
- [75] S. B. Jones and S. P. Friedman, "Particle shape effects on the effective permittivity of anisotropic or isotropic media consisting of aligned or randomly oriented ellipsoidal particles," *Water Resources Research*, vol. 36, pp. 2821-2833, 2000.
- [76] C. Y. Chan and R. J. Knight, "Determining water content and saturation from dielectric measurements in layered materials," *Water Resources Research*, vol. 35, pp. 85-93, 1999.
- [77] C. Y. Chan and R. J. Knight, "Laboratory measurements of electromagnetic wave velocity in layered sands," *Water Resources Research*, vol. 37, pp. 1099-1105, 2001.
- [78] D. Robinson, S. B. Jones, J. Wraith, D. Or, and S. Friedman, "A review of advances in dielectric and electrical conductivity measurement in soils using time domain reflectometry," *Vadose Zone Journal*, vol. 2, pp. 444-475, 2003.
- [79] T. J. Schmugge, "Remote sensing of soil moisture: Recent advances," *Geoscience and Remote Sensing, IEEE Transactions on*, pp. 336-344, 1983.
- [80] T. J. Jackson, P. E. O'Neill, and C. T. Swift, "Passive microwave observation of diurnal surface soil moisture," *Geoscience and Remote Sensing, IEEE Transactions on*, vol. 35, pp. 1210-1222, 1997.
- [81] T. J. Schmugge, W. P. Kustas, J. C. Ritchie, T. J. Jackson, and A. Rango, "Remote sensing in hydrology," *Advances in water resources*, vol. 25, pp. 1367-1385, 2002.
- [82] T. T. Wilheit, "Radiative transfer in a plane stratified dielectric," *IEEE Transactions on Geoscience Electronics*, vol. 16, pp. 138-143, 1978.
- [83] T. Schmugge, T. Wilheit, W. Webster, and P. Gloersen, "Remote sensing of soil moisture with microwave radiometer-II," *NASA, Tech. Note IN-D-8321, GSFC, Green belt, MD*, 1976.
- [84] T. Schmugge, *Remote sensing of soil moisture: Goddard Space Flight Center USA*, 1976.
- [85] N. R. C. S. Soil Survey Staff, United States Department of Agriculture. U.S. General Soil Map (STATSGO2). Available online at <http://sdmdataaccess.nrcs.usda.gov/>.
- [86] M. Uematsu and E. Frank, "Static dielectric constant of water and steam," *Journal of Physical and Chemical Reference Data*, vol. 9, pp. 1291-1306, 1980.
- [87] J. Davis and A. Annan, "GROUND-PENETRATING RADAR FOR HIGH-RESOLUTION MAPPING OF SOIL AND ROCK STRATIGRAPHY1," *Geophysical prospecting*, vol. 37, pp. 531-551, 1989.
- [88] F. Ulaby, R. Moore, and A. Fung, "Microwave Remote Sensing: Active and Passive, vol. III, Volume Scattering and Emission Theory, Advanced Systems and Applications," *Inc., Dedham, Massachusetts*, pp. 1797-1848, 1986.
- [89] V. L. Mironov, L. G. Kosolapova, and S. V. Fomin, "Physically and mineralogically based spectroscopic dielectric model for moist soils," *Geoscience and Remote Sensing, IEEE Transactions on*, vol. 47, pp. 2059-2070, 2009.
- [90] J. O. Curtis, C. A. Weiss Jr, and J. B. Everett, "Effect of Soil Composition on Complex Dielectric Properties," DTIC Document 1995.
- [91] D. Boyarskii, V. Tikhonov, and N. Y. Komarova, "Model of dielectric constant of bound water in soil for applications of microwave remote sensing," *Progress In Electromagnetics Research*, vol. 35, pp. 251-269, 2002.
- [92] J.-P. Wigneron, Y. Kerr, P. Waldteufel, K. Saleh, M.-J. Escorihuela, P. Richaume, *et al.*, "L-band Microwave Emission of the Biosphere (L-MEB) Model: Description and calibration against experimental data sets over crop fields," *Remote Sensing of Environment*, vol. 107, pp. 639-655, 2007.
- [93] P. O'Neill, S. Chan, E. Njoku, T. Jackson, and R. Bindlish, "SMAP Level 2 & 3 Soil Moisture (Passive) Algorithm Theoretical Basis Document (ATBD)," *Initial Release, version*, vol. 1, 2012.
- [94] J. C. Patton, "Comparison of SMOS vegetation optical thickness data with the proposed SMAP algorithm," Iowa State University, 2014.
- [95] J. Wang and B. Choudhury, "Remote sensing of soil moisture content, over bare field at 1.4 GHz frequency," *Journal of Geophysical Research: Oceans (1978-2012)*, vol. 86, pp. 5277-5282, 1981.

- [96] T. J. Jackson and P. E. O'Neill. "Salinity effects on the microwave emission of soils." *Geoscience and Remote Sensing, IEEE Transactions on*, pp. 214-220, 1987.
- [97] E. G. Njoku and D. Entekhabi, "Passive microwave remote sensing of soil moisture," *Journal of hydrology*, vol. 184, pp. 101-129, 1996.
- [98] K.-E. Lindenschmidt, G. Ollesch, and M. Rode, "Physically-based hydrological modelling for non-point dissolved phosphorus transport in small and medium-sized river basins/Modélisation hydrologique à bases physiques et du transport de phosphore dissous en bassins versants de petite et moyenne tailles," *Hydrological sciences journal*, vol. 49, 2004.
- [99] I. Kistner, G. Ollesch, R. Meissner, and M. Rode, "Spatial-temporal dynamics of water soluble phosphorus in the topsoil of a low mountain range catchment," *Agriculture, Ecosystems & Environment*, vol. 176, pp. 24-38, 2013.
- [100] E. Martini, U. Wollschläger, S. Kögler, T. Behrens, P. Dietrich, F. Reinstorf, *et al.*, "Spatial and Temporal Dynamics of Hillslope-Scale Soil Moisture Patterns: Characteristic States and Transition Mechanisms," *Vadose Zone Journal*, vol. 14, 2015.
- [101] M. Rodell, P. Houser, U. e. a. Jambor, J. Gottschalck, K. Mitchell, C. Meng, *et al.*, "The global land data assimilation system," *Bulletin of the American Meteorological Society*, vol. 85, pp. 381-394, 2004.
- [102] J.-P. Wigneron, J.-C. Calvet, T. Pellarin, A. Van de Griend, M. Berger, and P. Ferrazzoli, "Retrieving near-surface soil moisture from microwave radiometric observations: current status and future plans," *Remote Sensing of Environment*, vol. 85, pp. 489-506, 2003.
- [103] C. Montzka, J. P. Grant, H. Moradkhani, H.-J. H. Franssen, L. 4rvrihermüller, M. Drusch, *et al.*, "Estimation of radiative transfer parameters from l-band passive microwave brightness temperatures using advanced data assimilation," *Vadose Zone Journal*, vol. 12, 2013.

Curriculum Vitae

Chang-Hwan Park

email: ecomm77@gmail.com

Profile	My research interest is to maximize the benefits of remote sensing for the better monitoring and prediction in agriculture and water resource management.
Experience	<p style="text-align: center;">Research Visiting</p> <p>JPL (Jet Propulsion Laboratory – NASA, LA, US) 7/2014 – 9/2014</p> <ul style="list-style-type: none">• Research collaboration with Dr. Tom Jackson and SMAP soil moisture algorithm team <p style="text-align: center;">Research Assistance</p> <p>IRTG (University of Hohenheim and Tuebingen, Germany) 6/2012 – 5/2015</p> <ul style="list-style-type: none">• Develop universal forward model for land surface remote sensing <p style="text-align: center;">Visiting Scientist Associate</p> <p>SMHI (Swedish Meteorological and Hydrological Institute, Sweden) 10/2011 – 3/2012</p> <ul style="list-style-type: none">• Investigation of the global cloud top height algorithm and A-train measurements <p style="text-align: center;">Research Assistance</p> <p>SSEC (Space Science Engineering Center, Madison, Wisconsin, US) 10/2009 – 9/2011</p> <ul style="list-style-type: none">• Integration of fine scale remote-sensing measurement and coarse scale forecast model• Radar data assimilation on WRF (Weather Research and Forecast model) based on EnKF(Ensemble Kalman Filter) mode <p style="text-align: center;">Research Intern 10/2005 – 8/2006</p> <p>KORDI (Korea Ocean Research and Development Institute, Seoul, Korea)</p> <ul style="list-style-type: none">• Numerical modeling of Tsushima Warm Current effect on the East Korea Sea <p style="text-align: center;">Research Assistance 5/2003 – 6/2005</p> <p>Saint-Petersburg State University (Russia)</p> <ul style="list-style-type: none">• Numerical Modeling of Sea water density profile in the Wind driven zonal flow <p>PhD Student (Geoscience) 6/2012 – 6/2015</p>
Education	<p>University of Hohenheim, Stuttgart, Germany</p> <p>M.S. (Meteorology) 8/2006 - 10/2009</p> <p>University of Wisconsin - Madison, US</p> <p>M.S. (Oceanography) 3/2003 – 6/2005</p> <p>Saint-Petersburg State University, Russia</p> <p>Scholarship of National Institute for International Education Development</p> <p>B.S. (Civil and Environmental Engineering) 3/1996 – 3/2002</p>
Other experience	<p>Kookmin University, Seoul, Korea</p> <p>Military service 1/1998 – 3/2000</p>